UNIVERSITY OF KENT

DOCTORAL THESIS

Optical Signal Processing For Data Compression In Ultrafast Measurement

Author:

Chaitanya K. Mididoddi

Supervisor:

Dr. Chao Wang

A thesis submitted in fulfilment of the requirements

for the degree of Doctorate of Philosophy

in

Electronic Engineering

School of Engineering and Digital Arts

Internal Examiner:

Dr. Michael R. Hughes

External Examiner:

Dr. Xu Wang

Date of Defence : 20/03/2019

Ideas do not always come in a flash but by diligent trial-and-error experiments that take time and thought.

Charles K. Kao

Declaration

I, Chaitanya K. Mididoddi herewith declare that this thesis titled Optical Signal Processing For Data Compression In Ultrafast Measurementand the work presented here are my own and I can confirm that :

- The research work was done while pursuing research degree at this University
- The work has been reported without any prohibited assistance of third parties and without making use of aids other than those specified.
- The notions taken over directly or indirectly from other sources have been identified as such.
- This work has not previously been presented in identical or similar form to any other examination board.

The thesis work was conducted from January 2015 to June 2018 under the supervision of Dr. Chao Wang at School of Engineering and Digital Arts, University of Kent.

Chaitanya K. Mididoddi

August 2019

Acknowledgements

First of all, I would like to show my gratitude to my supervisor Dr.Chao Wang for his esteemed guidance.

I would like to express my gratitude to technical support team(Paul Sinnock, Yan Zhang, Joanna Gentry, Edwin Lui, Antonio Mendoza and the team) of School of Engineering and Digital Arts for their help in computer related technical issues. I would like to thank demonstration management(Mark Esdale and Mike Green and the lecturers at the school) for giving me enough teaching work and Stuart Gibson for accepting me as research assistant for a project work which helped me get some financial assistance.

I cherish the time which I spent with my colleagues and Lab mates Guoqing Wang, Eamonn Ahmed, Usman Habib, Anthony Aighobahi, Shabnam Noor and Phillippos.

I would like to thank photonics team in physics department Prof. Adrian Podoleanu, Prof. David Jackson, George Dogbre, Adrian Bradu, Michael Hughes, Manuael Jorge Marques, Sophie, Magalie, Felix, Ramona, Yong and others. Special thanks to Manuel for letting me adapt his latex template, helping me with info on OCT systems and Megalie for lending me her thesis.

Finally I would like to thank my family for their continuous love and support.

Abstract

Today the world is filled with continuous deluge of digital information which are ever increasing by every fraction of second. Real-time analog information such as images, RF signals needs to be sampled and quantized to represent in digital domain with help of measurement systems for information analysis, further post processing and storage. Photonics offers various advantages in terms of high bandwidth, security, immunity to electromagnetic interference, reduction in frequency dependant loss as compared to conventional electronic measurement systems. However the large bandwidth data needs to be acquired as per Nyquist principle requiring high bandwidth electronic sampler and digitizer. To address this problem, Photonic Time Stretch has been introduced to reduce the need for high speed electronic measurement equipment by significantly slowing down the speed of sampling signal. However, this generates massive data volume. Photonics-assisted methods such as Anamorphic Stretch Transform, Compressed Sensing and Fourier spectrum acquisition sensing have been addressed to achieve data compression while sampling the information. In this thesis, novel photonic implementations of each of these methods have been investigated through numerical and experimental demonstrations.

The main contribution of this thesis include (1) Application of photonic implementation of compressed sensing for Optical Coherence Tomography, Fiber Bragg Grating enabled signal sensing and blind spectrum sensing applications (2) Photonic compressed sensing enabled ultra-fast imaging system (3) Fourier spectrum acquisition for RF spectrum sensing

with all-optical approach (4) Adaptive non-uniform photonic time stretch methods using anamorphic stretch transform to reduce the the number of samples to be measured.

Table of contents

List of figures x

List of tables xxiii

1 Introduction 1

1.1 Overview 1

1.2 Summary of objectives and main contributions of the thesis 8

1.3 Organization of Thesis 9

2 Background Theory 13

2.1 Photonic Time Stretch 13

2.2 Compressed Sensing 22

2.2.1 Theory of Compressed Sensing 23

2.2.2 Photonic Implementation of Compressed Sensing 28

2.2.2.1 Time Domain Photonic Compressed Sensing 28

2.2.2.2 Spatial Domain Photonic Compressed Sensing 30

2.2.2.3 Spectral Domain Photonic Compressed Sensing 33

2.3 Signal Sensing with Fourier Spectrum acquisition 35

3 Photonic Compressed Sensing for Data Compression 39

3.1 Time Domain Photonic Compressed Sensing for Optical Coherence Tomography . . . 39
3.1.1 Background on Optical Coherence Tomography . . . 40
3.1.2 Principles . . . 46
3.1.3 Simulation Results . . . 48
3.1.4 Experiment Results . . . 50
3.1.5 Time Domain Photonic Compressed Sensing for OCT with Improved Resolution . . . 51
3.1.6 RF synchronization . . . 55
3.1.7 Evaluation of Minimization Algorithms in Compressive Sensing PTS-OCT . . . 57
3.1.7.1 Reconstruction accuracy . . . 57
3.1.7.2 Computation cost . . . 59
3.1.8 Discussions . . . 61
3.1.9 Conclusion . . . 63
3.2 Spectral Domain Photonic Compressed Sensing for blind spectrum sensing 64
3.2.1 Principles . . . 66
3.2.1.1 Random pattern generation . . . 66
3.2.1.2 Photonic Compressed Sensing . . . 67
3.2.2 Simulation Results . . . 68
3.2.3 Experimental Results . . . 72
3.2.4 Discussions . . . 74
3.2.5 Conclusions . . . 78
3.3 High throughput compressed FBG sensing . . . 78
3.3.1 Results with Time Domain Photonic Compressed Sensing . . . 80
3.3.1.1 Monotonic profile . . . 80

3.3.1.2 S-shaped profile . . . 83
3.3.2 Results with Spectral Domain Photonic Compressed Sensing . . . 84
3.3.3 Discussion . . . 87
3.3.4 Conclusion . . . 88
3.4 Overall Summary . . . 88

4 Spatial Domain Photonic Compressed Sensing for Ultrafast Single-Pixel Imaging 90
4.1 Introduction . . . 91
4.2 Principles . . . 93
4.3 Results . . . 97
4.3.1 Reconstruction of image and comparison with traditional STEAM imaging . . . 97
4.3.2 Resolution information from the random patterns . . . 97
4.4 Discussions . . . 100
4.5 Conclusion . . . 100

5 All-optical FFT scanning for blind spectrum sensing 102
5.1 Introduction . . . 102
5.2 Principles . . . 103
5.3 Experiment Results . . . 105
5.3.1 System calibration . . . 105
5.3.2 Single tone reconstruction . . . 107
5.3.3 Multi tone reconstruction . . . 109
5.4 Discussions . . . 109
5.4.1 Dual tone reconstruction with non-uniform sampling . . . 109
5.5 Conclusion . . . 112

6 Adaptive non-uniform photonic time stretch for high-speed signal detection for data compression **113**

6.1 Principle . . . 115

6.2 Results . . . 116

6.2.1 AST filter with quadratic time delay . . . 117

6.2.2 AST filter with cubic time delay . . . 123

6.2.3 Discussions . . . 126

6.3 Conclusion . . . 127

7 Summary and Future Work **128**

7.1 Summary . . . 128

7.2 Outlook . . . 131

7.2.1 Future work based on AST system proposed in this thesis: . . . 131

7.2.2 Future work for SD-PCS system based on cascaded MZI proposed in this thesis: . . . 132

7.2.3 Future work for UF-PCS imaging system . . . 132

7.2.4 Potential future work for compressed sensing . . . 133

References **134**

Appendix A Publications produced from work reported in this thesis **148**

Appendix B Equipment used in the experiments **151**

Appendix C Sample MATLAB code used for post-processing **157**

List of figures

1.1 Schematic of generic microwave photonic link 2

1.2 Thesis structure 10

2.1 Photonic time stretch concept with temporal and spectral profiles as function of length of dispersive element. Inset shows the dispersive element denoted in this thesis which is a DCF. 14

2.2 Summary of time stretch theory. When higher order dispersion is negligible, the injective mapping is established resulting in Photonic time stretch . . . 17

2.3 Linear time stretch for TS-ADC 18

2.4 Anamorphic Stretch Transform vs linear time stretch. a)Actual signal. A 10 GHz sinusoidal signal with 1 sec duration should be sampled at 20 GS/s for faithful reconstruction. The overall number of samples to be stored are 20 GSamples followed by quantization. b) Linear Time Stretch method is conventional PTS to reduce the sampling rate to 1 GHz but increases the duration to 10 s making the number of stored samples remains same, 20 GSamples c) Anamorphic Stretch Transform uses selective stretching which reduces the sampling rate over certain temporal duration which reduces the number of samples to be stored and compressed 19

2.5 Anamorphic stretch Transform in imaging 21

2.6 Compressed sensing in a nutshell: Imaging example 22

2.7 Theory of CS in nutshell: Random mixing 23
2.8 Compressed sensing in 1D: Matlab simulation example 25
2.9 Typical example of Time Domain Photonic Compressed sensing based on PTS for imaging application 29
2.10 Typical example of spatial domain Photonic Compressed sensing for imaging application 31
2.11 Typical example of spatial domain Photonic Compressed sensing for imaging application 34
2.12 Signal sensing by Fourier spectrum acquisition : Matlab simulation example 37

3.1 Comparison of different biomedical imaging methods. CM:Confocal Microscopy, OCT: Optical Coherence Tomography US: UltraSound MRI:Magnetic Resonance Imaging 41
3.2 Block diagram of the proposed TD-PCS-OCT experimental setup. 45
3.3 Simulation results for a two-layer PTS-OCT measurement. (a) Temporal interference pattern as a result of path length difference. The time-stretched original pulse is shown in red dotted line. (b) The spectrum profile of the optical interference pattern, clearly showing two carrier frequencies of 3.5 GHz and 4 GHz. (c) The reconstructed signal in time domain using 70 measurements. (d) The reconstructed Fourier spectrum showing two strong tones which match with the original signal. 49

3.4 Experiment results for a single-layer PTS-OCT measurement. (a) The temporal interference pattern for five successive pulses. (b) The first 5 PRBS patterns. (c) The modulated waveforms with red marking showing no pattern for exact amount of duration of a bit 0. (d) The compressed optical pulses using a SMF with opposite dispersion profile. The peak power of compressed pulses produce the measurements. (e) Overlapped temporal waveforms for the reconstructed signal (in solid line) and the original signal (in red dash line). (f) Fourier domain representation of the reconstructed signal (in solid line) and the original signal (in red dash line). 52

3.5 Experimental results for a second single-layer sample with different path length difference. (a) The original interference pattern in time domain. (b) Fourier transform of the original interference pattern showing a single carrier frequency of 800 MHz. (c) The reconstructed time domain waveform with 33 measurements. (d) The reconstructed DFT domain signal clearly identifying the 800 MHz frequency component. 53

3.6 Experimental results showing data compressed PTS-OCT with improved frequency resolution. (a) The original temporal interference waveform with a carrier frequency of 725 MHz. (b) Its Fourier transform shows two closely located frequency peaks at 700 and 750 MHz. (c) The constructed temporal waveform based on normal one pulse integration. (d) Reconstructed DFT signal showing only the 750 MHz signal. This indicates a total failure in frequency identification. (e) and (f) show the reconstruction results based on dual pulse integration. The 725 MHz frequency component is successfully identified. 54

3.7 Conventional procedure for RF synchronization 56

3.8 Procedure followed in this thesis for RF synchronization 56

3.9 The reconstructed frequency domain signals for all five algorithms corresponding to a compression ratio of 40%. Red line is the ground truth signal and blue line represents reconstruction. From left to right, top row: (a) NESTA and (b) l_1 Magic; middle row: (c) ADMM Basis pursuit and (d) lasso; bottom row: (e) Matlab lasso for non-standardised data and (f) standardised data respectively. 58

3.10 Evaluation of reconstruction accuracy. (a) RMSE of reconstructed signal calculated over entire frequency range. All five candidate algorithms show a descending trend. NESTA and l_1 Magic algorithm yield the smallest RMS error. (b) RMSE of reconstructed signal calculated for the frequencies spanned by the 4 dominant peaks only. Error rates similar for all five algorithms for small number of measurements. Relative performance of NESTA and l_1 Magic improves as the number of measurements increases. 60

3.11 The computational time as a function of the number of measurements. ADMM Lasso, Matlab Lasso, Matlab Lasso (standardized) and l_1 Magic show small linear increase with respect to number of measurements. Basis pursuit is unstable for measurements <110 due to slow convergence rate . . 61

3.12 Simulation results of compressive sensing of single tone signal 1GHz with L1 reconstruction algorithm. a) FFT spectrum of the original (red) and the reconstructed (blue) signals; b) Time domain of original(red) and reconstructed(blue) signal 62

3.13 Simulation result showing improvement of compression ratio using a Gaussian-shaped analog random bit sequence. The bandwidth of frequency peaks have been reduced. The inset shows the reconstructed temporal waveform, clearly indicating the removal of Gaussian envelope. 64

3.14 Schematic for SD-PCS experimental setup based on cascaded MZI structure with variable optical delay element 66

3.15 Temporal and spectral domain responses of cascaded dispersion-unbalanced MZIs. (a) Spectral domain output and (b) time domain response of the first MZI with a fixed time delay of 50ps; (c) individual spectral domain and (d) time domain response of the second MZI alone with delay of 50ps 69

3.16 Quasi random patterns from cascading effect. a) Temporal domain representation of Random pattern when variable delay is 17.5ps b) Corresponding FFT spectrum c) Temporal domain representation of Random pattern when variable delay is 21.25ps d) Corresponding FFT spectrum e) Correlation of the random patterns generated by varying the delay in second MZI from 1.25ps to 50ps in steps of 1.25ps 70

3.17 Simulation results for 3 tone signal. a) a 3-tone RF signal input repetitive of 20 ns b) Gaussian random patterns with time delay varying from 1.25ps to 5ps c) Corresponding mixed signals d) Summed measurements of varying amplitude levels representing the dot product of random pattern with RF signal d) Output after electro optical mixing with RF signal e) Reconstructed output in time domain after l_1 reconstruction f) Reconstructed signal in Fourier domain showing successful reconstruction of all 3 tones blue representing reconstructed signal with red color representing original signal's FFT representation. 71

3.18 Experimentally generated optical random patterns. a) Random pattern of MZI-1 b) c) Cascaded MZI response with 230ps as variable optical delay in MZI-2 set to 230ps e) Cascaded MZI response with 330ps as variable optical delay in MZI-2 set to 330ps. 73

3.19 Correlation of the random patterns generated by varying the delay in second MZI from 230ps to 330ps in steps of 2ps. 74

3.20 Experimental results with two-tone RF spectrum a) Input test RF signal time domain b) Corresponding FFT representation c) Reconstructed RF signal in time domain shown in blue color. The smoothed version is shown in red color for comparison with original RF signal d) Corresponding FFT representation showing two strong peaks at 0.4GHz and 1GHz. 75

3.21 Experimental results with single tone RF spectrum a) Reconstructed 1GHz tone in time domain b) Corresponding FFT representation c) Reconstructed 0.5GHz tone in time domain d) Corresponding FFT representation. 75

3.22 FFT representations of the random patterns shown in Fig. 3.18 .a) FFT of the cascaded MZI structure when optical delay in MZI-2 set to 230ps. b) FFT of the cascaded MZI structure when optical delay in MZI-2 set to 330ps. . . . 76

3.23 Simulation results for verifying the bandwidth of the proposed setup using VPI-transmission maker software. a) Cross correlation between the random patterns b) Test RF signal in time domain c) Corresponding frequency domain showing RF frequencies 5GHz, 8GHz and 60GHz. d) Reconstructed RF signal from mixing and integration and l_1 reconstruction e) Reconstructed RF signal in FFT domain showing strong spectral powers at exact locations as input RF signal. 77

3.24 Schematic of proposed and simulated TD-PCS-FBG system with traditional binary PRBS based random mixing. 80

3.25 Simulation results for TD-PCS-FBG system with monotonic strain profile. a. Original time stretched sensing signal in time domain b. FFT respresentation of the time domain signal c. Spectrogram of the sensing signal showing linear frequency chirp d. Two PRBS sequences used for mixing e. Mixed signal with PRBS and sensing signal. f. Time domain reconstruction of sensing signal upon l_1 reconstruction with 62.5% compression ratio g. Corresponding FFT domain representation h. Spectrogram showing clear chirp profile. The l_1 reconstruction results are repeated for 75 % ,87.5% and 100 % compression ratios and the time domain reconstruction is shown in Fig. i. l. and o. , corresponding FFT domain representation in Fig. j. m. and p. , and corresponding chirp profiles are shown in Fig. k. n. and q. 81

3.26 Simulation results for TD-PCS-FBG system with S-shaped strain profile. a. Original time stretched sensing signal in time domain b. FFT respresentation of the time domain signal c. Spectrogram of the sensing signal showing linear frequency chirp d. Two PRBS sequences used for mixing e. Mixed signal with PRBS and sensing signal. f. Time domain reconstruction of sensing signal upon l_1 reconstruction with 50% compression ratio g. Corresponding FFT domain representation h. Spectrogram showing clear chirp profile. The l_1 reconstruciton results are repeated for 62.5%, 75 % ,87.5% and 100 % compression ratios and the time domain reconstruction is shown in Fig. i. l. o. and r. , corresponding FFT domain representation in Fig. j. m. p. and s. , and corresponding chirp profiles are shown in Fig. k. n. q. and t. 82

3.27 Schematic of proposed and simulated SD-PCS-FBG system with all-optical random patterns generated from cascaded MZI setup 84

3.28 Correlation between the patterns generated from cascaded MZI setup for SD-PCS-FBG system 85

3.29 Reconstruction results for downward chirp signal with all-optical random pattern generation and mixing. a. Temporal domain reconstruction with 200 measurements with 50% compression ratio. b. Corresponding FFT domain with 200 measurements with 50% compression ratio. c. Spectrogram of the reconstructed signal. The results with 62.5% and 72.5% compression ratios are shown respectively with time domain reconstruction in Fig. d. and g. , corresponding FFT domain representation in Fig. e. and h., and corresponding chirp profiles are shown in Fig. f. and i. 86

3.30 Reconstruction results for S-bend chirp signal with all-optical random pattern generation and mixing. a. Temporal domain reconstruction with 200 measurements with 50% compression ratio. b. Corresponding FFT domain with 200 measurements with 50% compression ratio. c. Spectrogram of the reconstructed signal. The results with 62.5% and 72.5% compression ratios are shown respectively with time domain reconstruction in Fig. d. and g. , corresponding FFT domain representation in Fig. e. and h., and corresponding chirp profiles are shown in Fig. f. and i. 87

3.31 Root Mean Square Error results for TD-PCS-FBG system and SD-PCS-FBG system. a) RMSE as a function of compression ratio for uniform strain signal b) RMSE as a function of compression ratio for S-shaped strain signal . . . 88

4.1 Schematic of Proposed UF-PCS imaging system. Step-1 is performed with experimental setup with tuneable laser source. Step-2 is verified through simulations in MATLAB. Step 1:Experimental calibration. Step 2: Proposed Compressive Imaging system. MMF:Multimode Fibre, Storage: A computer used used to record and store the patterns, MLL:Mode locked laser with a pulse with of 800fs and repetition rate of 20MHz, DCF: Dispersion Compensating Fibre of 1ns/nm chromatic dispersion, PD:free space Photo Detector, Processor: A computer with signal processing capability to extract the image from measurements acquired from scope and patterns recorded from calibration 93

4.2 Four of the recorded patterns from beam profiler. The wavelength step size considered is 0.1 nm from 1550 nm 94

4.3 Correlation matrix of the patterns recorded from beam profiler. This is a symmetric matrix with diagonal being represented by the auto correlation of the pattern which is close to unity. 95

4.4 Self correlation variation for three wavelengths against time duration. . . . 96

4.5 Comparison of results with compressed imaging and conventional STEAM sensing. a) Original image with pixel size 27X27. b) to f) Reconstructed images with l_1 minimization algorithm from with increased number of measurements. g) to k) The sampled images from traditional STEAM imaging system which are emulated by downsampling the original image. 98

4.6 Comparison of MSE for speckle based compressed imaging vs binary patterns based compressed imaging 98

4.7 Nyquist resolution limit. a)Pattern captured by beam profiler with 540X540 pixel resolution b) 2D spectral domain representation after removing the low frequency components c) Superimposed spectral domain representation of individual rows of the image followed by columns of the image shown in Fig. a. d) The random pattern after removing the high spatial frequency low spectral power components shown in Fig. f. e) Corresponding 2D spectral FFT f) superimposed representations after removal of high frequency components g) The random pattern after removing the high spatial frequency low spectral power components shown in Fig. i. h) Corresponding 2D spectral FFT i) superimposed representations after removal of high frequency components j) The random pattern after removing the high spatial frequency low spectral power components shown in Fig. f. k) Corresponding 2D spectral FFT l) superimposed representations after removal of high frequency components. 99

5.1 Schematic of experimental set-up. OC:Optical Power splitter/Combiner, PC:Polarization Controller, PM:Phase Modulator, DC: DC bias signal, IFFT: Inverse FFT , RF Sync.:RF synchronization, EDFA: Erbium Doped Fibre Amplifier 104

5.2 Time delay - Frequency relation after adjusting the offset. The insets show the time domain and FFT representations at a particular optical delay of 130ps. Blue color shows the experimental result. The results from theoretical calculations is shown in red 106

5.3 Optical pulse comparison for individual DC voltage applied to phase modulator. 106

5.4 Demonstration with single tone RF signal. a) Phase shifted and time stretched gaussian optical pulse carrier signal in time domain with 80ns duration at 4ps optical delay. b)Electro-optically mixed optical signal c)Fourier spectrum acquisition showing strong single tone at 9ps optical delay with calibration curve. Red line is the calculated while Blue line is experimental observation d) Time domain reconstruction of the acquired FFT 108

5.5 Demonstration with multitone RF signal. a) Input RF spectrum. b) Reconstructed FFT spectrum. The experimental calibration line is shown in blue color while theoretical calculated line is shown in red color. 108

5.6 Demonstration of dual tone reconstruction with 0.5ps resolution a) Original signal FFT representation b) reconstructed FFT with experimental calibration 110

5.7 Demonstration of anamorphic sampling of FFT. a) Unsuccessful FFT reconstruction by sparse uniform sampling with 3ps delay resolution with experiment calibration b) FFT reconstruction with anamorphic sampling with experiment calibration 110

5.8 Simulation results. a) Input multitoned RF signal with highest frequency 40.2GHz b) Corresponding FFT spectrum of signal c) Phase-shifted optical carrier. Inset shows RF magnitude spectrum d) Signal encoded phase-shifted optical carrier. Inset shows RF magnitude spectrum e) Reconstructed time domain signal from inverse transformation f) Reconstructed FFT spectrum with frequency shown in green color. Optical time delay is shown in X-axis. 111

6.1 Schematic diagram of the proposed and simulated adaptive non-uniform photonic time stretch system. 114

6.2 Simulation results on the microwave photonic phase filtering. (a) The original input RF signal under test. (b) Stretched RF signal by the microwave photonic phase filter with a linear frequency-dependent time delay response. (c) Spectrogram of the original RF signal. (d) Spectrogram of the RF signal after microwave photonic filtering, showing a frequency chirp rate of 2 GHz/ns. 117

6.3 (a) Time stretched optical pulse by the first dispersive element. (b) Optical pulse modulated with the pre-stretched RF signal. (c) Corresponding optical spectrum verifying that the RF signal is also encoded in to spectral domain. (d) One-to-one mapping between time and frequency according to (b) and (c). 119

6.4 (a) The time delay function of the designed AST filter with quadratic group delay. (b) Non-uniformly stretched optical pulse by the AST filter. (c) The reconstructed RF signal following the signal recovery algorithm implemented in digital domain. (d) Spectrogram of AST stretched optical pulse after photo-detection showing the non-uniform photonic time stretch 121

6.5 (a) A second RF signal under test. (b) Pre-stretched RF signal by the same microwave photonic phase filter with linear frequency-dependent time delay response. (c) Spectrogram of the original RF signal. (d) Spectrogram of the pre-stretched RF signal by the microwave photonic phase filter 122

6.6 (a) Modulated optical pulse carrier after non-uniform stretching at the AST filter. (b) The reconstructed RF signal after digital signal recovery 122

6.7 (a) Time delay as a function of optical frequency in the AST filter with cubic group delay response. (b) Non-uniformly stretched optical pulse carrying RF signal by the AST filter. (c) The reconstructed RF signal following the signal recovery algorithm implemented in digital domain. (d) Spectrogram of non-uniformly stretched optical pulse confirming TBP reduction of the captured RF signal. 124

6.8 (a) Modulated optical pulse after non-uniform stretching with the AST filter with cubic time delay. (b) The recovered RF signal 2 after digital signal processing 125

7.1 Summary of thesis work 130

7.2 AST quad filter using Photonic Crystal Fibre 131

7.3 Proposed spectral domain photonic time stretch compressed sensing based OCT system that can sense the A-scan profile of sample 132

B.1 Mendocino series FPL type C -band Desktop 1550nm femtosecond laser . . 151

B.2 Tektronix Arbitrary Waveform Generator 7122C 152

B.3 Agilent 86100A Wideband sampling scope 152

B.4 Tektronix realtime oscilloscope 153

B.5 E4440A PSA Spectrum Analyzer 154

B.6 Optical Spectrum Analyzer Agilent 86146B 154

B.7 Dispersion Compensating Fibre OFS SMFDK-S-020-03-01 155

B.8 General Photonics Variable Optical Delay Line VDL-001 155

B.9 General Photonics Motorized Optical Delay Line MDL-001 156

B.10 Amonics Optical Fibre Amplifier Pre Amplifier AEDFA-PA-35-B-FA . . . 156

List of tables

1.1 Components of photonic link 3

6.1 TBP Reduction for two different RF signals using AST filter with quadratic time delay 121

6.2 TBP Reduction for the first RF signals using an AST filter with cubic time delay 125

B.1 Specifications of MLL 151

B.2 Specifications of AWG: 152

B.3 Specifications of sampling oscilloscope: 153

B.4 Specifications of realtime oscilloscope: 153

B.5 Specifications of electrical spectrum analyser: 154

B.6 Specifications of optical spectrum analyser: 154

B.7 Specifications of DCF: 155

B.8 Specifications of optical delay line: 155

B.9 Specifications of motorized optical delay line: 156

B.10 Specifications of optical amplifier: 156

Chapter 1

Introduction

1.1 Overview

Microwave photonics [1–4] studies interaction between the fields of microwave technology and light wave technology for the applications ranging from wireless sensors [5], communications [6–8], radar [9–11], instrumentation and biomedical applications [12–15]. In general, this field has been classified as [4, 16] generation [17], processing [18, 19] and measurement [20] of microwave/RF or THz [8] signals. Processing analog information such as microwave/RF signals in optical domain has several advantages compared to its electronic counterpart, such as high bandwidth, low information dependant loss(approx. 0.2 dB/km for standard single mode fibre at 1550 nm wavelength range) and immunity to electromagnetic interference [21]. Real-time measurement of RF signal or characterization of microwave photonics system/devices require ultra-fast optical measurement system. However, the inherent consequence of continuous ultra-fast measurement is the big data produced. This thesis work mainly focusses on ultra-fast photonic measurement systems using optical signal processing methods described below and next few chapters for sensing 2D images, Optical Coherence Tomography, Radio Frequency and distributed Fibre Bragg Grating sensed signals with data compression techniques. Within the scope of this thesis, a generic microwave photonic link

for analog information capturing can be illustrated as shown in Figure 1.1 that can cover 1D signal measurement or 2D image detection [20].

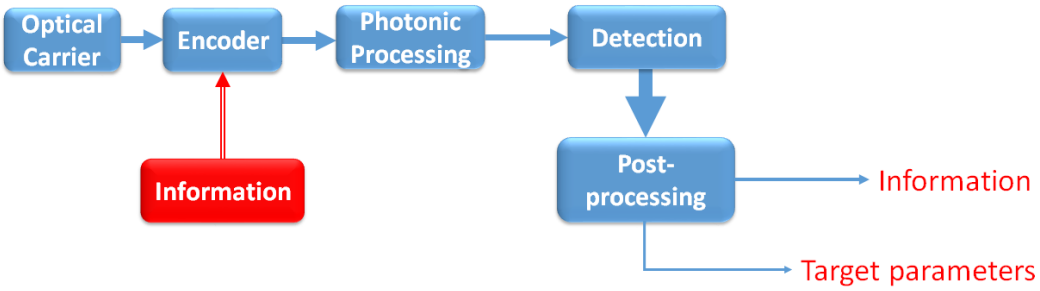

Fig. 1.1 Schematic of generic microwave photonic link

As shown in Fig.1.1, an optical carrier generates light beam and is encoded with information to be captured. Followed by Photonic processing module, detection and post-processing, the information can be reconstructed or certain properties of the information can be extracted using machine learning. Typical components or examples for each of the module are shown in table 1.1.

In general, any measurement system is expected to be (1) High Speed: Data needs to be acquired and processed quickly. In particular, the sampling system should sample high bandwidth signals at twice the maximum frequency as per Nyquist-Shannon principle and this necessitates high speed acquisition. (2) High resolution: Highly accurate with fine resolution (3)High operation stability (4) Economically feasible: Affordable with low energy consumption(i.e., greener solution) (5) Compact footprint: The physical size of unit is expected to be smaller which can be achieved by integrating into Photonic Integrated Circuit. However, not only the physical footprint of the optical system but also the data to be sampled and stored should be compact in size which can be referred to as digital size. In this thesis, reducing digital size of the ultrafast signal measurement system has been mainly discussed. Also, methods have been proposed and demonstrated to make measurement

Table 1.1 Components of photonic link

Component	Several eamples
Optical carrier	1. A narrow-band Continuous Wave laser 2. A broadband ultra-short pulsed laser that can be produced by mode locked lasers [22] 3. A super continuum source [23] 4. A broadband incoherent source [24] 5. A multi-wavelength source [25, 26]
Information	1. 1D microwave/RF signal 2. 2D image
Encoder	1. Mach-Zehnder modulator to sense the RF information 2. Michelson interferometry 3. Spectrum-encoded imaging system involving lenses and diffraction gratings
Processing	1. 1D random pattern for mixing 2. 2D spatial pattern 3. Optical spectral filter
Detection	1. A Photodetector followed by Analog-to-digital converters and data storage units. 2. CCD/CMOS camera in case of direct imaging
Post-processing	1. Information analysis which is processed with Digital signal processing units used for reconstruction of exact information 2. Required target parameters using big data analytics or deep learning algorithms[27]

systems economically feasible by employing low speed photodetectors and digitizers for high-speed signal detection.

Due to recent matured technology in generation of high speed signals and the need for capturing information at high scanning rate, ultrafast measurement systems [20, 28, 29] have gained importance in biomedical[30, 31], security[32] and communications[33] fields. This ultrafast sampling is crucial to convert high speed analog information such as 1D signals and 2D images from analog continuous domain to sampled and quantized digital domain for post-processing computational analysis. In order to sample high speed data, the measurement system encounters these 2 limitations.

Nyquist criterion: High speed sampling electronic equipment is required to sample the information sufficiently as per Nyquist principle which states that the sampling rate should be atleast twice the maximum frequency of analog information for faithful reconstruction or analysis.

To suppress this high speed requirement, the concept of Photonic Time stretch(also known as dispersive fourier transform [16, 34]) method has been introduced and studied. This method has significantly slowed down frequency of the information so that it can be sampled with low speed electronic digitizers. An additional advantage is that the signal can not only be sensed in time domain, but also in optical wavelength domain using a spectral channelization approach [16]. However, this has not addressed the problem of digital size or data compression. As a simplified example, a 10GHz RF signal requires 20GS/s digitizer for sampling. With photonic time stretch, if the RF signal is modulated to optical domain, and stretched by a factor of 10, the effective RF signal frequency is 1GHz. Hence, a 2GS/s photo detector and electronic digitizer is sufficient to capture the signal. However, the effective RF signal is longer in time making overall TBP or the number of samples to be stored in the system after sampling, remains unchanged. Hence, this "Big Data" problem remains.

"Big Data" problem: For example, a 1D multi-toned RF signal of maximum frequency 10GHz would require an analog to digital converter sampling at 20GS/s rate and if sampled for 4 seconds assuming 10bit quantization resolution per sample, total data volume of 93GB can be generated and a modern UHD Blue ray disk would be completely filled. If the signal is stretched using photonic time stretch principle, the number of samples to be stored remains the same as the TBP is unchanged. Exemplifying the scenario with 2D image, a current 4K image with 3840X2160 resolution would require processing of 8 million pixels per image at a certain frame rate. Its unimaginable to process such "Big data" [35] images without compression[36]. To address this, Conventional JPEG2000 has been developed which is extremely successful image compression algorithm to reduce the image size to great extent without loosing much graphical detail to the human perception by zeroing out the low spectral powered wavelet coefficients based on certain threshold. However, an entire image has to be captured before this post processing algorithm takes place [37]. The case is more intense in case of video streaming, capturing a sequence of scans. This continuous torrent of data necessitated the need for data compression methods. There are multiple solutions proposed for this problem which resulted in (A) Achieving data compression while sampling the information (B) Reducing the need for high speed electronic sampling scopes and detectors and effectively reducing the cost of the overall system. A few existing approaches are introduced as solutions. (1) Anamorphic Stretch Transform(AST) (2) Compressed Sensing(CS) (3) Signal Sensing with Basis Acquisition.

*AST:*One solution being, feature selective time stretch where certain segments with rich information of the signal/image is stretched/highly sampled and remaining part is coercively sampled which can be defined as AST [38] or non-linear sampling. Due to the nature of sampling, it is mainly employed in optical domain with Photonic Time Stretch principle which maps broadband spectrum of an ultra-short optical pulse to a time stretched waveform using chromatic dispersion. This enables spectro-temporal information transfer and has become

an emerging and enabling technique for various microwave photonics applications. The background theory will be discussed in Chapter 2 in detail. The AST method is considered to be an enhanced version of Photonic Time Stretch principle. If the region of interest of the signal is known as priory, interested segments of the signal can be stretched further using customized optical group delay filter which can stretch selected range of wavelengths over time. As the time is mapped to optical frequency, time domain of the selective region will be stretched further enabling us to sample the high frequency transients with low speed digitizers. To perform this, a time-bandwidth engineered custom-fibre bragg grating with pre-defined group delay-optical frequency function is placed as aforementioned optical group delay filter [35, 39–42]. The AST method has found applications in flow-cytometry, data compressed time stretch imaging [43]. However, as mentioned, this requires prior knowledge of "Region of Interest" of the information either in time or spatial domain and hence, the system has to reconfigure the time stretch filter for different inputs with different regions of interest. In this thesis, an adaptive non-uniform sampling method has been demonstrated to address this issue by pre-stretching the information before AST.

*CS:*Alternatively, aforementioned big data problem and high speed electronic detection requirement can be addressed with CS which is a signal processing paradigm where sensed information can be reconstructed with far less measurements than the traditional electronic detectors [37, 44–47]. In this method, the sensing information is mixed with a set of random masks and are individually summed and considered as measurements and the original information is reconstructed during post-processing stage using l_1-minimization methods having known the random patterns as priory. This enables data compression and reduces the necessity of using high speed electronic digitizers. However, it is assumed that the information is sparse in some transformation domain such as Fourier, gabor, wavelet or even temporal domain and that the set of random masks are incoherent. The information can be reconstructed during post-processing stage where the obtained measurements and

random masks are given as inputs. Applications for Compressed sensing range from ultra-wideband RF signals in software-defined radio [48], bind RF spectrum sensing, electronic warefare to imaging, trace gas sensing and video compressing, THz imaging [49–51], 3D imaging[52] and Hyperspectral imaging[53]. Of lately, there has been interest in photonic compressed sensing system owing to large bandwidth availability and other advantages with optical domain in contrast to conventional electronics such as GHz information processing capability and already existing imaging technologies. In general, Photonic implementation of Compressed Sensing systems can be categorized into 3 different types based on the domain of random pattern mixing. (1) Time Domain Photonic Compressed Sensing (2) Spectral Domain Photonic Compressed Sensing (3) Spatial Domain Photonic Compressed Sensing. These methods developed within the thesis work will be discussed in detail in subsequent chapters.

*Signal sensing with Fourier Spectrum Acquisition:*Aforementioned CS method requires random patterns to be known as priory for reconstruction, in case of traditional binary patterns generated from SLM or electronic PRBS generators or random patterns generated from all-optical methods. This specific requirement can be eliminated by scanning the entire information in its transformation domain also referred to as "Basis Scan". The basis can be Fourier domain [54–58] or Wavelet domain such as haar basis[59] to name a few. In Fourier spectrum acquisition method, the sensing information is mixed with a set of phase shifted and harmonic signals or patterns and the information is reconstructed by inverse transformation during post-processing[56, 55]. To achieve data compression, frequency based thresholding has been demonstrated [55]. However, the scanning time is longer than traditional CS approach as sensing will be done 4 times higher. This method requires sweeping of phase shifted RF signals to scan the whole frequency band which would require high speed and expensive RF generators or Arbitrary Waveform Generator. In this thesis, a novel photonics-assisted Fourier spectrum acquisition method has been demonstrated, which

scans the spectrum of an unknown signal with single pixel photodetector without high speed RF generator.

1.2 Summary of objectives and main contributions of the thesis

Objectives: In this thesis, the main objectives can be summarized as (1) To reduce massive data volume (digital size) during information sensing by utilizing various compressed sensing methods. (2) To acquire information using low speed electronic sampler and digitizers (3) Reduce physical size of overall measurement system by employing novel all-optical methods (4) To explore compressed sensing enabled ultra-fast imaging system (5) To explore alternative systems to sparsity constrained compressed sensing methods by investigating all-optical methods for basis scan.

Main contributions of the thesis: In this thesis, three different types of photonic implementation of compressed sensing systems for applications such as biomedical OCT scanning (single layer model), distributed FBG sensing have been proposed and experimentally demonstrated. With help of numerical simulations and experimental setup, photonic compressed sensing has been demonstrated for Michelson OCT system and data compression has been achieved [60–62]. The work has been extended for measuring strain sensing with distributed FBG grating [63] . However the used binary random masks require high bandwidth front end electronic equipment which are expensive and induce signal loss. In addition, they have huge physical size making over all system bulky. The overall limitations of this system have been presented in [64]. To overcome these difficulties, analog all-optical random pattern generation by cascaded Mach-Zehnder Interferometric structures have been demonstrated.

This work has been published in [65]. These generated optical random patterns have been applied to blind RF spectrum sensing [66] and distributed FBG sensing.

Realtime ultra-fast imaging has been area of interest to achieve high imaging speeds. Utilizing compressed sensing capability to reconstruct an image with reduced number of measurements, in this thesis, photonic compressed sensing enabled ultra-fast imaging system that can sense the images with 20 Million frames per second[67] has been proposed. This has been achieved by wavelength dependant chaotic nature of multimode fibre.

In addition to compressed sensing systems, a method to generate the phase shifted sinusoidal illumination patterns in optical domain utilizing electro-optic phase modulator and optical delay line elements have been proposed and experimentally demonstrated. The advantage is that it can generate upto 150GHz with a commercially available delay line and low sampling detector that may not be (to the best of our knowledge) determined by current state-of-the-art electronic detectors. With this setup, an unknown radio frequency spectrum has been sensed. This method can have applications in imaging, OCT and ultra-wideband RF signal sensing[54].

With AST approach, an adaptive non-uniform photonic time stretch method has been proposed based on microwave photonics pre-stretching that achieves blind detection of high-speed RF signals with reduced TBP. Non-uniform photonic time stretch using both quadratic and cubic group delay response has been demonstrated with significant TBP compression ratio[68].

1.3 Organization of Thesis

- In **Chapter 1**, a brief introduction on ultra-fast measurement systems have been presented. Major contribution and organization of thesis has been summarized with help of general schematics.

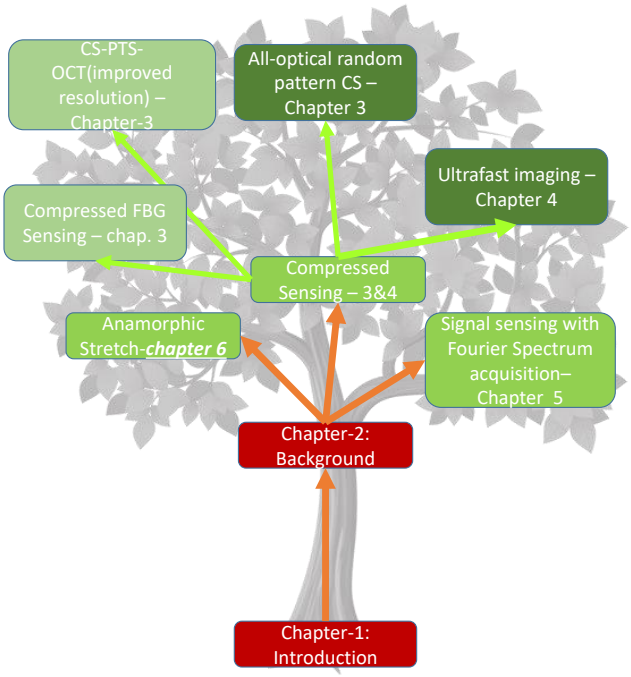

Fig. 1.2 Thesis structure

- In **Chapter 2**, a background review of the methods used in ultra-fast measurement systems been discussed with numerical equations. The general concept of Photonic Time Stretch has been explained for ultra-short pulsed optical source such as Mode locked laser and various alternatives to produce the time stretch method have been referenced. Followed by this, Anamorphic Stretch Transform or non-linear photonic time stretch concept has been discussed with help of figures in detail. An alternative method of compressed sensing has been discussed along with various types of Photonic Compressed Sensing systems with current state of the art techniques. Similarly, background theory for spectrum sensing by Fourier spectrum acquisition is another approach which has been discussed.

- In **Chapter 3**, a brief introduction on Optical Coherence Tomography and specifically, SS-OCT system has been discussed. Followed by this, data compression in high-throughput photonic time-stretch OCT by exploiting the spectral sparsity of the encoded

reflection profile using time domain photonic compressed sensing approach have been presented. By direct optical implementation, the necessity of high speed electronic equipment followed by storage constraints have been heavily relaxed. In addition, a method of improving frequency measurement resolution in the proposed system has been demonstrated. A number of optimization algorithms for the post-processing of the OCT signals have been compared in terms of accuracy and efficiency. Similarly, time domain photonic compressed sensing system for measuring strain and temperature using fully distributed FBG sensors have been demonstrated with a brief introduction on OTS-FDR [28].

Due to the limitations present in time domain photonic compressed system, a novel spectral domain photonic compressed sensing has been proposed and experimentally demonstrated for detection of unknown RF spectrum. The technique is based on photonic time stretch involving cascaded MZIs for spectral domain random mixing explained in great detail in chapter 3. In a proof-of-concept experiment, successful detection of single tone and two-tone RF signals with very low compression ratio using very low detection bandwidth has been demonstrated. The method has been extended to strain sensing using distributed FBG interrogation technique.

- In **Chapter 4**, a brief introduction on single pixel imaging has been presented emphasising the necessity of high speed imaging. Conventional approaches can reach imaging rates of 1000's of frames per second. Utilizing the ability of compressed sensing system to reconstruct a naturally sparse image with few number of samples, an ultra-fast optical imaging method with multimode fibre has been demonstrated. This has been achieved by generating incoherent 2D speckle patterns by varying optical wavelength. A real-time imaging speed of 20 Million frames per second has been proposed in a proof-of-concept demonstration. However, the image size is dependant on field of view of the fibre. The schematic and principle related to this method

has been explained in detail with experimentally generated speckle patterns and with numerical simulations.

- In **Chapter 5**, an all-optical approach for Fourier spectrum scanning of a blind spectrum sensing has been proposed and experimentally demonstrated. Any arbitrary signal in time domain can be sensed indirectly in Fourier domain by measuring the magnitude and phase spectra. This has been implemented by generating phase shifted sinusoidal illumination patterns followed by post-processing techniques. A brief introduction based on previous methods has been presented followed by the approach of generating these phase shifted sinusoidal illumination patterns directly in optical domain based on PTS method. The entire Fourier spectrum can hence, be scanned for non-zero DFT coefficients with a uniform tunable resolution at very low speed. Fourier spectrum scanning of single tone 1GHz and multi tone RF signals with as low as 50MS/s sampling rate has been demonstrated. A method to improve the measurement rate has been proposed. However the scanning rate is dependant on the number of measurements which is typically few Hz or below. This has been explained in great detail in chapter 5.

- In **Chapter 6**, an adaptive non-uniform photonic time stretch method based on microwave photonics pre-stretching that achieves blind detection of high-speed RF signals with reduced TBP has been presented. In general, AST is constrained by "region of interest" of the sensing signal. A method has been proposed to relax this constraint.

- In **Chapter 7**, Overall summary has been provided based on the work presented in this thesis. A final discussion has been drawn along with prospective future work based on the this work.

Chapter 2

Background Theory

In this chapter, a complete literature review of PTS [34, 16], CS, Signal sensing with Fourier spectrum acquisition methods followed by a summery of the work done in this thesis have been discussed along with theoretical explanations, numerical equations supported by referenced work from various research groups.

2.1 Photonic Time Stretch

As explained in [69, 70], there exists a duality between paraxial diffraction in space and dispersion of narrowband pulses. Based on diffraction-dispersion analogy, quadratic time-phase modulation can be acted as a time lens. Under second order dispersion approximation [71, 72], if a transform limited ultrashort optical pulse is propagated through highly dispersive fibre as pictorized in Figure 2.1, the output pulse in time domain is tuned to magnitude spectrum of the input pulse and an injective mapping between time domain and optical frequency/wavelength can be established. This is known as PTS [73], [74], also known as dispersive Fourier transform [75, 71, 16], Real-Time Fourier transform [76], [77], or wavelength-to-time mapping [78–80]. After PTS, the pulse diminishes in peak amplitude as the pulse energy is constant requiring an optical amplifier to improve the pulse power and it

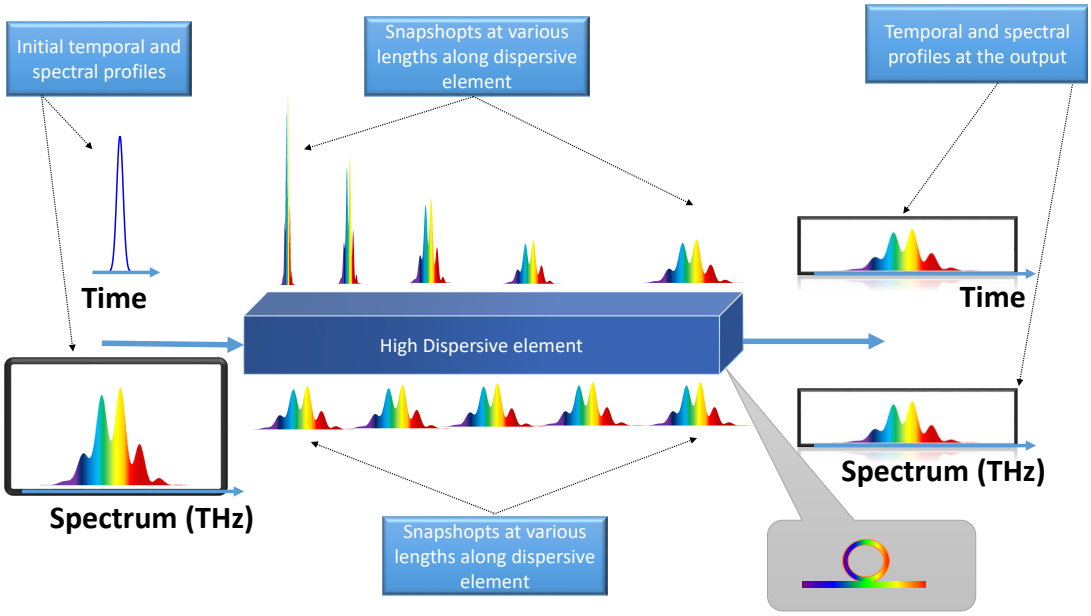

Fig. 2.1 Photonic time stretch concept with temporal and spectral profiles as function of length of dispersive element. Inset shows the dispersive element denoted in this thesis which is a DCF.

is assumed that non-linear effects are neglected in the dispersive device. However, resent research suggests that the amplification can be avoided with dissipative solitons [81].

Considering that the impulse response of the dispersive element as $H(\omega) = |H(\omega)| \times e^{-j\Phi(\omega)}$, where $|H(\omega)|$ is the amplitude spectrum and $\Phi(\omega)$ is the phase spectrum.

As per the Taylor series expansion, the phase spectrum $\Phi(\omega)$ can be expanded around the central optical frequency ω_0 as,

$$\Phi(\omega) = \Phi(\omega_0) + (\omega - \omega_0)\dot{\Phi}(\omega_0) + \frac{1}{2}(\omega - \omega_0)^2\ddot{\Phi}(\omega_0) \tag{2.1}$$

assuming that the higher order derivative terms have negligible values compared to optical phase $\Phi(\omega_0)$ and other product terms.

Hence the impulse response $H(\omega)$ can be re-arranged as,

$$H(\omega) \propto |H(\omega)| \times exp(-j\Phi_0)exp(-j\dot{\Phi}_0\omega))exp(-j\frac{1}{2}\ddot{\Phi}_0\omega^2) \tag{2.2}$$

The system response $h(t)$ can be obtained by inverse FFT of $H(\omega)$ which can be written as,

$$h(t) = IFFT(H(\omega)) \propto \int_{-\infty}^{\infty} |H(\omega)| \times exp(-j\Phi_0) exp(-j\dot{\Phi}_0\omega)) exp(-j\frac{1}{2}\ddot{\Phi}_0\omega^2) \times exp(j\omega t) d\omega \tag{2.3}$$

Ignoring the constant terms and assuming that the dispersion element has no effect on magnitude spectrum,

$$h(t) \propto \int_{-\infty}^{\infty} exp\left[-j\frac{\ddot{\Phi}_0}{2}\left(\omega - \frac{-\dot{\Phi}_0}{\ddot{\Phi}_0}\right)^2\right] \times exp(j\omega t) \times d\omega \tag{2.4}$$

This is a well known integral [82, 83] and $h(t)$ can be derived as,

$$h(t) \propto exp\left(j\frac{-\dot{\Phi}_0}{\ddot{\Phi}_0}t + j\frac{t^2}{2\ddot{\Phi}_0}\right) \tag{2.5}$$

The above expression can be written as,

$$h(t) \propto exp\left(j\frac{(t-\dot{\Phi}_0)^2}{2\ddot{\Phi}_0}\right) \tag{2.6}$$

If the time limited input considered as $x(t)$, the output y(t) can be formulated as,

$$y(t) = x(t) * h(t) \tag{2.7}$$

$$y(t) \propto \int_{t'=-\infty}^{t'=\infty} x(t') exp\left(j\frac{(t-t')^2}{2\ddot{\Phi}_0}\right) dt' \tag{2.8}$$

$$y(t) \propto \int_{t'=-\infty}^{t'=\infty} x(t') exp\left(j\frac{t^2}{2\ddot{\Phi}_0}\right) exp\left(j\frac{t'^2}{2\ddot{\Phi}_0}\right) exp\left(j\frac{-tt'}{\ddot{\Phi}_0}\right) dt' \tag{2.9}$$

If the input pulse is time limited and the pulse width $t'^2 << \ddot{\Phi}_0$ where $\ddot{\Phi}_0 = \frac{d\tau}{d\nu}$ in ps^2 which can be expressed in two different forms given below.

$\ddot{\Phi}_0 = \frac{-\lambda^2}{c}\ddot{\Psi} = 2 * \pi * D_\omega$ where $\ddot{\Psi} = \frac{d\tau}{d\lambda}$ in ps/nm $D_\omega = \frac{d\tau}{d\omega}$ in ps^2/rad

With above approximation, the term $exp\left(j\frac{t'^2}{2\ddot{\Phi}_0}\right)$ can be neglected to be 1 and the overall output temporal response can be approximated as,

$$y(t) \propto exp\left(j\frac{t^2}{2\ddot{\Phi}_0}\right)\int_{t'=-\infty}^{t'=\infty} x(t')exp\left(j\frac{-tt'}{\ddot{\Phi}_0}\right)dt' \tag{2.10}$$

which can be re-written ignoring the phase reference as,

$$y(t) \propto X(\omega)\Big]_{\omega=\frac{t}{\ddot{\Phi}_0}} \tag{2.11}$$

The above equation explains that output time domain is proportional to spectral response with injective mapping between time and optical frequency domains. Because of the inverse relation between the wavelength and optical frequency, there will be inverse one-one mapping between wavelength and time.

However, the explained theory works under two important assumptions. First assumption is that input is transform limited, ultra-short pulse. Also, the square of the pulse width should be negligible compared to dispersion parameter $\ddot{\Phi}_0$. The second assumption is that the higher order dispersion is not present or negligible compared to lower order terms. The presence of higher order dispersion distorts injective mapping between time and optical frequency into many to one [84]. This has been shown graphically in Figure 2.2.

The aforementioned PTS concept is implemented mainly with pulsed source and highly dispersive element followed by optical amplification. The dispersive element can be designed for various optical wavelengths regime. Generally, Single mode Fibre(SMF) and more specifically DCF can be used. However, DCF has better dispersion to loss ratio but its mainly available in 1550nm. Alternatively, a Ch-FBG [34] can be used. The advantage with Ch-FBG is that they are compact, easily customizable and foot print of dispersion can be significantly reduced with monolithic integration. The drawback of using Ch-FBG may be

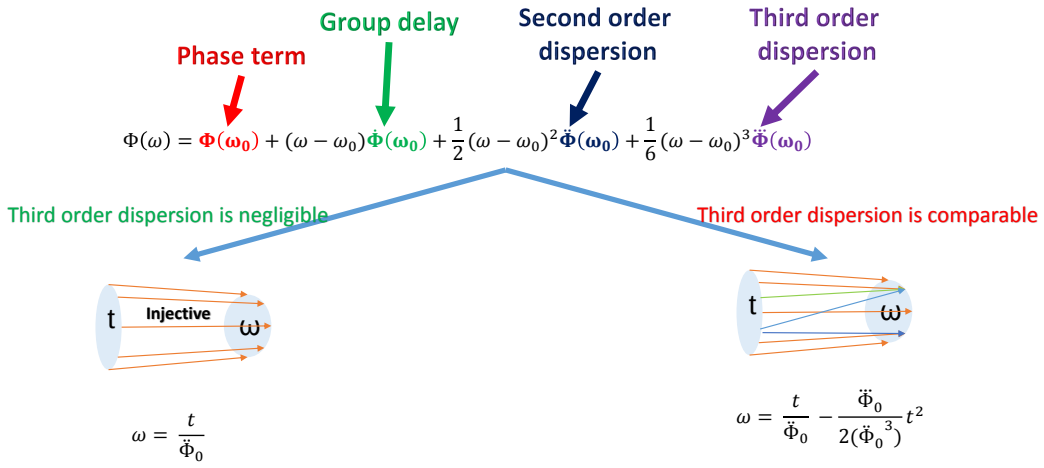

Fig. 2.2 Summary of time stretch theory. When higher order dispersion is negligible, the injective mapping is established resulting in Photonic time stretch

the GVD distortion which can be converted to fast temporal modulation. Another technique is to use the chromo-model dispersion with diffraction grating and Multimode Fibre setup. For biomedical applications in 800nm regime, small core fibres can be used for PTS [34]. Alternatively, a FACED device has been demonstrated for PTS in visible wavelength [85]. For wavelengths at 500nm, 2.0μm, PTS approaches have been demonstrated [86, 87]. While these demonstrates the wavelength to time mapping, the VIPA involves mapping wavelength range to space facilitating 2D spectral shower[31] when combined with above methods.

Recently, PTS method has also been demonstrated without dispersion approximation using an acousto-optical frequency shifting followed by round trip cavity to achieve time-frequency mapping [88].

The optical source can generally be a mode locked laser or a super continuum source. It has also been demonstrated with an incoherent source [89]. Alternative to PTS, there have been demonstrations of using frequency combs [90]. These can be generated from

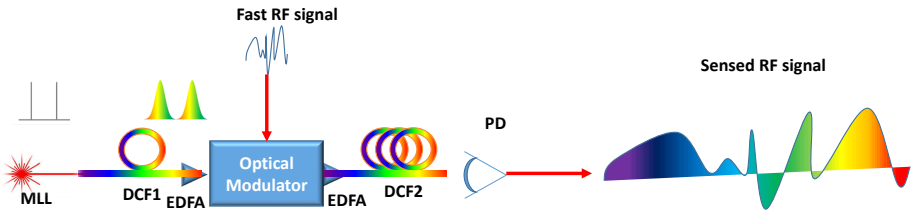

Fig. 2.3 Linear time stretch for TS-ADC

multi-wavelength source followed by cascaded modulation from an RF source [26] or optical frequency combs generated from micro resonator [91] followed by cascaded modulation.

The PTS technology has been used in numerous applications from imaging to biomedical applications such as OCT [92, 93, 12, 14, 94, 15, 95], microscopy [89, 96, 55],high speed imaging [97, 74], photonic analog to digital converter [98–100], optical wireless communications [101] and capturing non-repetitive events [102].

If the PTS achieves time-wavelength mapping, the high RF frequency information may not be captured and it needs to be stretched further. This can be achieved by linear time stretch method where the optical signal subjected to dispersive fourier transform is further stretched with another dispersive element and the stretch factor is the ratio of second element's dispersion to that of the first [99, 16, 103]. The process has been depicted in Figure 2.3. A MLL can generate ultra-short broadband optical pulses which are stretched using dispersion compensating fibre (DCF1) as per PTS principle. The time stretched pulses are amplified with EDFA and electro-optically modulated with fast RF signal. The encoded optical pulses are amplified and stretched further with DCF2 and low speed PD can be able to sense the RF signal. Based on this method, a femtosecond single shot digitizer [104] has been designed with a stretch factor of around 250 to increase the effective bandwidth of low speed photodetector and electronic sampler. TS-ADC has been proposed to linearly stretch the signal and WDM is used to sense the signal using parallel optical filter and during the

post-processing, the signal can be reconstructed.

Photonic Time Stretch with Mode locked Laser is the main foundation for rest of the thesis for works reported in chapters 3,4,5 and 6.

Anamorphic Stretch Transform: Despite that the conventional linear time stretch is useful in boosting the bandwidth of the system, apparently the record time is increased by the stretch factor making the overall TBP constant. Recently, non-uniform photonic time stretch, also known as AST [38, 35, 40], has been proposed to address this issue based on selective stretching: the information rich (high-frequency) region of the input signal is stretched more with nonlinear group delay such that it can be sampled with finer resolution than the slower temporal features [40]. An illustrative example is shown in Fig. 2.4.

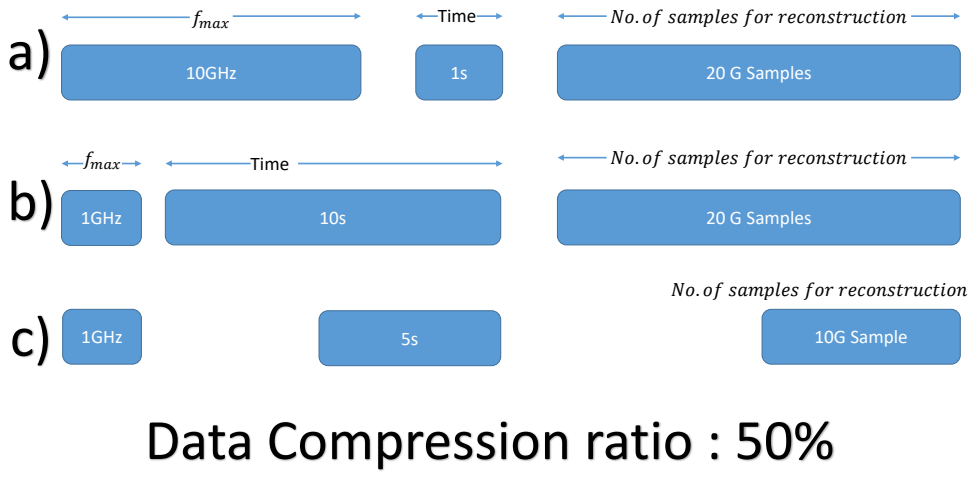

Fig. 2.4 Anamorphic Stretch Transform vs linear time stretch. a)Actual signal. A 10 GHz sinusoidal signal with 1 sec duration should be sampled at 20 GS/s for faithful reconstruction. The overall number of samples to be stored are 20 GSamples followed by quantization. b) Linear Time Stretch method is conventional PTS to reduce the sampling rate to 1 GHz but increases the duration to 10 s making the number of stored samples remains same, 20 GSamples c) Anamorphic Stretch Transform uses selective stretching which reduces the sampling rate over certain temporal duration which reduces the number of samples to be stored and compressed

A multitoned RF signal with maximum frequency of 10 GHz (occupied only for some duration) and record time 1 second requires storage of 20 GSamples for reconstruction. With Linear time stretch of factor 10, the maximum frequency can be reduced to 1GHz. However, the record time is increased by same factor. Hence, the TBP remains constant. With AST, if the 10 GHz frequency location is known, Only that segment can be stretched and the number of samples can be reduced to 10 Gsamples making the compression ratio as 50%. However, prior knowledge of the spectral-temporal profile of the input RF signal is needed in order to design the signal-specific AST filter [42], which is usually not feasible and practical in real-time detection of unknown high-speed RF signals. Moreover, the AST filter needs to be reconfigured for new RF signals with different instantaneous frequency profiles. This makes the implementation of AST filter with engineered nonlinear group delay response more challenging. Therefore a generalized adaptive non-uniform photonic time stretch design for blind detection of arbitrary RF signals with TBP reduction is highly desired. An illustrative application for AST in imaging is shown in Figure 2.5.

A mode locked laser followed by dispersion compensating fibre stretches the ultra-short pulse and maps to optical spectrum. The stretched pulse is amplified and directed to fibre collimator (FC) and magnified using beam expander setup. A diffraction grating is used to spatially disperse the optical wavelength to space thereby, time to wavelength to space mapping can be achieved. If image is spatially encoded to this stretched pulse using lenses, the information can be encoded to spectral and temporal domains. The encoded pulse can be directed to AST filter which stretches the temporal profile based on the group delay of optical wavelengths designed in AST filter. Hence, selective stretching in time domain can be achieved [43]. The reshaped signal can be sampled at relatively low speed photodetector and low speed electronic digitizers. With post-processing, the information can be reconstructed with digital signal processing unit.

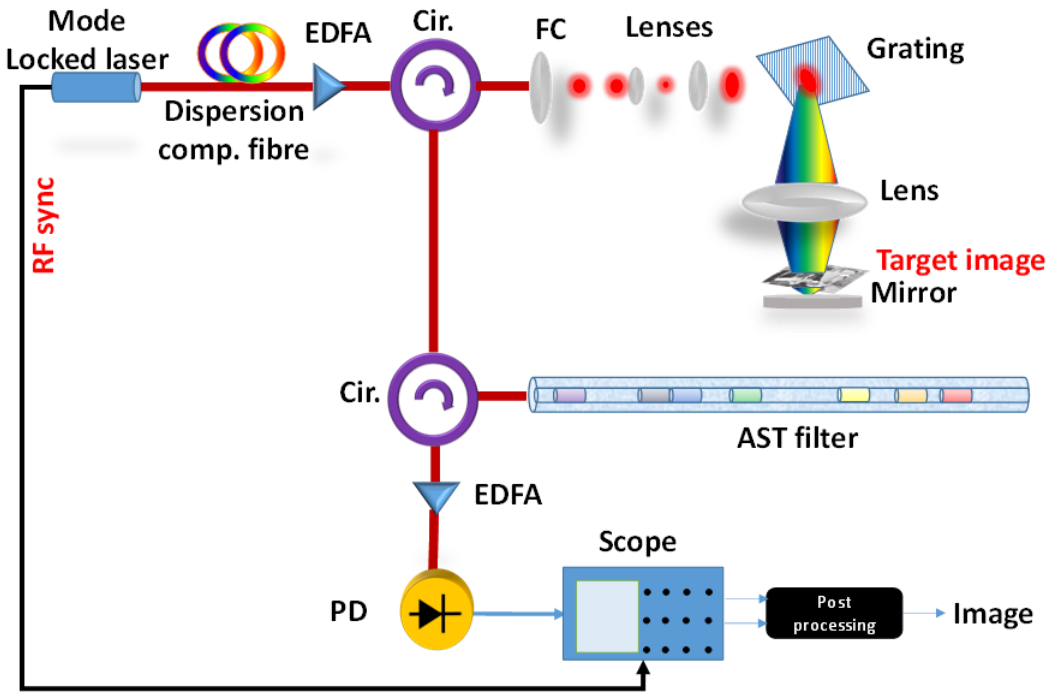

Fig. 2.5 Anamorphic stretch Transform in imaging

In Chapter 6, an alternative system has been proposed which can overcome this limitation of "Region of Interest". This can be implemented using a microwave photonic phase filter for pre-chirping the input RF signal and an AST filter to non-uniformly stretch the optical pulse carrying transformed RF signal. The microwave photonic phase filter with frequency-dependent time delay separates the high frequency (information-rich) part of an unknown microwave/RF signal from its low frequency components across the entire duration of the time limited signal. A following non-uniform PTS system based on AST filter is designed based on the spectral-temporal distribution pre-defined by the microwave photonic stretching filter. Without any knowledge of spectral-temporal distribution of the unknown RF signal and without reconfiguring the non-uniform stretch filter for different RF signals, the proposed approach enables reduction of TBP in blind detection of time-limited RF signals using this non-uniform photonic time stretch method.

2.2 Compressed Sensing

Compressed sensing(CS) [105, 106, 45, 107] is a signal processing paradigm based on proposition that natural images/signals have a sparse representation in a transformation domain (e.g. wavelet domain) and can be reconstructed from under sampled data or a reduced number of measurements in a single-pixel receiver scheme leading to overall compressed data volume. The overall CS detection of image in a nutshell has been illustrated in below Figure 2.6. The information is mixed with a binary spatial mask and focussed onto a single pixel

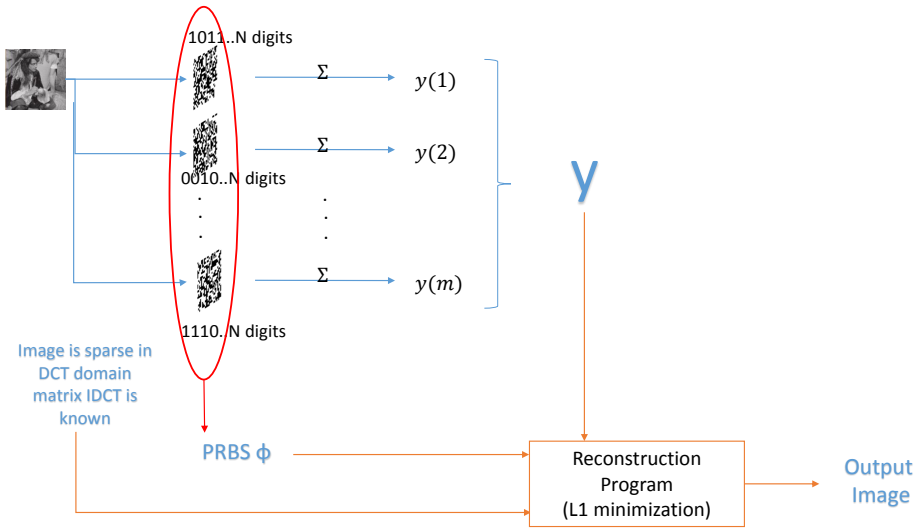

Fig. 2.6 Compressed sensing in a nutshell: Imaging example

photodetector which represents the dot product of the information vector with binary mask vector. The mask is refreshed with another binary sequence which is independent of previous mask and the process is repeated m times to obtain m measurements. In the post processing of l_1 reconstruction, the image is reconstructed by inputting the obtained dot products and the random masks which are used to obtain those dot products. Since the transformation domain in which the information is sparse and the length of the signal are known as priory,

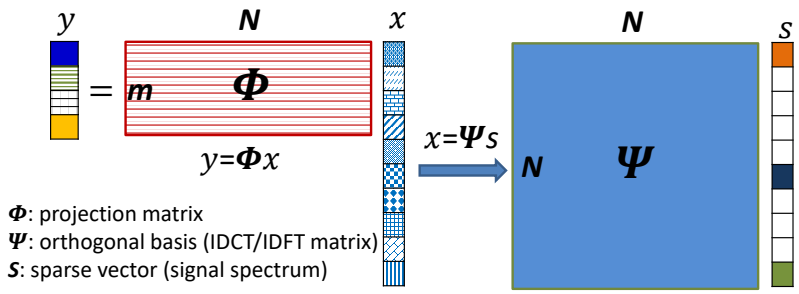

Fig. 2.7 Theory of CS in nutshell: Random mixing

the image or signal can be reconstructed faithfully without any need for high speed sampling equipment with reduced number of measurements achieving data compression.

2.2.1 Theory of Compressed Sensing

The theory of compressed sensing can be divided into three sub fields. (1) Sparsity of the input (2) Incoherence between the random sequences (3) Reconstruction of the signal [107].

Sparsity: A signal is said to be sparse if most of components are negligible or zero. Since the images are naturally sparse, they can be compressed using successful algorithms such as JPEG, MPEG by storing largest coefficients in some transformation domain such as DCT, DFT or wavelet domains to name a few. As an example, a 1D signal, x of length N, is considered to be the information to be sampled which is sparse in Discrete Fourier Transform domain $\psi_{N\times N}$, the DFT domain signal can be represented as,

$$s_{NX1} = \psi_{NXN} x_{NX1} \tag{2.12}$$

and the signal can be written as,

$$x_{NX1} = \psi^{-1}_{NXN} s_{NX1} \tag{2.13}$$

Problem of Compressed Sensing: Currently, if x is sampled at Nyquist rate acquiring N samples, it can be faithfully reconstructed. However, our aim in this method is to obtain x with fewer number of measurements. if x is assumed to be K-sparse i.e., $K << N$ in a transformation domain as shown in Fig. 2.7, general linear measurement process can be considered by computing $m < N$ inner products between signal x and a "certain" collection of vectors, ϕ_{mXN}. These vectors should be of length N, same as the information x. If the dot products are measured resulting in y, it can be represented as,

$$y_{m\times 1} = \phi_{m\times N} x_{N\times 1} = \phi_{m\times N} \psi^{-1}_{NXN} s_{NX1} = A_{m\times N} s_{N\times 1} \tag{2.14}$$

where $A = \phi\psi^{-1}$.

Random matrices: For stable reconstruction of information x, The set of collection of vectors ϕ_{mXN} should be a 2 dimensional random matrix such as independent random variables with equal probability and measurements m should satisfy following condition.

$$m \geq cKlog(\frac{N}{K}) \tag{2.15}$$

where c is a universal constant.

Reconstruction: Finally, the reconstruction of information can be executed by solving the minimization problem,

$$min(||s||_1) \quad subject\ to \quad y = As \tag{2.16}$$

results in sparse solution $\tilde{s}$. Since information length is known and the transformation domain in which the information signal is sparse is known, $\tilde{x}$ can be reconstructed. The compression ratio is defined as m/N.

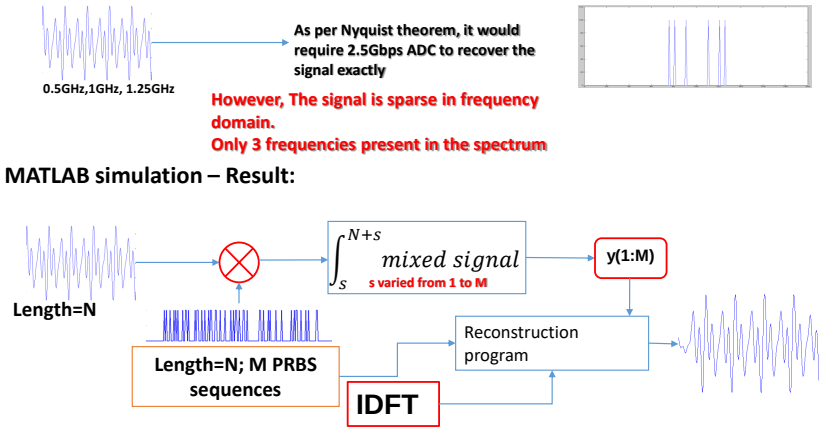

Fig. 2.8 Compressed sensing in 1D: Matlab simulation example

1D Example: As a simple illustration, a multi toned signal of duration 80ns has been considered with 0.5GHz, 1GHz and 1.25GHz as frequency tones. In normal scenario, a 2.5GS/s digitizer is required to sample the signal followed by quantizer for faithful reconstruction. Hence, signal length N can be defined as,

$$N = \text{Overall duration of the signal in sec} \times \text{Nyquist Sampling rate of the signal} = 200 \tag{2.17}$$

Instead of conventional sampling, if compressed sensing approach is used with the number of measurements chosen to be 20, the signal can be reconstructed making overall compression ratio as 10%.

The compressed sensing enables signal reconstruction with far less measurements than sampling at Nyquist rate. This saves storage space on the system for the acquired signal. This enables high speed acquisition as only 10% of the detector time is required, however post-processing time is longer than expected. This method depends on signal sparsity and estimated non-zero DFT coefficients in Fourier domain as explained in equation 2.15. Also, the front end is more complex as a Nyquist data rate incoherent random patterns need to be

generated and modulated onto the information. The acceptable compression ratio depends on threshold root mean square error for a number of signal measurements.

The quality of reconstruction of the result can be estimated by correlation or RMSE method in comparision with actual signal. In this thesis, we measured RMSE for 1D signals and MSE for images as a quantitative measure for CS reconstruction. However, the acceptable compresstion ratio for a CS system is determined based on number of factors such as non-zero coefficients in the transformation domain. The compression ratio varies for every signal/image as outlined in [108]. However, the acceptable compression ratio of CS system can be estimated based on testing with all combinations of signals. In this thesis, the acceptable compression ratio has been estimated based on signal/image under test based on RMSE or MSE measured against compression ratio. In [109], 90% correlation has been considered as baseline for preserving the reconstruction result through simulation results. In this thesis, an estimated compression ratio has been calculated in simulation results.

CS for imaging: If the information is an image is directly sampled in 2D, the explained theory slightly changed. A target 2D image $I_{N\times N}$ is mixed with m random patterns each of same size as target image, $\phi_{N\times N}$ where m also corresponds to number of measurements. By vectorizing the image into 1D as $I_{NN\times 1}$ and m random patterns as $(R_{m\times NN})$, the CS system can be simplified into 1D model. The image $I_{NN\times 1}$ assumed to be sparse in DCT domain, the measurement vector $y_{m\times 1}$ can be described as the dot product between the image and random patterns,

$$y_{m\times 1} = R_{m\times NN}.I_{NN\times 1} \tag{2.18}$$

Image $I_{NN\times 1}$ can be represented in transformation domain $\psi_{NN\times NN}$ as,

$$s_{NN\times 1} = \psi_{NN\times NN}.I_{NN\times 1} \tag{2.19}$$

where $s_{NN\times 1}$ denotes the transformation domain representation. Hence the equations can be summarized as,

$$y_{m\times 1} = R_{m\times NN}.\psi^{-1}s_{NN\times 1} = A_{n\times NN}.s_{NN\times 1} \tag{2.20}$$

where

$$A_{m\times NN} = R_{m\times NN}.\psi^{-1}_{NN\times NN} \tag{2.21}$$

In the reconstruction program, the measurement vector $y_{m\times 1}$ and $R_{m\times NN}$ are given as inputs and the transformation domain $\psi_{NN\times NN}$ is known, Hence $s_{NN\times 1}$ can be reconstructed using total variation minimization algorithm ,

$$(TV)_1 \quad min \quad TV(s) \quad \text{subject to } As = y \tag{2.22}$$

From the retrieved transformation representation output $\tilde{s}$, the image can be reconstructed as,

$$\tilde{I}_{NN\times 1} = \psi_{NN\times NN}.\tilde{s}_{NN\times 1} \tag{2.23}$$

and can be de-vectorized to get the 2D image $\tilde{I}_{N\times N}$. The compression ratio in this case, would be $\frac{m}{N^2}$.

Since the introduction of CS theory, there have been number of implementations [48, 110, 107, 111–114, 44, 115–117] with application in security, imaging and signal processing. Though the front end equipment such as random pattern mixer is complex, data compression can be achieved if information is sparse and very low speed detectors are sufficient for detecting high frequency information.

2.2.2 Photonic Implementation of Compressed Sensing

Due to high bandwidth availability and already existing imaging modalities in optics and photonics field, Photonic compressed sensing has become more of interest. Within the scope of this thesis, the Photonic compressed sensing has been categorised as 3 techniques.

1. Time Domain Photonic Compressed Sensing : Electronically generated random patterns are mixed with optical carrier in time domain with help of electro-optical interaction such as modulators.

2. Spatial Domain Photonic Compressed Sensing : The random pattern is generated in spatial domain. This can also be referred to as ”Structured Illumination based Compressed Sensing".

3. Spectral Domain Photonic Compressed Sensing : The random patterns are generated and mixed in spectral domain with help of diffraction gratings or spectral filters.

2.2.2.1 Time Domain Photonic Compressed Sensing

Photonic compressed sensing for image or signal detection can be acheived with electronically generated random patterns from high speed Arbitrary Waveform Generator and can be mixed with electro-optic modulator. This has been illustrated for imaging, blind spectrum sensing [118–124] using CW laser, pulsed laser or multi-wavelength laser with electro-optic modulation being the common element.

Compressed Sensing based Photonic Time Stretch (CS-PTS) enables optical information processing with compressed sensing. An example of Time Domain Photonic Compressed Sensing has been depicted in Figure 2.9.

A mode locked laser followed by dispersion compensating fibre is used as carrier which stretches the ultra-short pulse and maps to optical spectrum. The stretched pulse is amplified and directed to FC and magnified with beam expander setup. A diffraction grating (sometimes,

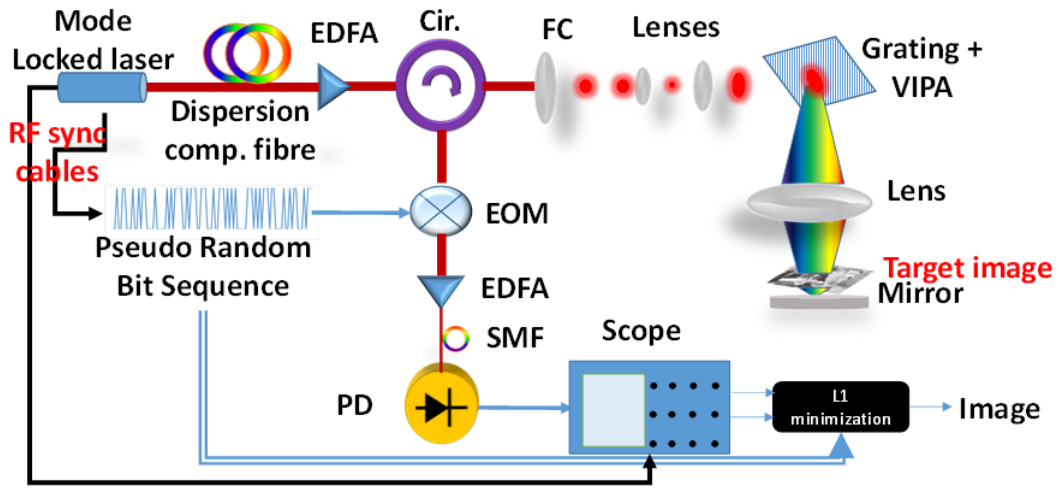

Fig. 2.9 Typical example of Time Domain Photonic Compressed sensing based on PTS for imaging application

may include Virtually Imaged Phase Array (VIPA)) is used to spatially disperse the optical wavelength to space and thereby, time to wavelength to space mapping can be achieved. If image is spatially encoded to this stretched pulse using lenses, the image/information can be encoded to spectral and temporal domains as well. The encoded pulse can then be directed to Electr-Optic MZM where a PRBS is encoded. The PRBS is generated in time domain from Arbitrary Waveform Generator or Programmable Pattern Generators. After mixing, the pulses are amplified and compressed using Single Mode Fibre (SMF) to represent the dot product of PRBS and encoded image. A low speed PD detects the power and sampled using low speed electronic scope. The process is repeated m times to obtain m measurements. By inputting PRBS sets and measurements, the image can be reconstructed in post-processing stage using $l_1$or TV minimization algorithms using DSP unit.

The applications of this method include RF spectral sensing [125] and imaging/microscopy [126, 127, 96].

In chapter 3, Time Domain Photonic Compressed Sensing method for OCT application has been discussed. In this case, simulation results have been presented for multilayer sample

and experimental results have been presented for single layer reflection sample enabling data compression with help of traditional PRBS based compressed sensing. A comprehensive analysis and further simulation and experimental verifications are presented.

Furthermore, a dual pulse integration method has been demonstrated to show the capability of improving frequency measurement resolution in the proposed system, leading to improved depth resolution in OCT measurement. A number of optimization algorithms for the reconstruction of the frequency domain OCT signals have also been compared in terms of frequency reconstruction accuracy and efficiency.

Time Domain Photonic Compressed Sensing method has been demonstrated for Linearly Chirped Fiber Bragg Grating (LCFBG) sensing OTS-FDR[28] which has been proved to be promising tool for high speed and high resolution fully distributed sensors due to its longer grating length and broader reflection bandwidth than uniform FBGs. However its capability is not only limited by the sampling rate of oscilloscope and the bandwidth of the Photodetector which are expensive to afford but also, occupies more memory with number of strain gauges to be measured and this data needs to be reduced to improve storage efficiency. These limitations can be addressed with the help of compressed sensing which acquires high speed RF signals with less number of samples than the Nyquist rate, thus, solving the big data problem and the need for high speed electronic equipment.

2.2.2.2 Spatial Domain Photonic Compressed Sensing

Compressed sensing can also be achieved by mixing in spatial domain which can be referred to as "Structured Illumination sensing"[128, 129]. This method is mainly used to sample images because of the spatial mixing involved. However, there have been demonstrations to reconstruct RF spectrum [130] using wavelength dependant speckle patterns from multimode fibre. In conventional image sampling, the image is acquired with CCD/CMOS camera. Single Pixel Imaging method enables to detect 2D image with low speed electronic sampler

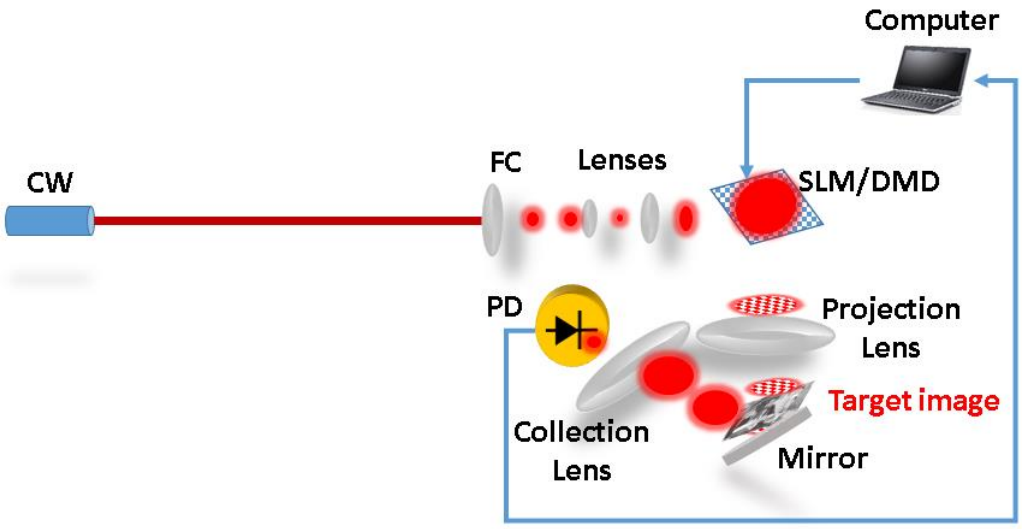

Fig. 2.10 Typical example of spatial domain Photonic Compressed sensing for imaging application

and digitizer without any significant reduction in quality. Spatial domain photonic compressed sensing can be regarded as a variant of single pixel imaging [44] where under-sampled measurements are used to detect the naturally sparse image enabling data compression. Another variant for single pixel imaging is "basis scan" where complete set of patterns either in Fourier domain or wavelet domain[59, 57] are illuminated onto the object to be sampled[59, 129]. This has been explained in section 2.3. For compressed sensing reconstruction, under sampled measurements are considered with independent random patterns. Generally these patterns are binary in nature and generated with SLM [130, 49, 51] or DMD [131, 132] which have low refresh rate but can work at single wavelength[129]. An example of typical Spatial Domain Photonic Compressed Sensing system is shown in Figure 2.10.

An optical carrier, generally a continuous wave laser generates light beam is directed to fibre collimator(FC) and magnified with beam expander setup. A spatial Light Modulator/Digital Micromirror Device induces random pattern to optical beam for some exposure

time. Using a projection lens, the encoded optical random pattern is encoded with image information. After reflection from mirror, the optical beam is focussed onto single pixel PD and interface unit collects power measurement and the process is repeated m times to obtain m measurements. By inputting random pattern set and measurements, the image can be reconstructed using l_1 minimization algorithms using DSP unit.

In [133], an ultra-fast resonance modulation scheme has been demonstrated based on wavelength dependant, non uniform cavity that can generate incoherent patterns with wide-band source. There have been demonstrations where instead of binary patterns using SLM or DMD, speckle patterns in multimode structure followed by 2D array of low speed Photodetectors have been implemented to sense multiple dot products at a single time instant [134] or using scattering medium [135] instead of multimode fibre with spatial impurity such as Zinc Oxide. The two dimentional PD array can be simplified by inducing impurities in fibre that have properties dependant on wavelength of the light as demonstrated in [136]. However, wavelength sweeping is limited in speed.

Since, the conventional structured illumination methods based on DMD,SLM or a liquid crystal array fall short in refresh rate, making it a real challenge for video rate and high-speed imaging applications, such as studying dynamic phenomena in living cells, neural activity, and microfluidics, and capturing important rare events, in chapter 4, the multimode fibre based compressed ultra-fast imaging system has been demonstrated where wavelength sweeping has been demonstrated with PTS method. Hence, a new approach for ultra-fast (20 Mfps) structured illumination single-pixel imaging has been made possible using light beam speckles out of a multimode fiber due to wavelength dependant multimode interference. The generation of incoherent 2D speckle patterns for a range of 500 wavelengths have been experimentally demonstrated. The incoherence among these patterns can be measured using cross-correlation result. For demonstrated wavelength-dependent optical speckle patterns, low correlation has been obtained which verifies the utility of multimode interference

based structured illumination in compressed sensing based single-pixel imaging. Ultra-fast wavelength sweeping is achieved by stretching optical pulses from a mode-locked laser using chromatic dispersion. Therefore, high imaging speeds can be achieved. Typical imaging speed is close to repetition rate of the modelocked laser which is few 10's of MHz or even GHz if number of wavelengths are sacrificed.

2.2.2.3 Spectral Domain Photonic Compressed Sensing

Photonic compressed sensing can also be achieved by manipulating the optical spectrum with random pattern sequence. While the Spatial Domain Photonic Compressed Sensing can be demonstrated for all optical sources, the spectral domain mixing can be done only for wideband sources such as broadband incoherent source[24], coherent mode locked laser[137], super-continuum sources or multi-wavelength laser source. Followed by time/spectral domain encoding of information, the pulses are spectrally encoded with random pattern through diffraction grating and SLM to binarize the optical spectrum with specific wavelength resolution (commercially available spectral filters). While the spectral filtering has been demonstrated using SLM[130], the refresh rate of SLM is relatively slow to obtain the measurements.

A typical example of Spectral Domain Photonic Compressed Sensing system is shown in Figure 2.11.

A wideband optical source is used as carrier, is amplified and directed to fibre collimator(FC) and magnified using beam expander setup. A diffraction grating is used to spatially disperse the optical frequency to space and thereby, time to wavelength to space mapping can be achieved. If image is spatially encoded to this stretched pulse using lenses, the image/information can be encoded to spectral and temporal domains. The encoded pulse can be directed to Spectral Shaper where the spectrum is modulated with electronically generated PRBS. After mixing, the pulses are amplified and sensed in time domain using low speed

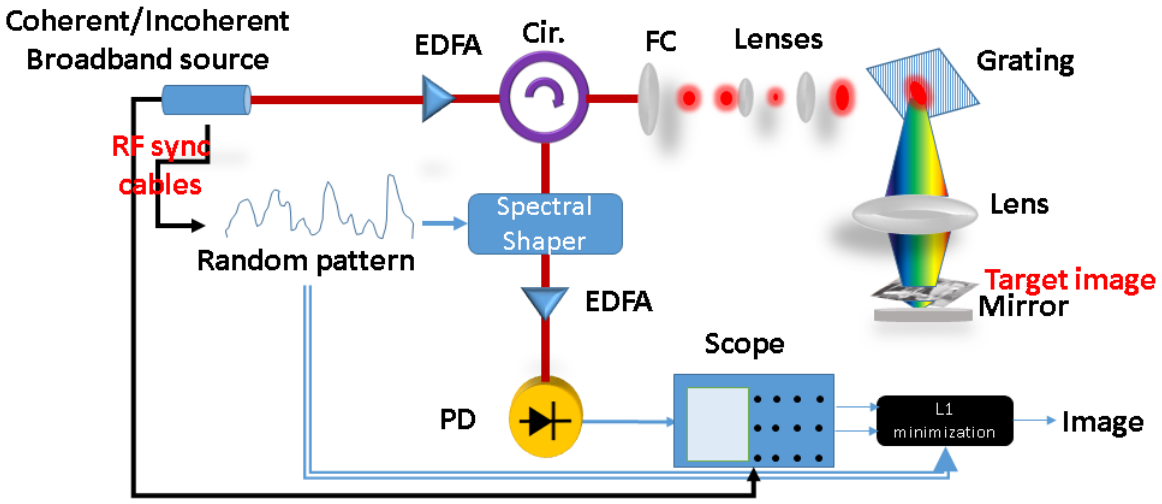

Fig. 2.11 Typical example of spatial domain Photonic Compressed sensing for imaging application

photodetector followed by electronic scope. The process is repeated m times to obtain m measurements. By inputting PRBS sets and measurements, the image can be reconstructed using minimization algorithms in post-processing stage using DSP unit.

In any compressed sensing system, mixing information with repeatable and deterministic random sequences is a crucial step in implementing Photonic Compressed Sensing. Current traditional technologies like PRBS mixing, SLM/DMD are either expensive or slow. To completely eliminate electronic bottleneck in Photonic Compressed Sensing, all-optical approaches are highly demanded. This will have multiple advantages such as (1) Achieving data compression (2) Reduction in overall system cost (3) Improved energy efficiency as loss can be significantly reduced (4) Reduction in physical size as commercially available electronic generators are bulky.

In section 3.2, a novel all-optical random sequence generation and mixing approach has been presented for Spectral Domain Photonic Compressed Sensing system for detection of RF signals. In contrast to spatial-domain and time-domain random mixing solutions, random sequence generation using a spectral filter based on wavelength-to-time mapping

in time stretched optical pulses have been proposed. The spectral filter will provide various reproducible random spectral response. This is made possible by using two cascaded dispersion-unbalanced MZIs. The overall spectral response represents a broadband random spectral pattern. Owing to the dispersion-induced wavelength-to-time mapping, spectral random filtering enables equivalent temporal mixing of RF signals and all-optically generated random sequences. Fast tuning of the overall spectral response is realized by changing the optical time delay module within the MZIs. This method avoids high-speed electronic PRBS generator and modulator, electronic bottleneck in random mixing has been overcome and is also cost effective. With this approach, lossy electro-optic mixing using MZM, bulky Arbitrary Waveform Generator (AWG) and EDFA can be avoided enabling increased energy efficiency. However, the random spectral filter requires one time calibration using high speed electronic detector before performing actual measurements. The challenges are to control the phase instability in interferomteric structure and designing the fast tunable optical delay element. This technique was experimentally demonstrated for blind RF spectrum sensing and proposed the system's utility for FBG sensing signals with numerical demonstrations.

As an alternative to our proposed system, there has been research on generating such spectral domain random patterns through customized photonic integrated chip with the help of microring resonators[138, 139] which requires customized fabrication.

2.3 Signal Sensing with Fourier Spectrum acquisition

As mentioned in [44], Single Pixel Imaging reduces the required size, complexity and cost of overall system. In addition to sensing flexibility, the single pixel imaging system utilizes higher quantum efficiency of photodiode as compared to conventional CCD/CMOS camera and that the fill factor of a DMD is more than CCD/CMOS array. In general, there are three types of scanning methods in this technique. (1) Raster Scan: Single pixel detector takes equal number of measurements as number of pixels and reconstructs the image. (2) Basis

Scan: A single sensor takes equal number of measurements from different combinations of the pixels as determined by scanning function such as harmonic sinusoidals. (3) Compressed Sensing: A single sensor take number of measurements less than number of pixels and image is reconstructed through l_1 minimization algorithms. In general, CS approaches fall short in two aspects: (1) Nyquist rate random/speckle patterns are required for random mixing. (2) By its nature, CS approach only works for sparse signals.

In this section, Single Pixel Imaging through Basis Scan approach has been discussed. Unlike CS, the object is illuminated with complete patterns associated with particular basis. The basis can be Fourier scan[56, 55], wavelet scan[140], wavelet based on Haar transform [59] or hadamard basis[57]. However, the processing time is very slow due to the limitation of the components used. Previous methods utilizes either Programmable pattern generator which is limited in bandwidth and expensive[59, 55] or Digital MicroMirror Devices[57] which are limited in speed.

In this section, N-step phase shifting($N = 4$) sinusoidal structured illumination has been presented for Fourier basis scan as illustrated in [56, 55]. In general, the method can be demonstrated for $N \geq 3$ [56].The method with N=4 has been illustrated below.

Theory of Signal sensing with Fourier spectrum acquisition: The information signal either a 1D RF signal or a vectorized 2D image denoted as $x_{N\times 1}$ with sampling time of δt. Here, Number of samples$N$ is relative term dependant on speed of signal generator. Instead of sampling the signal with binary patterns as in CS method or traditional Nyquist sampling method, 4-phase shifted sinusoidal patterns are considered for mixing and the dot product of both vectors is considered as measurement that can be acquired with very low speed photodiode and electronic digitizer. The sampling illumination patterns are harmonic frequencies whose fundamental frequency is inverse of overall length of the information signal $x_{N\times 1}$, f.

$$f = \frac{1}{N \times \delta t} \tag{2.24}$$

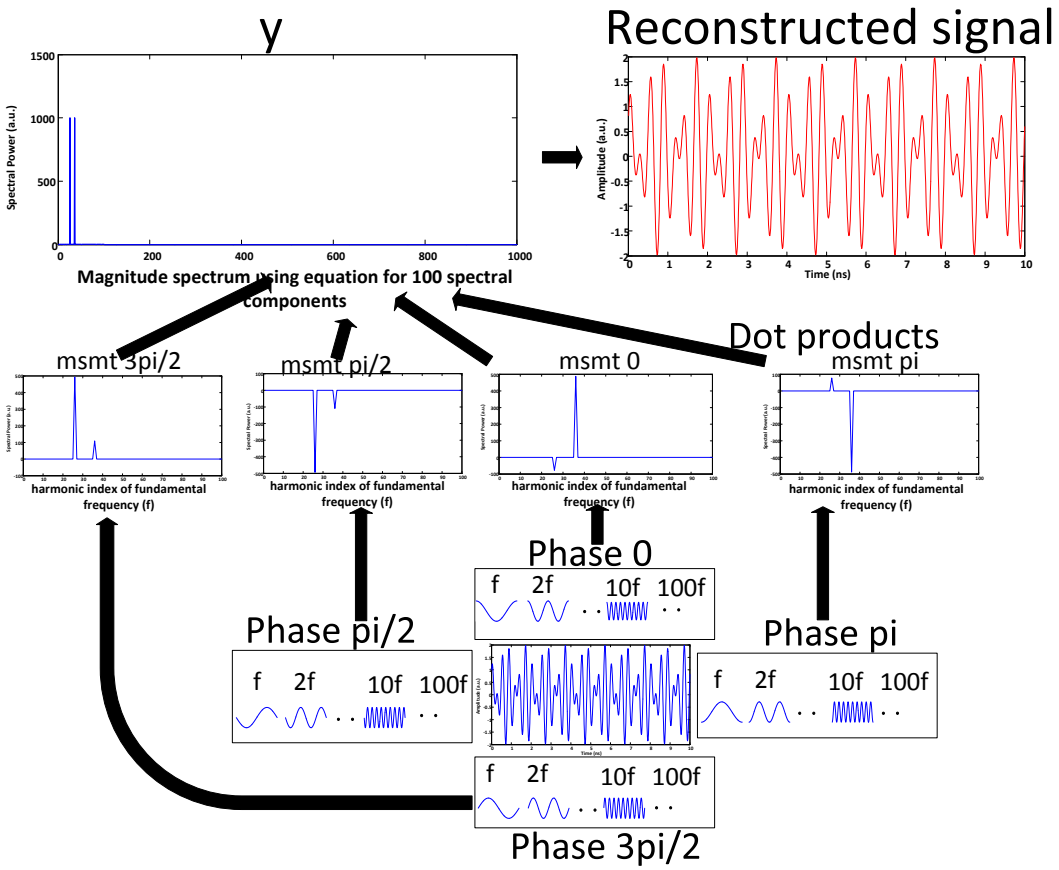

Fig. 2.12 Signal sensing by Fourier spectrum acquisition : Matlab simulation example

When signal x is multiplied with cosine signal of frequency f and phase 0, and overall summed power measured as $msmt_0$,

$$msmt_0 = x_{N\times 1}.cos(2\pi fN\delta t) \tag{2.25}$$

Similarly when phase shifted by $\frac{\pi}{2}$,π,$\frac{3\pi}{2}$, the measured powers are denoted as below.

$$msmt_{\frac{\pi}{2}} = x_{N\times 1}.cos(2\pi fN\delta t + \frac{\pi}{2}) \tag{2.26}$$

$$msmt_{\pi} = x_{N\times 1}.cos(2\pi fN\delta t + \pi) \tag{2.27}$$

$$msmt_{\frac{3\pi}{2}} = x_{N\times 1}.cos(2\pi fN\delta t + \frac{3\pi}{2}) \tag{2.28}$$

Combining above equations, the spectral component at the frequency f can be obtained as,

$$y = (msmt_0 - msmt_\pi) + j(msmt_{\frac{\pi}{2}} - msmt_{\frac{3\pi}{2}}) \tag{2.29}$$

Taking m measurements by tuning the frequency from f to $f \times (N-1)$,

$$y_{m\times 1} = (msmt_0 - msmt_\pi)_{m\times 1} + j(msmt_{\frac{\pi}{2}} - msmt_{\frac{3\pi}{2}})_{m\times 1} \tag{2.30}$$

The reconstructed image or signal can be obtained by computing inverse Fourier transformation of $y_{m\times 1}$. The compression ratio is $\frac{4m}{N}$.
This has been illustrated with a simulation as shown in Figure 2.12.

Due to the limitations of speed and cost involved in several approaches, all-optical methods for Fourier basis scan is highly desired. In chapter 5, an all-optical PTS approach for Fourier spectrum acquisition has been proposed and experimentally demonstrated for broadband RF signal detection based on spectral shaping using MZI. Without using any high-speed electronic signal generator, modulator and photodetector, this method achieves data compression and completely eliminates the electronic bottleneck in high-speed RF spectrum sensing. Though this method is an alternative for aforementioned methods such as compressed sensing and AST, the record time is longer. However, the information can be obtained without any need for random sequence. The system capturing bandwidth increased to 150GHz hence the system's bandwidth is limited by signal sensing MZM whose bandwidth is limited [141].

Other than aforementioned methods, the data compression can also be achieved by collecting changes in sequence of scans such as run-length encoding [142].

Chapter 3

Photonic Compressed Sensing for Data Compression

This chapter discusses research work on application of two approaches of Photonic implementation of Compressed Sensing systems explained in chapter 2. (1) Time Domain Photonic Compressed Sensing system (abbreviated as TD-PCS) for Optical Coherence Tomography and FBG sensing. (2) An improved approach for Spectral Domain Photonic Compressed Sensing (abbreviated as SD-PCS) has been proposed and demonstrated for blind RF spectrum sensing and FBG sensing.

3.1 Time Domain Photonic Compressed Sensing for Optical Coherence Tomography

In this section, the method of Time Domain Photonic Compressed Sensing for Optical Coherence Tomography(abbreviated as TD-PCS-OCT) system has been experimentally demonstrated. In following subsections, background on OCT systems has been presented followed by our approach of achieving data compression in OCT system by using time

domain photonic compressed sensing mechanism.

Remainder of this section 3.1 is an extended or modified versions of published papers [65, 63, 61, 64].

3.1.1 Background on Optical Coherence Tomography

Optical coherence tomography (OCT) is an indispensable tool for high-resolution volumetric scanning of the internal structure of an object. Since its invention [92], OCT has been used and further improved as an *in-vivo* diagnostic tool for biological tissues such as ocular structures [93] with resolution of few micrometers, finer than conventional ultrasound scanning as illustrated in Fig. 3.1. OCT measures reflection profile of optical beam which is termed as Axial Scan or A-scan. By measuring several A-scans produces B-Scans and stack of several B-scans produces volumetric scanning.

OCT has applications in different fields depending on the wavelength regime used. OCT at visible wavelengths are mainly used in biomedical fields[143, 144]. OCT at 1050 nm has applications in biomedical field that requires deeper penetration and enhanced imaging range[145].The optical wavelengths around 1300 can be used for applications requires deeper penetration but limited by water absorption. OCT at long wavelengths from 1300nm to 1550nm and above is mainly used for industrial applications for Non-Destructive Testing, material characterization and imaging the paintings[146]. Recently, 4μm OCT has been demonstrated for analysing metallic structures[147]. In this thesis we discuss OCT in 1550nm regime for proof of concept application in Non Destructive Testing.

As shown in Fig 3.1, the resolution is improved for OCT system in comparison with standard clinical practices such as MRI,CT, Ultrasound and the penetration depth is improved compared to confocal microscopy. On the other hand, since OCT provides high-resolution

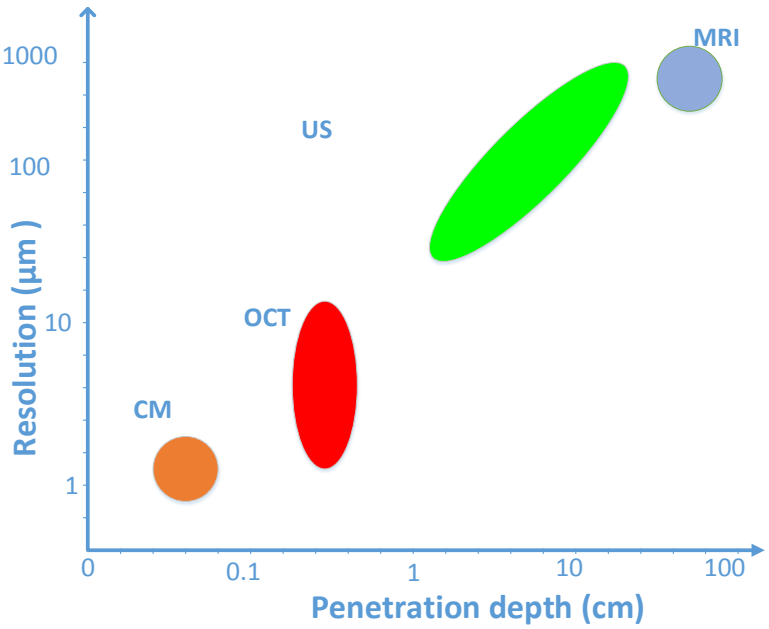

Fig. 3.1 Comparison of different biomedical imaging methods. CM:Confocal Microscopy, OCT: Optical Coherence Tomography US: UltraSound MRI:Magnetic Resonance Imaging

depth-resolved images of strongly scattering media in a contact-free way, this technique has also been proposed for non-biological applications, such as non-destructive testing (NDT) and contactless material characterization [148]. High-speed OCT is highly desirable for NDT applications where fast image acquisition is essential. Examples include observation of rapid dynamic processes and inspection of fast moving objects without motion artifacts.

The discovery of Fourier-Domain OCT (FD-OCT) has provided higher scan rates, offering greater stability and better signal-to-noise ratio compared to traditional time domain OCT methods [149]. In the last decade, extensive efforts have been made to increase the utility of FD-OCT towards further higher measurement speeds. Impressive MHz axial scan rates have been achieved by using a new type of high-speed frequency-sweeping optical source based on Fourier-domain mode locking (FDML) [150], and by using optical channelled spectrum measurement [151]. An FDML laser consists of longer cavity length, a semiconductor amplifier and a tunable Fabry-Perot filter enabling higher scanning speed. Apart from

targeting high-speed axial scanning, Master-Slave interferometry [152] was recently reported as an alternative high-speed solution for real-time *en-face* display of frequency-domain OCT images. FD-OCT can be subdivided as Spectral Domain OCT (SD-OCT) and Swept Source OCT (SS-OCT). In SD-OCT, a broadband light source is used in combination with spectrometer[15, 12]. In SS-OCT, a tunable light source is used in combination with high speed photodetector[12].

In this thesis, SS-OCT has been mainly focussed followed by Photonic Time Stretch OCT method which is considered to be a variant of SS-OCT. In general, any SS-OCT measurement system is ideally expected to be :

1. Ultra high axial resolution determined by the tuning bandwidth and source wavelength
2. High axial scan(A-scan) range which depends on the line width of each of the source wavelength while penetration depth depends on sample's absorption/reflection spectra.
3. High Sensitivity which depends on the interference of the reflection profile with the reference optical beam which depends on the optical line width and receiver's sensitivity
4. High A-scan rate/ high A-scans per sec which depends on the wavelength sweeping speed of the source.
5. Lower number of acquisition data samples for an OCT signal to be stored.
6. Within the sampling range of the detector which is a photodetector.

To address high speed A-scan rates, PTS technique has also been explored [153–156]. As explained in chapter 2, this method uses large chromatic dispersion in optical fibres to map the broadband spectrum of an ultra-short optical pulse into a temporal waveform. Therefore, frequency-domain OCT measurement can be achieved alternatively in time-domain using a high-speed single-pixel photodetector (PD), which enables PTS-OCT to operate at the

axial scan rate equivalent to the pulse repetition rate of the laser, typically ranging from tens of MHz to even GHz. PTS-OCT was first implemented in the fiber-optic communication band (i.e., ∼1550 nm) [153], in which ultrafast PDs and good dispersive elements with large dispersion-to-loss ratio are commercially available. PTS-OCT operating at a shorter wavelength range has also been implemented offering better axial resolution and less water absorption in biological samples [154]. Amplified time stretch OCT with greatly improved sensitivity based on broadband Raman amplification has been recently demonstrated to allow high-speed OCT imaging of biological tissues [155, 156].

While the PTS technique has enabled high-throughput OCT measurement due to the use of high-speed hardware, the instruments inherently produce an extremely high-rate data volume. For example, for a PTS-OCT system running at an axial scan rate of nearly 100 MHz [154], with each OCT waveform having one thousand sampled pixels, and a high-speed ADC with a typical 10 bits of digitization accuracy [76], the produced data rate can be as high as one trillion bits per second. This deluge of OCT image data will overwhelm even the most advanced data acquisition circuits in acquiring high speed data and the backend digital signal processors in processing this huge information.Therefore, new and efficient photonic approaches, to address this extremely broadband bandwidth, emerging massive data problems in ultra-fast OCT systems.

If the Axial scan(A-scan) of PTS-OCT produces a sparse reflection profile with only few peaks in transformation domain, Compressed sensing can be used to reduce the number of samples per A-scan for a set of random patterns and this can be extended to entire volumetric scanning. As a result of reduced number of samples, the overall scanning time can be reduced. For detecting the samples, a very low speed photodetector can be used. However, the process requires 2 additional components compared to PTS-OCT. A high bandwidth AWG is needed to produce high speed random binary sequence and an electro-optic modulator is required to modulate the electrical random sequence to optical carrier.

To reduce the number of samples, research efforts have also been made to explore the use of CS method in OCT systems for data compression. For example, in [157], a CS method has been employed in post processing to reconstruct 3D OCT images from a subset of the original images by exploiting the image sparsity in certain transform domain. In [158], CS has been implemented in spectral domain OCT to reduce the total amount of original data from a CCD camera. The random under-sampling of OCT spectral data was achieved by randomly addressing the pixels in the CCD camera or applying a pre-set k-space mask [159]. Various reconstruction algorithms based on non-local approach [160] and energy-guided learning approach [161] have been studied to produce better reconstruction results from under-sampled data sets. Graphics processing units (GPU)-based parallel processing has improved reconstruction speed and achieved real-time CS spectral domain OCT [162].

In this work, TD-PCS method has been explored and experimentally demonstrated for application of Optical Coherence Tomography (abbreviated as TD-PCS-OCT) to address high speed A-scan rate requirement and low sample acquisition. Thus, basic limitation of Nyquist-Shannon sampling principle has been overcome at the detection unit and importantly the need for high speed electronic detectors has been reduced. Both random mixing and signal integration are implemented in the optical domain based on temporal modulation of time stretched optical pulse using PRBSs and pulse compression using SMF with opposite dispersion value. The proposed method not only overcomes the bottleneck of big data problems [163] but also provides an economic alternative to high-speed PTS-OCT data acquisition as a very low speed (50MHz) detector is capable enough to capture compressed OCT data, which otherwise demands tens of GS/s sampling rate [153–156].

Note: Conventionally TD-OCT is a method that has been developed for OCT volumetric scanning in time domain. However, in this context, Time domain should be understood as time domain photonic compressed sensing method developed for photonic time stretch OCT method.

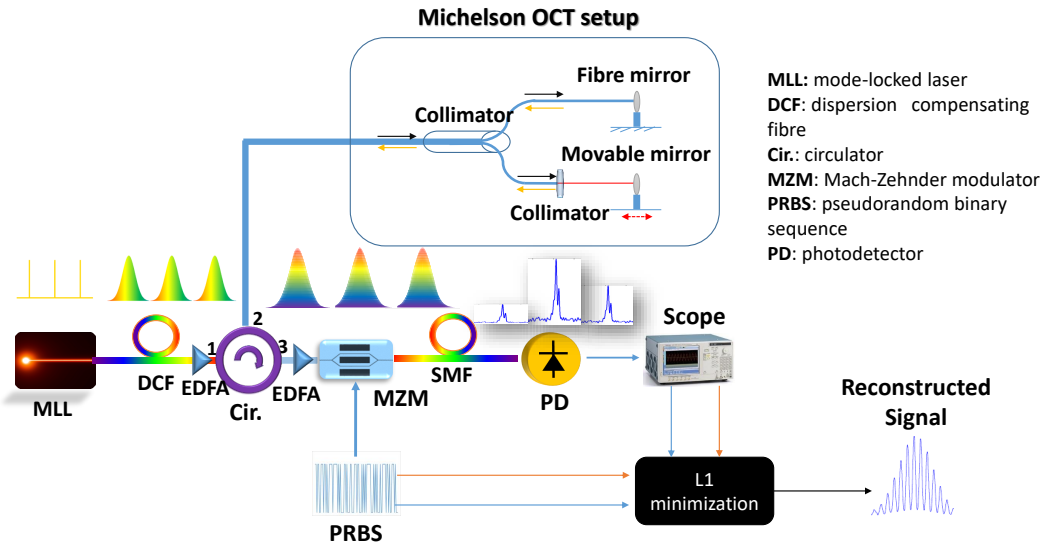

Fig. 3.2 Block diagram of the proposed TD-PCS-OCT experimental setup.

The remainder of this section is organized as follows. the principle of the proposed TD-PCS-OCT system has been described in detail. The simulation results to verify the optical system for randomization and integration with reconstruction algorithm has been presented in section 3.1.3. Experimental demonstration of data compressed PTS-OCT for a single-layer sample with various depth profiles is carried out and presented in section 3.1.4. A new optical compressive sensing scheme based on dual pulse compression to improve the reconstruction frequency resolution is demonstrated and reported in section 3.1.5. Synchronization procedure followed in our system has been presented in section 3.1.6. In section 3.1.7, our evaluation of a number of reconstruction algorithms for TD-PCS-OCT is presented. Discussions on potential improvement in compression ratio are provided in section 3.1.8. Finally, the work is summarized in section 3.1.9.

3.1.2 Principles

Schematic diagram of our proposed TD-PCS-OCT system is shown in Fig. 3.2. The optical source is a passive MLL that produces a series of broadband ultra-short optical pulse train. The optical pulse is first stretched by a DCF generating a broadband passive wavelength swept optical carrier. The stretched pulse is amplified and sent to a Michelson interferometer for real-time spectral-domain OCT measurement. Each frequency component of the pulse spectrum hence illuminates the sample successively in time. The back-reflected pulses from different layers of the sample are interferometrically combined with an unmodulated pulse reflected from a reference mirror at the optical coupler, resulting in an interference fringe in the time domain. The concept of PTS-OCT can also be understood based on frequency or wavelength-to-time mapping: depth information of the sample is first encoded to optical pulse spectrum, which is further mapped to a temporal waveform by large group velocity dispersion (GVD) of the DCF. The wavelength-to-time mapping relation is written as ,

$$y(t) = X(\omega)\Big|_{\omega=\frac{t}{\ddot{\Phi}_0}} \tag{3.1}$$

$$\omega = \frac{t}{\ddot{\Phi}_0} \tag{3.2}$$

$$\Delta\lambda = \frac{\Delta t}{\ddot{\Psi}} \tag{3.3}$$

where $\ddot{\Psi}$ is the total chromatic dispersion (in ps/nm) of the DCF. Finally a spectral interferogram can be captured in real time using a high-speed single-pixel photodetector.The spectrum of each broadband pulse are one-one mapped to the temporal domain by large Group Velocity Dispersion (GVD), $\ddot{\Phi}_0$ of the DCF as explained [77] and in chapter 2 and re-iterated with equation 3.3.

Interferometric setup: In the Michelson-type interferometer set up, one optical fibre arm ends with a fixed fibre Faraday mirror and other arm is focused onto a moveable mirror, which emulates a single reflection-layer sample. This interferometer set up produces an interference fringe pattern in both the time and frequency domains. The optical path length difference between two arms is considered to be

$$\Delta l = (n_g L - L_1) \tag{3.4}$$

where n_g is the refractive index of the fibre in the fixed arm, L is the optical fibre length in fixed arm, L_1 is the free space length between the collimator and the tunable mirror. Free spectral range(FSR) in terms of frequency and wavelength can be calculated as,

$$\Delta \nu = \frac{c}{2\Delta l} \tag{3.5}$$

$$\Delta \lambda = \frac{\lambda^2}{2\Delta l} \tag{3.6}$$

From equations 3.3 and 3.6, the relation between RF frequency of the interference pattern and optical path length difference can be established as,

$$f_{RF} = \frac{1}{\Delta t} = \frac{2\Delta l}{\lambda^2 \ddot{\Psi}} \tag{3.7}$$

Therefore, the optical path length difference and hence the depth information of the sample can be uniquely determined from the RF frequency at a refresh rate identical to the pulse repetition rate.

As explained in section 2.2, Compressed sensing theory shows that a frequency-sparse signal, such as the time-encoded OCT signal, can be recovered from a reduced number of measurements in a single-pixel receiver scheme such as the PTS-OCT system, which leads to significant data compression if incoherent set of random patterns are used. This normally

involves three successive steps [45]: random pattern mixing, integration, and down-sampling. The original signal can be then reconstructed following a minimization algorithm as explained in chapter 2. To implement TD-PCS system, each of the spectrally encoded optical pulses are modulated with a pseudo-random bit sequence (PRBS) using an electro-optical modulator. The bit rate of the PRBS defines Nyquist rate of the detection system.

3.1.3 Simulation Results

A simulation is first performed using a commercial simulation tool VPItransmissionMaker to verify the method. The schematic shown in Fig. 3.2 is considered and the input optical pulse is assumed to have a Gaussian shape with a full-width at half maximum (FWHM) of 800 fs and repetition rate of 50MHz, and the DCF has total dispersion of 1.28 ns/nm. The original ultra-short optical pulse is significantly stretched in time after dispersion as shown with dashed line envelop in Fig. 3.3.a. The sample used in the simulation has a two-layer structure with a layer-to-layer separation of 0.768 mm. After reflection from the Michelson interferometer, the spectral interferogram is mapped to a time-domain waveform due to the frequency-to-time mapping. The obtained waveform is shown in Fig. 3.3.a with solid line. Since reflection from each layer within the sample turns into unique frequency with respect to the reference arm, each path length difference converts to a single-tone RF frequency in time domain. Fig. 3.3.b shows the corresponding Fourier spectrum, which has two strong frequency peaks at 4 GHz and 3.5 GHz respectively. The power of the peaks indicates the strength of reflection from individual layers. An excellent match with the given model in Eq. 3.7 is observed. Note that there is an additional frequency component close to the baseband, which is corresponding to inter-layer interference and can be removed during post-processing.

The encoded and stretched optical pulse carrying depth information is then mixed with a PRBS pattern of 10 Gbps, which leads to an original signal length of N=200. Signal integra-

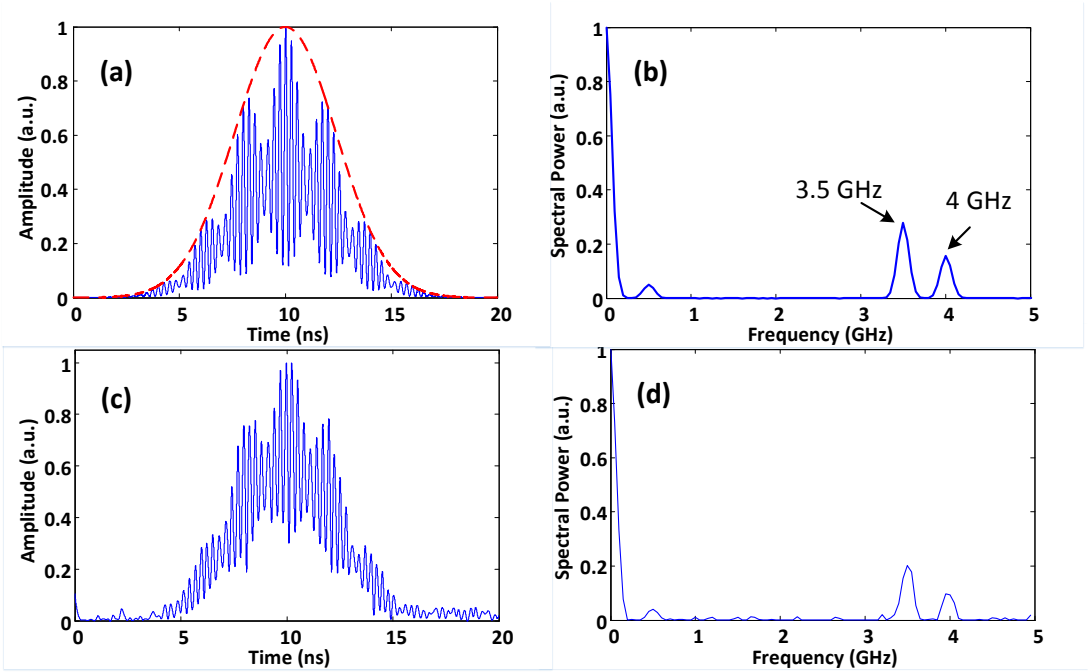

Fig. 3.3 Simulation results for a two-layer PTS-OCT measurement. (a) Temporal interference pattern as a result of path length difference. The time-stretched original pulse is shown in red dotted line. (b) The spectrum profile of the optical interference pattern, clearly showing two carrier frequencies of 3.5 GHz and 4 GHz. (c) The reconstructed signal in time domain using 70 measurements. (d) The reconstructed Fourier spectrum showing two strong tones which match with the original signal.

tion is realized based on pulse compression using a Single mode Fibre (SMF) with opposite dispersion profile, which generates a single measurement result. Multiple measurements are implemented with different PRBS patterns and used to run l_1 minimization reconstruction. By taking 70 measurements, the reconstructed DFT domain signal is shown in Fig. 3.3.d and corresponding time domain representation is calculated using inverse Fourier transform and shown in Fig. 3.3.c. It is evident that a good reconstruction is obtained with a compression ratio of 35%.

3.1.4 Experiment Results

To verify the utility of the proposed TD-PCS-OCT system, a proof of concept experiment has been designed and implemented based on the setup shown in Fig. 3.2. In the experiment, the optical source is a passively mode locked laser (Calmar Mendocino FP laser), which produces a series of ultrashort optical pulses with FWHM of 800 fs and repetition rate of 50MHz at central wavelength 1550nm with optical bandwidth of 12nm. After being time stretched using a DCF(OFS SMFDK-S-020-03-01) with total dispersion of -1.04ns/nm, the optical pulses are amplified and directed to a Michelson-type OCT setup where one arm is an optical fibre ended with a fibre Faraday mirror and the other is in free-space towards a moveable mirror emulating as a single-layer sample. Tuning to a particular path difference, the depth profile is encoded into the RF frequency of the mapped temporal waveform.

The first five consecutive pulses are captured using a high-speed PD and a real-time oscilloscope and shown in Fig. 3.4.a. The stretched Gaussian pulse is encoded with a single tone RF frequency indicating the strong single-layer reflection from the sample. The Fourier transform of the interference waveform is indicated by the red dotted line in Fig. 3.4.e. A clear peak at 650 MHz is obtained, which corresponds to an optical path length difference of 0.81 mm. PRBS patterns at 2.5 Gbps are generated by an arbitrary waveform generator (AWG, Tektronix AWG7122C) as shown in Fig. 3.4.b. Considering Nyquist rate of 2.5 Gbps and pulse period of 20 ns, the original signal length is N=50. Mixing of PRBS patterns with the encoded optical pulses is implemented using a 10 GHz MZM with the results captured by the oscilloscope and shown in Fig. 3.4.c. Passing the randomly mixed pulses through a SMF with opposite dispersion profile, signal integration has been realized via pulse compression. The compressed pulses are detected with a 2.5GHz PD and shown in Fig. 3.4.d. The pulses have a pulse-width of 0.4 ns which is inversely proportional to the PD bandwidth. The peak power of each pulse indicates the integration of mixed optical pulse and leads to a single measurement result. Overall 33 measurements have been taken to reconstruct the

original signal following an l_1-Magic minimization algorithm as described in [112]. The reconstructed DFT domain signal is shown with solid line in Fig. 3.4.f. The target frequency (650 MHz) has been successfully recovered with a compression ratio of 66%. Fig. 3.4.e shows the reconstructed time domain signal and the original signal with blue solid and red dotted line respectively. A good match in time-domain reconstruction has been achieved and data compression is achieved in system at the cost of reduced axial scan rate. The effective axial scan rate in this experiment is 1.51 MHz. A better compression ratio (due to fewer number of measurements) will increase the scan rate as number of pulses required are reduced.

A second experiment was carried out to verify the utility of the system at different imaging depths. The moveable mirror is tuned further to get an increased optical path length difference of 0.99 mm. The mapped spectrally-encoded optical pulse has a higher carrier frequency of 800 MHz, with its time-domain and frequency-domain representations shown in Fig. 3.5.a and 3.5.b respectively. The same random mixing and optical pulse compression processes are carried out. With 33 measurements, the reconstructed time-domain and DFT domain signals are shown in Fig. 3.5.c and 3.5.d respectively. The reconstructed signal matches well with the original signal with a compression ratio of 66%.

3.1.5 Time Domain Photonic Compressed Sensing for OCT with Improved Resolution

As demonstrated, the TD-PCS-OCT system achieves significant data compression. However, it suffers from one difficulty that it can only reconstruct discrete frequency tones (a frequency grid) in the OCT spectrum, which are harmonic tones of the laser repetition rate, due to the periodic nature of the optical pulse train. The minimum frequency resolution that can be resolved is as same as the repetition rate [48]. If the RF frequency is near a midpoint of the

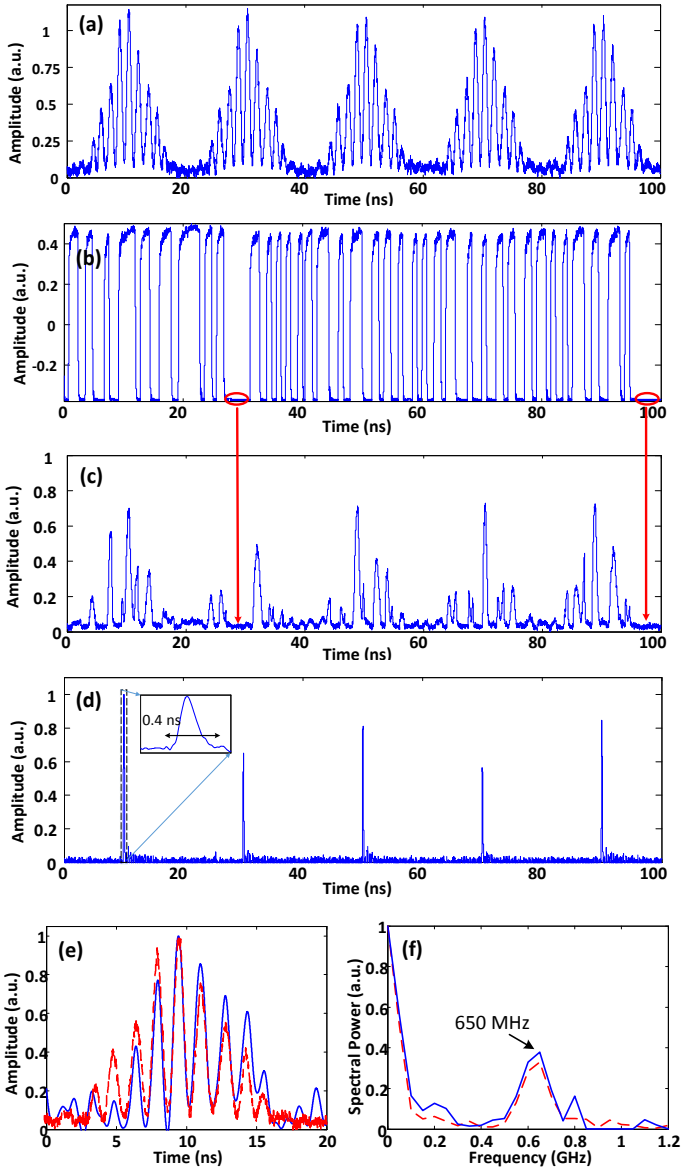

Fig. 3.4 Experiment results for a single-layer PTS-OCT measurement. (a) The temporal interference pattern for five successive pulses. (b) The first 5 PRBS patterns. (c) The modulated waveforms with red marking showing no pattern for exact amount of duration of a bit 0. (d) The compressed optical pulses using a SMF with opposite dispersion profile. The peak power of compressed pulses produce the measurements. (e) Overlapped temporal waveforms for the reconstructed signal (in solid line) and the original signal (in red dash line). (f) Fourier domain representation of the reconstructed signal (in solid line) and the original signal (in red dash line).

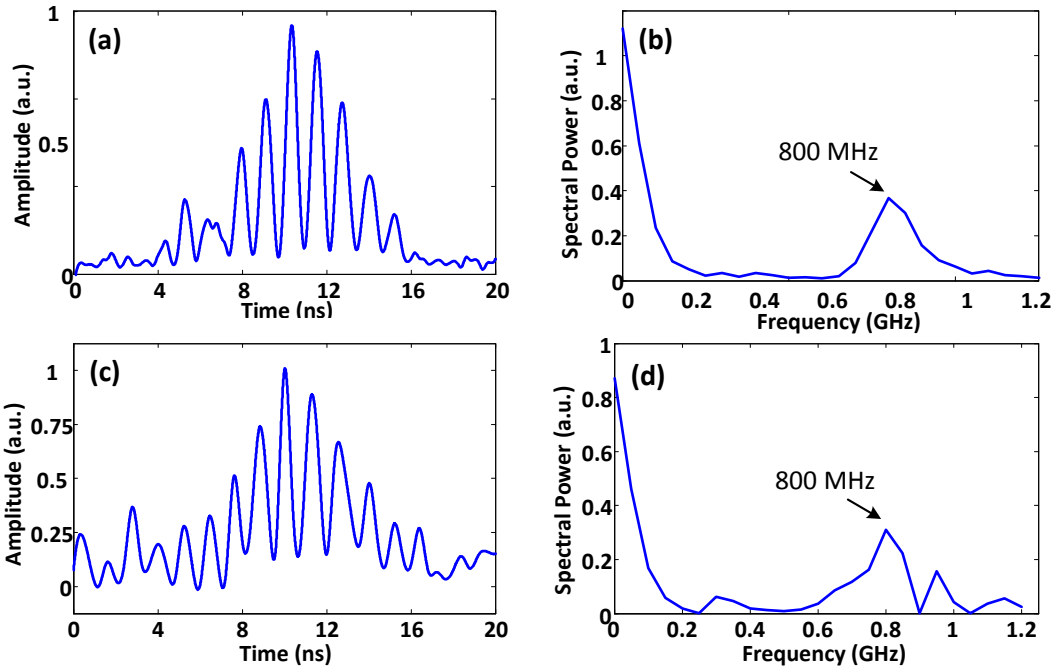

Fig. 3.5 Experimental results for a second single-layer sample with different path length difference. (a) The original interference pattern in time domain. (b) Fourier transform of the original interference pattern showing a single carrier frequency of 800 MHz. (c) The reconstructed time domain waveform with 33 measurements. (d) The reconstructed DFT domain signal clearly identifying the 800 MHz frequency component.

frequency grid, frequency detection will fail [164]. In the application of TD-PCS-OCT, this difficulty leads to only discrete depth profiles and limits its applications in practical scenarios.

More sophisticated reconstruction algorithms based on joint-sparsity-based matching pursuit has been proposed to address this issue [165]. Here, a new optical scheme has been demonstrated based on dual pulse integration that enables the reconstruction of non-harmonic tones using only the basic minimization algorithm. This will allow frequency reconstruction resolution less than the pulse repetition rate and unblock the detection of midpoint frequencies.

In the experiment setup, the optical path length difference is set to be 0.905 mm such that the carrier RF frequency of temporal interference pattern is 725 MHz, which is obviously not a harmonic tone of 50 MHz but a midpoint in the frequency grid with 50 MHz separation.

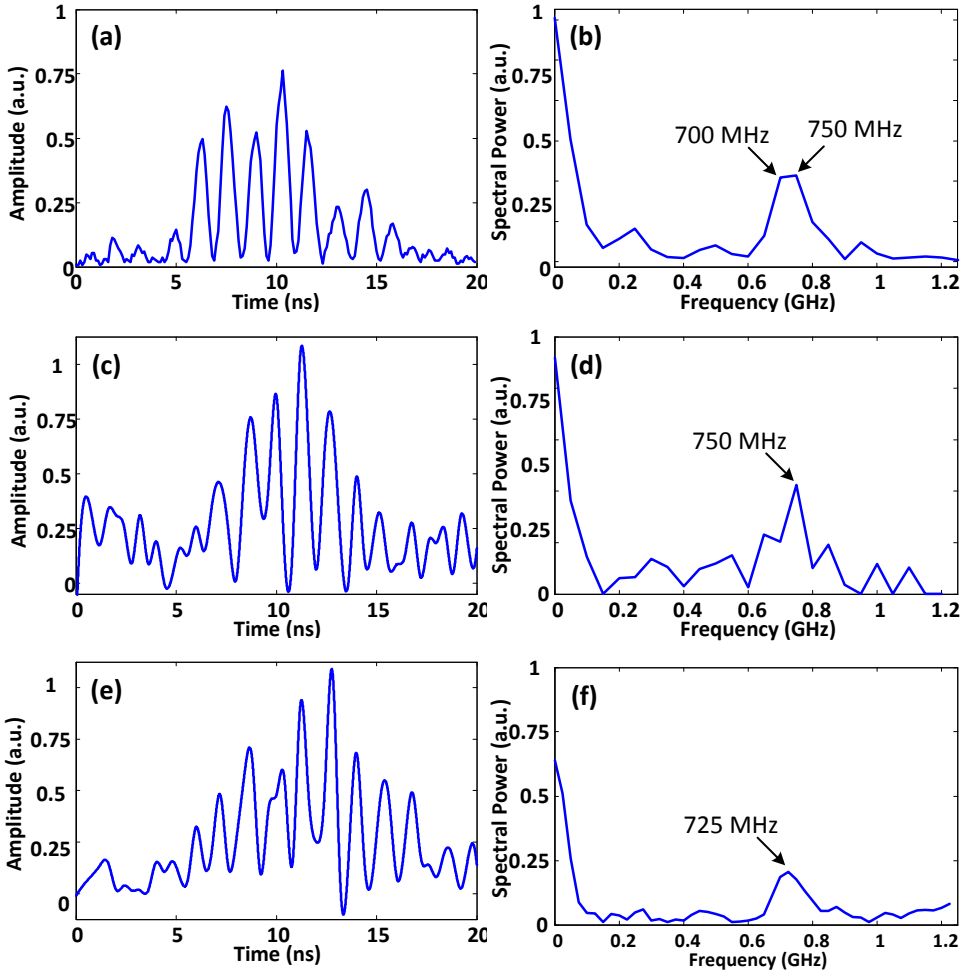

Fig. 3.6 Experimental results showing data compressed PTS-OCT with improved frequency resolution. (a) The original temporal interference waveform with a carrier frequency of 725 MHz. (b) Its Fourier transform shows two closely located frequency peaks at 700 and 750 MHz. (c) The constructed temporal waveform based on normal one pulse integration. (d) Reconstructed DFT signal showing only the 750 MHz signal. This indicates a total failure in frequency identification. (e) and (f) show the reconstruction results based on dual pulse integration. The 725 MHz frequency component is successfully identified.

The original spectrally-encoded temporal waveform is captured using the oscilloscope and shown in Fig. 3.6.a and its Fourier transform is plotted in Fig. 3.6.b. Two closely located frequency peaks at 700 MHz and 750 MHz are presented due to the frequency grid. After normal compressive sensing process, the reconstructed time-domain and DFT-domain signals are shown in Fig. 3.6.c and 3.6.d respectively. The reconstructed frequency shows 750 MHz only and identification of actual 725 MHz frequency has totally failed. This is because 750 MHz component has a slightly higher power than 700 MHz as shown in Fig. 3.6.b and the reconstruction algorithm only can pick up one stronger frequency. Here, two successive PRBS-mixed optical pulses have been integrated to form one measurement element for compressive sensing. As shown in Fig. 3.6.f, the actual carrier frequency of 725 MHz is accurately identified thanks to dual pulse integration, and a compression ratio of 66% is achieved. Note that the detection speed has to be reduced as a trade-off.

3.1.6 RF synchronization

In any system consisting of individual electronic and optical sources, it is essential to synchronize their electronic clocks to reduce any phase fluctuations, distortions in results. In the scope of this thesis, it has been mandatory to synchronize the pattern generator(In our case, Tektronix AWG7122C) with Mode locked laser(calmar Mendocino FP Laser) which emits optical pulses at a repetition rate of 50MHz.

Normally it is custom to use a derived clock from pulsed laser by detecting with a high speed photodetector and isolating a single RF frequncy comb by a narrow bandpass filter. This comb since its a single tone signal, can be used as stable clock for rest of the system such as RF signal generator. The process is depicted in Fig. 3.7.

However, in our case, since the repetition frequency of the mode locked laser is 50MHz, the comb spacing is 50MHz after being detected by Photodetector. To our knowledge, 50MHz narrow bandpass filter that can completely attenuate remaining combs and that has

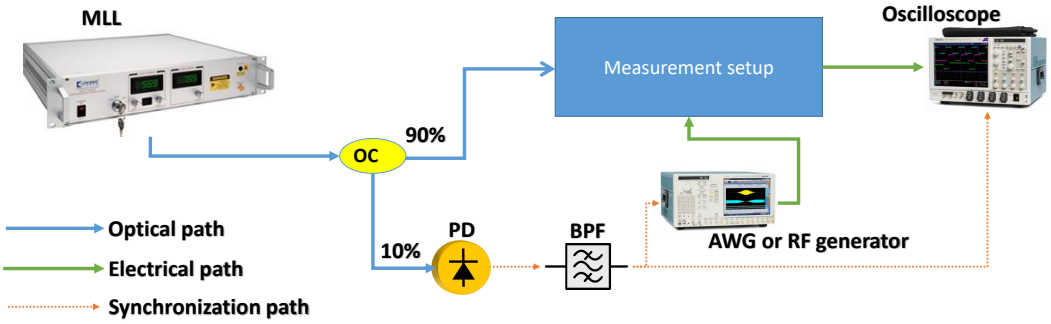

Fig. 3.7 Conventional procedure for RF synchronization

large frequency range has not been available or is too costly. After several attempts, an alternative approach has been considered.

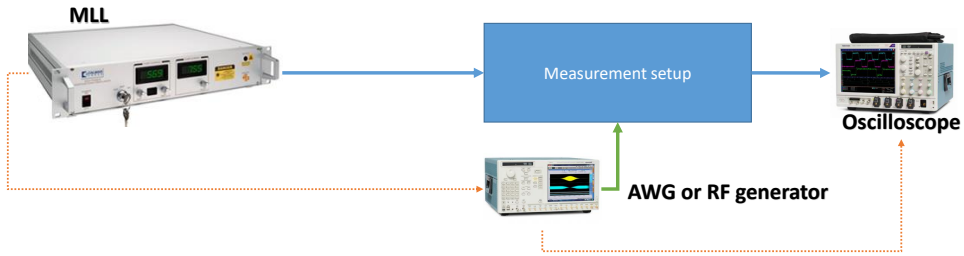

Fig. 3.8 Procedure followed in this thesis for RF synchronization

In all our experiments, Arbitrary waveform generator has been used as the signal source. The MLL has been generating an impulse clock at 50MHz repetition rate. Using this as reference clock with help of co-axial cable, internal clock multiplier factor has been inputted to AWG system software to compute the data rate of the PRBS or any arbitrary signal. For example, to generate 2.5GS/s clock, 50 is given as multiplication factor. The synchronization setup is shown in Fig. 3.8. For faithful reconstruction of the information, the MLL clock should be synchronized with PRBS random pulses. Any offset may result in poor reconstruction.

3.1.7 Evaluation of Minimization Algorithms in Compressive Sensing PTS-OCT

This section 3.1.7 is a collaboration work done with Forensic Imaging Group, School of Physical Sciences, University of Kent

Thus far in this work, a primal-dual interior point method for l_1 minimization has been used for PTS-OCT signal reconstruction. In this section, a number of alternative optimization algorithms for the reconstruction of PTS-OCT signals have been compared in terms of their reconstruction accuracy and efficiency. This will provide useful information in selection of appropriate algorithms for this particular PTS-OCT scheme.

In the context of compressive sensing, the time-stretched measurements can be modelled as a basis pursuit or a lasso l_1 minimization problem. Note that these minimization problems have a slightly different mathematical form to Eq. 2.16. Five sparsity promoting algorithms were compared: primal-dual interior point method (l_1 Magic) [166], alternating direction method for multipliers for basis pursuit (ADMM BP) and lasso (ADMM Lasso) [167], lasso method using coordinate descent (Matlab Lasso) and its standardised version [168], and NESTA [169].

3.1.7.1 Reconstruction accuracy

To make a fair comparison, without loss of generality, the original PTS-OCT signal is set to have four dominant carrier frequencies (2.6 GHz, 2.9 GHz, 3.6 GHz and 4.6 GHz) corresponding to a four-layer sample. A PRBS vector with probability of 0.5 and sampling rate of 10 Gbps is used to mix with the original PTS-OCT signal, which makes the overall signal length to be 200. The reconstructed frequency spectrum is shown, at a common compression ratio of 40% (80 measurements), for each of the five algorithms as shown in Fig. 3.9. The red line is the ground truth signal and blue line represents the reconstructed results. NESTA produces an acceptable result in which the dominant peaks are all reconstructed and

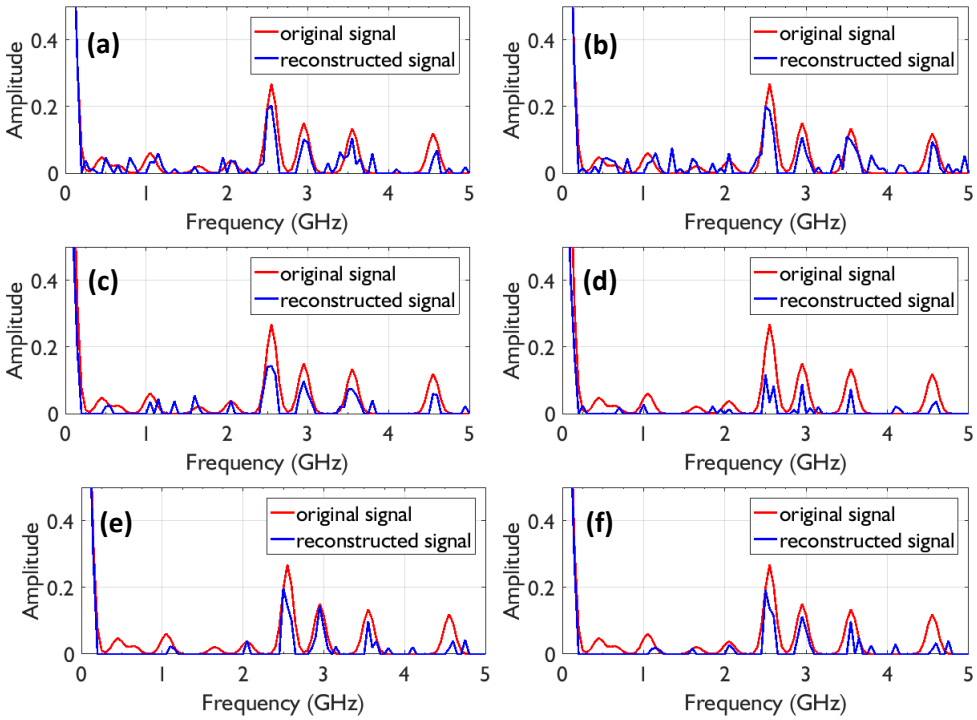

Fig. 3.9 The reconstructed frequency domain signals for all five algorithms corresponding to a compression ratio of 40%. Red line is the ground truth signal and blue line represents reconstruction. From left to right, top row: (a) NESTA and (b) l_1 Magic; middle row: (c) ADMM Basis pursuit and (d) lasso; bottom row: (e) Matlab lasso for non-standardised data and (f) standardised data respectively.

l_1 Magic performs similarly well. ADMM Basis pursuit produces a less noisy signal but the energy at the frequency bands of interest is suppressed, which results in a less accurate result. This is also the case for ADMM lasso. Matlab lasso produces a large frequency drift for the weakest frequency peak at 4.6 GHz.

The reconstruction accuracy was evaluated using the RMSE in the frequency domain. Reconstruction errors were first calculated, over the whole frequency range, for different numbers of measurements ranging from 30 (15% compression ratio) up to a maximum of 200 measurements (no compression) as shown in Fig. 3.10.a. The RMSE for the two ADMM methods is unstable but exhibits a decreasing trend w.r.t. measurements. Conversely, l_1 Magic and NESTA show a smoothly decreasing error w.r.t. measurements and have the

lowest error of the 5 algorithms tested. For the Matlab lasso algorithm, standardization reduces the error for fewer measurements but the error converges with non-standardised result as the number of measurements increases.

Since the four dominant frequency bands indicate the most important information, RMSE was calculated again for four dominant frequency peaks only with the results shown in Fig. 3.10.b. Similar to Fig. 3.11.a, NESTA and l_1 Magic yield the smallest error over the frequency range. The reconstruction error for ADMM basis pursuit is again very unstable w.r.t. the number of measurements. Note at 70 to 90 measurements, ADMM basis pursuit achieves similar results to NESTA. This implies its advantage in reducing noise. In contrast, ADMM lasso remains stable at high sampling densities. Furthermore, standardisation for Matlab lasso has little effect on RMSE.

3.1.7.2 Computation cost

For each algorithm, the processing time for reconstruction was measured 5 times and averaged. The code was run in Matlab on a 64-bit Windows 10 machine with an Intel Core i7 CPU @ 3.07GHz and 8GB RAM. As shown in Fig. 3.11 the processing time for most algorithms is within 1 second except ADMM Basis pursuit which takes longer time than 1.5 seconds, with the peak at 2.4 seconds. This is due to its slow converge speed. ADMM is an iterative algorithm that executes quicker when the number of iterations is reduced at the expense of accuracy. The ADMM lasso is the fastest of the 5 algorithms with relatively small increase in computation time w.r.t. the number of measurements. Note, NESTA takes much more time than l_1 Magic although they have similar RMSE.

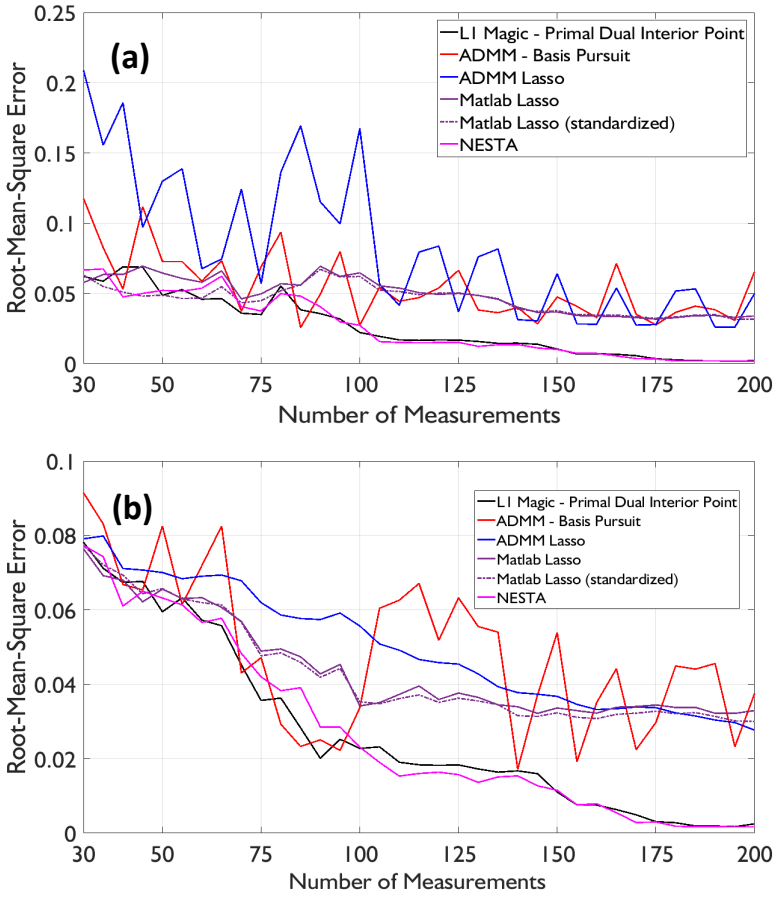

Fig. 3.10 Evaluation of reconstruction accuracy. (a) RMSE of reconstructed signal calculated over entire frequency range. All five candidate algorithms show a descending trend. NESTA and l_1 Magic algorithm yield the smallest RMS error. (b) RMSE of reconstructed signal calculated for the frequencies spanned by the 4 dominant peaks only. Error rates similar for all five algorithms for small number of measurements. Relative performance of NESTA and l_1 Magic improves as the number of measurements increases.

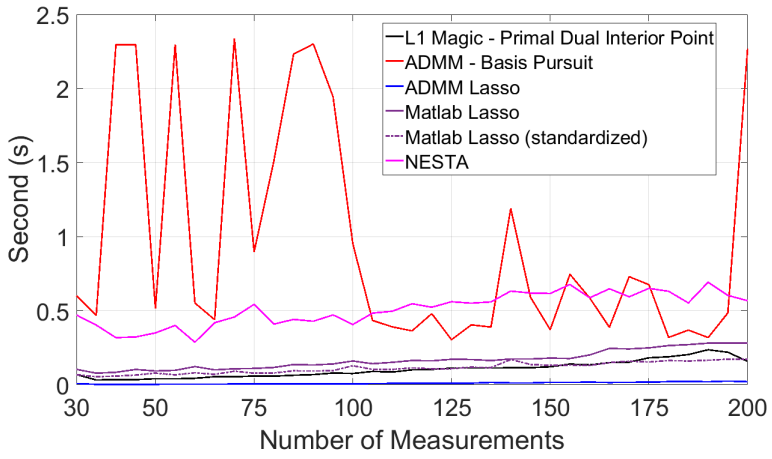

Fig. 3.11 The computational time as a function of the number of measurements. ADMM Lasso, Matlab Lasso, Matlab Lasso (standardized) and l_1 Magic show small linear increase with respect to number of measurements. Basis pursuit is unstable for measurements <110 due to slow convergence rate

3.1.8 Discussions

In our proof-of-the-concept experimental demonstrations presented for TD-PCS-OCT system, 33 measurements were required to reconstruct the original signal with a signal length of 50, leading to a compression ratio of 66%. There is great potential to improve the compression ratio based on the following three principles.

Despite a single carrier RF frequency to be identified for a single-layer sample, the reconstructed DFT domain signal is not a single-tone but a Gaussian frequency distribution with a 3-dB bandwidth of 200 MHz. In signal reconstruction, more calculation resources and hence more measurements are required to reconstruct the whole Gaussian frequency band, which however does not carry any useful information (apart from the central peak frequency) leading to a sacrificed compression ratio. This can be illustrated by simple MATLAB simulation as shown in Fig. 3.12.

Considering a single tone 1 GHz signal at 10 Gb/s sampling rate, the overall signal length is N = 200 as shown in Figure 3.12 in both frequency and time domains in red

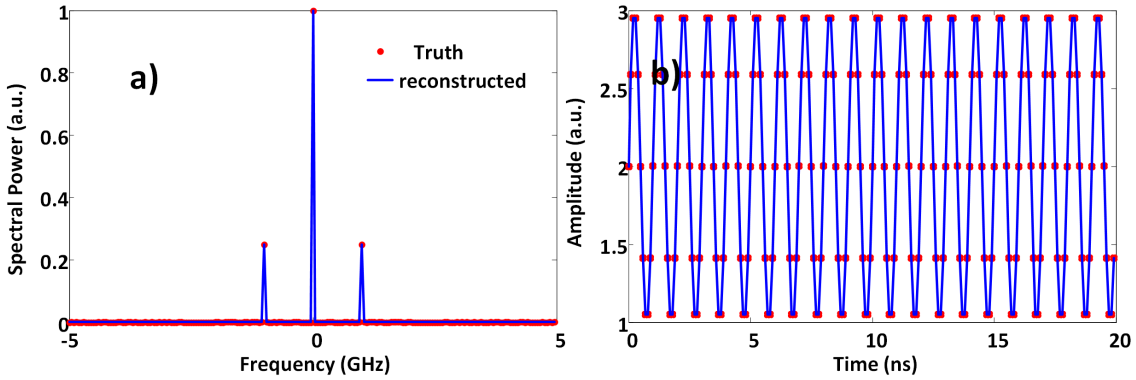

Fig. 3.12 Simulation results of compressive sensing of single tone signal 1GHz with L1 reconstruction algorithm. a) FFT spectrum of the original (red) and the reconstructed (blue) signals; b) Time domain of original(red) and reconstructed(blue) signal

dots. A set of binary random sequences have been mixed and integrated with the signal. Using L1 reconstruction, the reconstructed signal in FFT and time domains are shown in Figure 3.12 in blue color. As observed, the bandwidth occupied by the single tone is 50MHz and the number of non-zero tones are 3 and the number of measurements are as low as 10 making the compression ratio 5% whereas the OCT signals in the experiments and simulations in previous sections were convolutions of tones with time stretched MLL Gaussian pulses, which results in semi sparse signal with more non zero frequency tones, 27 in single layer experimental results which need to be retrieved. This concept is similar to axial scan resolution limit in SS-OCT system. Figure 3.4 shows the single tone signal convoluted with time stretched MLL Gaussian pulses. As the number of measurements required linearly dependent on sparse tones, the number of measurements required are higher in this case. This issue can be improved by stretching the optical pulse further to a longer time window. Then the Fourier domain bandwidth will be effectively reduced. With a full-stretch of 100% duty cycle, the Fourier domain bandwidth for each carrier frequency can be as low as the pulse repetition rate [170], which is 50 MHz in our case. The compression ratio can be improved by 4 times.

Secondly, the compression ratio can be significantly improved by increasing the PRBS rate. In our demonstration, PRBS patterns are sampled at 2.5 Gbps, which is purely limited by the bandwidth of our AWG equipment. Low Nyquist rate not only limits the compression ratio but also the detection bandwidth of the PTS-OCT system. High data rate PRBS generator is a real challenge due to the electronic bottleneck. One solution is to partially compress over-stretched and PRBS-modulated optical pulse to increase the effective PRBS sampling rate [165].

Thirdly, the problem of Gaussian frequency band in the reconstructed DFT domain signal can be tackled from a different perspective. Here, PRBS-modulated Gaussian pulse has been used as an analog random bit sequence, rather than binary PRBS patterns as used in traditional compressive sensing systems. The use of Gaussian-shape analog random bit sequence in the reconstruction algorithm will effectively remove the Gaussian envelope of the information-carrying optical pulse and hence reduce the bandwidth of carrier frequencies in DFT domain. This method can be implemented purely in the digital domain during signal reconstruction and no hardware changes, such as pulse over-stretching and partially compression, are required. More simulations are carried out to verify this approach with parameters as same as used in previous sections. As shown in Fig. 3.13, the bandwidth of frequencies of interest (3.5 and 4 GHz) has been greatly reduced due to the removal of Gaussian envelope (see inset of Fig. 3.13). Only 20 measurements are required to reconstruct the signal shown in Fig. 3.13, leading to a greatly improved compression ratio of 10%. The method has been improvised to spectral filter with cascaded MZI structure to eliminate the electronics mostly. The method has been presented in next section.

3.1.9 Conclusion

In this section, a data compression approach has been proposed and experimentally demonstrated based on for OCT systems. Random mixing and integration processes were imple-

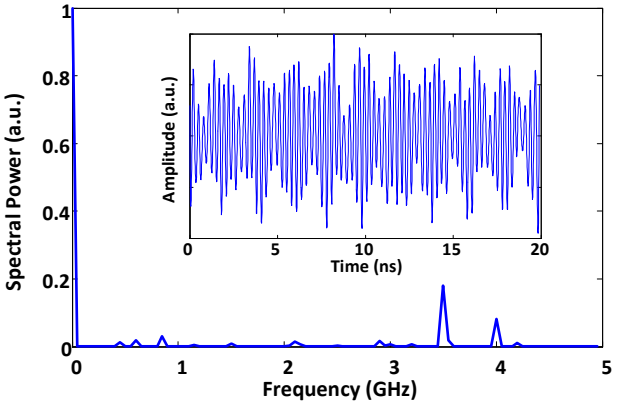

Fig. 3.13 Simulation result showing improvement of compression ratio using a Gaussian-shaped analog random bit sequence. The bandwidth of frequency peaks have been reduced. The inset shows the reconstructed temporal waveform, clearly indicating the removal of Gaussian envelope.

mented in the optical domain directly free from the electronic bottleneck. High-throughput axial scanning at 1.51 MHz has been achieved using low-speed data acquisition at 50 MS/s due to photonic compressive sensing with a compression ratio of 66%. A new dual pulse integration approach has been proposed and experimentally demonstrated to improve the frequency resolution of the system. Though simulation, a Gaussian-shape analog random bit sequence was used in the reconstruction algorithm, which leads to an improved compression ratio of 10%. In addition, a number of optimization algorithms for the reconstruction of the PTS-OCT signals have been studied in terms of reconstruction accuracy and efficiency.

3.2 Spectral Domain Photonic Compressed Sensing for blind spectrum sensing

As explained in chapter 2 and in previous section, the main limitation in TD-PCS system is the requirement of high-speed random sequence and high speed electro optic mixing. In this section,a novel approach of Spectral Domain Photonic Compressed Sensing (SD-

PCS) system has been demonstrated. In the following subsections, principle of generating random patterns in optical domain has been presented followed by the application in blind RF spectrum sensing. The method has been extended to Linearly Chirped Fibre Bragg Grating based strain sensing.

In this section, novel approach of SD-PCS method based on cascaded MZI has been demonstrated for detection of single-tone and two-tone RF signals with <25% compression ratio using only 50 MHz detection bandwidth. In contrast to other methods, analog random patterns have been generated using a spectral filter based on wavelength to time mapping in time stretched optical pulses [65]. The spectral filter using two cascaded dispersion unbalanced Mach-Zehnder Interferometers (MZIs) provides random spectral response. This spectral response changes with change in optical delay of one of MZI structure. Since, no high speed PRBS required in this approach, electronic bottleneck is overcome in random mixing. While in previous section, 66% compression ratio has been reported, which is due to convolution of encoded information with electrical spectrum of time stretched Gaussian optical pulse. This method reduces the compression ratio significantly to less than 20% as the Gaussian analog random sequence is used as a random pattern to retrieve the encoded information.

The remainder of this section 3.2 is organized as follows. In section 3.2.1, the principle and methods of the proposed system have been explained in detail. Section 3.2.2 is presented with simulation results to verify proposed system followed by experimental results in section 3.2.3. Discussions on improvements are provided in section 3.2.4. The work is summarized and concluded in section 3.2.5 .

Remainder of this section 3.1 is an extended or modified versions of published conference paper [66].

3.2.1 Principles

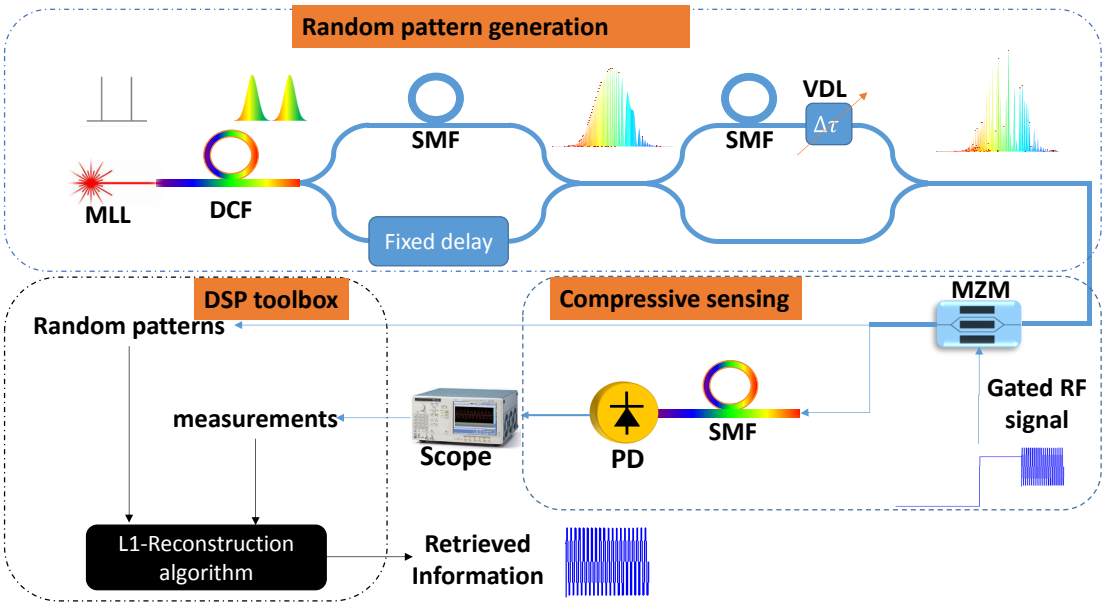

Fig. 3.14 Schematic for SD-PCS experimental setup based on cascaded MZI structure with variable optical delay element

Schematic diagram of our proposed SD-PCS system based on cascaded MZI structure is shown in Fig. 3.14. The overall principle has been explained in subsections as Random pattern generation, Photonic Compressed sensing process.

3.2.1.1 Random pattern generation

The optical source is a passive mode locked laser (MLL) that produces a series of broadband ultrashort pulses. Each optical pulse is time stretched by Dispersion Compensating Fibre(DCF) to map the temporal domain to Fourier domain and are processed with Cascaded MZI structure as shown in Fig. 3.14. MZI-1 response shows the chirped response with central frequency dependent on optical delay. The spectral response can be modelled as,

$$H_1(\omega) = \frac{1}{2}\left[1 + e^{-j\omega\Delta t_1 + j\frac{\phi\omega^2}{2}}\right] \tag{3.8}$$

where Δt_1 is the fixed time delay between two arms, and denotes the dispersion unbalance controlling chirp rate and FSR of MZI filter respectively. The chirped response is processed with MZI-2 with opposite chirp rate to produce a cascaded response. The convolution of MZI-2 impulse responses produces a pseudo random pattern which can be changeable with varying the delay of one of the MZIs. The cascaded spectral response of MZIs can be modelled as,

$$\left|H(\omega)\right| = \left[cos\left[\frac{\phi\omega^2}{2} + \frac{\omega(\Delta t_2 - \Delta t_1)}{2}\right] + cos\left[\frac{\omega(\Delta t_2 + \Delta t_1)}{2}\right]\right] \tag{3.9}$$

where Δt_2 is the variable time delay between two arms in the second MZI. It is crucial that these patterns should be distinct for successful reconstruction. This distinctiveness can be modelled by calculating cross correlation between any 2 patterns.

3.2.1.2 Photonic Compressed Sensing

Unlike the conventional systems where the random sequence is either generated by electronic AWG or SLM/DMD, in this case, the random patterns are generated in optical domain. Hence, compressed sensing process can be subdivided into 3 steps. 1) Calibration phase: The patterns are measured with high speed detector and high speed oscilloscope one time and are stored in computer against the variable delay values. 2) Sensing phase: Utilizing all-optical mixing and integration methods, the integrated power measurements are taken at 50MS/s rate which is the repetition rate of MLL. 3) Post-processing phase: Utilizing Digital Signal Processing tools, the information is reconstructed.

1.Calibration phase:

The patterns are directly measured using high speed photodetector and oscilloscope. Although the pattern is acquired with sampling rate of oscilloscope with length N, the over all nyquist rate of the system is based on minimum spectral power received by photodetector and maximum sampling rate of the oscilloscope. Hence the bandwidth of the overall measurement

system can be estimated as,

$$f_{max} = min\left(\frac{\text{maximum Sampling rate of oscilloscope}}{2}, f_{max}\text{by photodetector}\right) \tag{3.10}$$

Hence, the sampled random patterns are sufficiently integrated so that the over all length of the signal that can be determined as,

$$N = \frac{2 \times f_{max}}{\text{MLL repetition rate}} \tag{3.11}$$

2.Sensing phase:

Once the spectral range is determined, the unknown RF signal, $x_{N\times 1}$ which is assumed to be sparse in DFT domain $\psi_{N\times N}$, the sparse representation of x can be written as, $s = \psi x$. When the RF signal mixed with m random patterns $\phi_{m\times N}$ generated from cascaded MZI structure by varying the optical delay in MZI-2 with M different values, the integration produces M compressed measurements, $y_{M\times 1}$.

3.Post-processing phase:

By inputting the measurement vector $y_{m\times 1}$ and stored random patterns with effective length N estimated as per 3.11 and solving the l_1 minimization equation explained in section 2.2, the unknown RF signal can be reconstructed in Fourier domain and temporal domain. During this entire process the RF signal generator and oscilloscope are synchronized to MLL to lock the optical carrier with RF signal. The static delay in MZI arm is compensated by adding additional fibre in other arm.

3.2.2 Simulation Results

In this section, simulation results have been presented using VPItransmission maker software. As shown in Fig 3.14, MLL generates broadband ultra-short optical pulse train with 50MHz

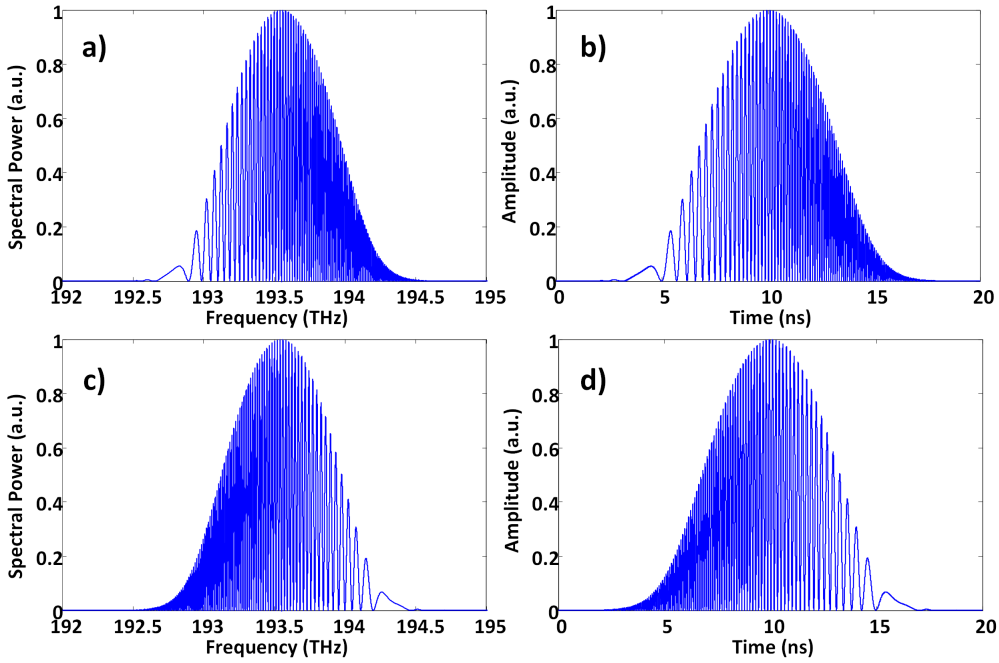

Fig. 3.15 Temporal and spectral domain responses of cascaded dispersion-unbalanced MZIs. (a) Spectral domain output and (b) time domain response of the first MZI with a fixed time delay of 50ps; (c) individual spectral domain and (d) time domain response of the second MZI alone with delay of 50ps

repetition rate with FWHM of 800fs. The optical pulses are time stretched using 960 ps/nm DCF.

The first MZI has fixed optical delay line in one arm and 500m Single mode Fibre in another arm. This produces a chirped response as shown in Fig.3.15. Fig. 3.15.a shows spectral response and corresponding time domain response is shown in Fig. 3.15.b. The chirp rate is controlled by Single Mode Fibre (SMF) dispersion and the central frequency is controlled by fixed optical delay in MZI-1 as per Eq. 3.8. The cascaded MZI responses are shown in Fig.3.16. Fig. 3.16.a shows temporal response of cascaded MZI when the optical delay of second MZI is set to 17.5 ps. The corresponding FFT domain is shown in Fig. 3.16.b. For another delay value of 21.25ps, the temporal and FFT domain responses are shown in Fig 3.16.c and 3.16.d. The nyquist rate of the patterns can be determined by observing the RF spectrum of the cascaded MZI responses in Fig. 3.16.b and 3.16.d. The power drops

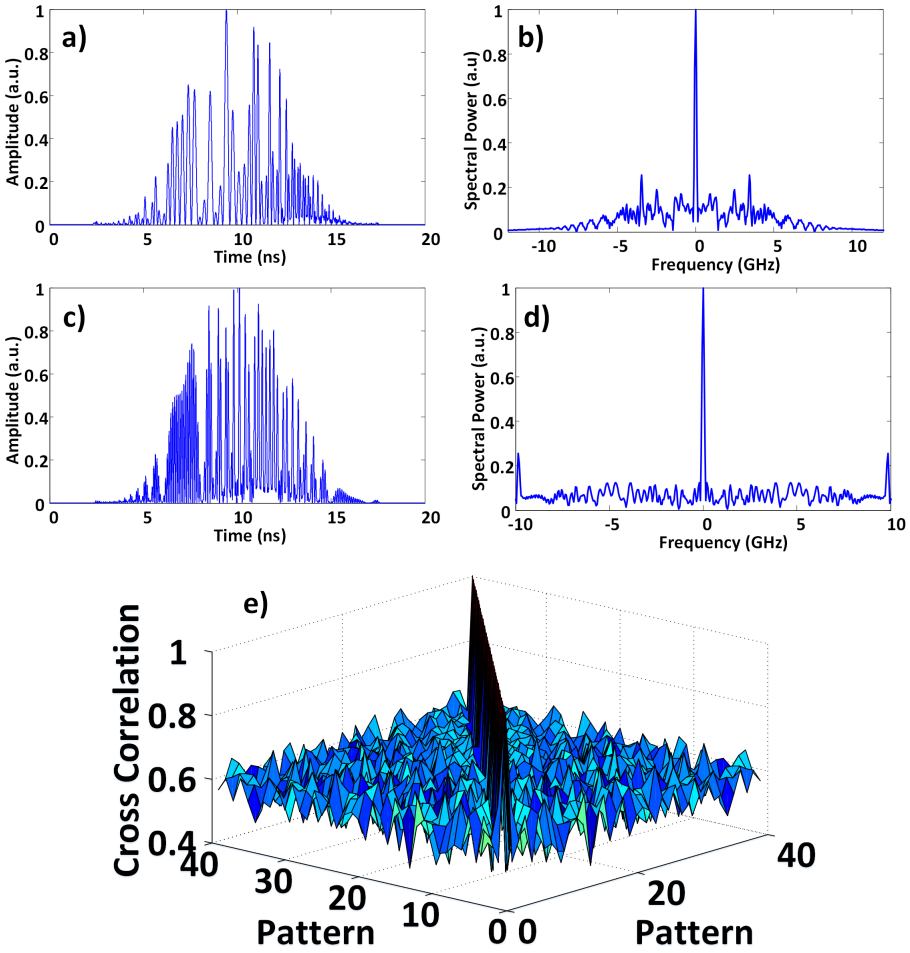

Fig. 3.16 Quasi random patterns from cascading effect. a) Temporal domain representation of Random pattern when variable delay is 17.5ps b) Corresponding FFT spectrum c) Temporal domain representation of Random pattern when variable delay is 21.25ps d) Corresponding FFT spectrum e) Correlation of the random patterns generated by varying the delay in second MZI from 1.25ps to 50ps in steps of 1.25ps

significantly after 10GHz. hence, can be considered as maximum frequency detectable by the system. One of measure of distinctiveness between the patterns is cross correlation between the patterns. The cross correlation is measured between the patterns and are presented in Fig. 3.16.e. The maximum cross correlation between any two different patterns is 70.41% with average cross correlation between any two different patterns is 45.76% after removing the highly correlated tail part which is low in amplitude.

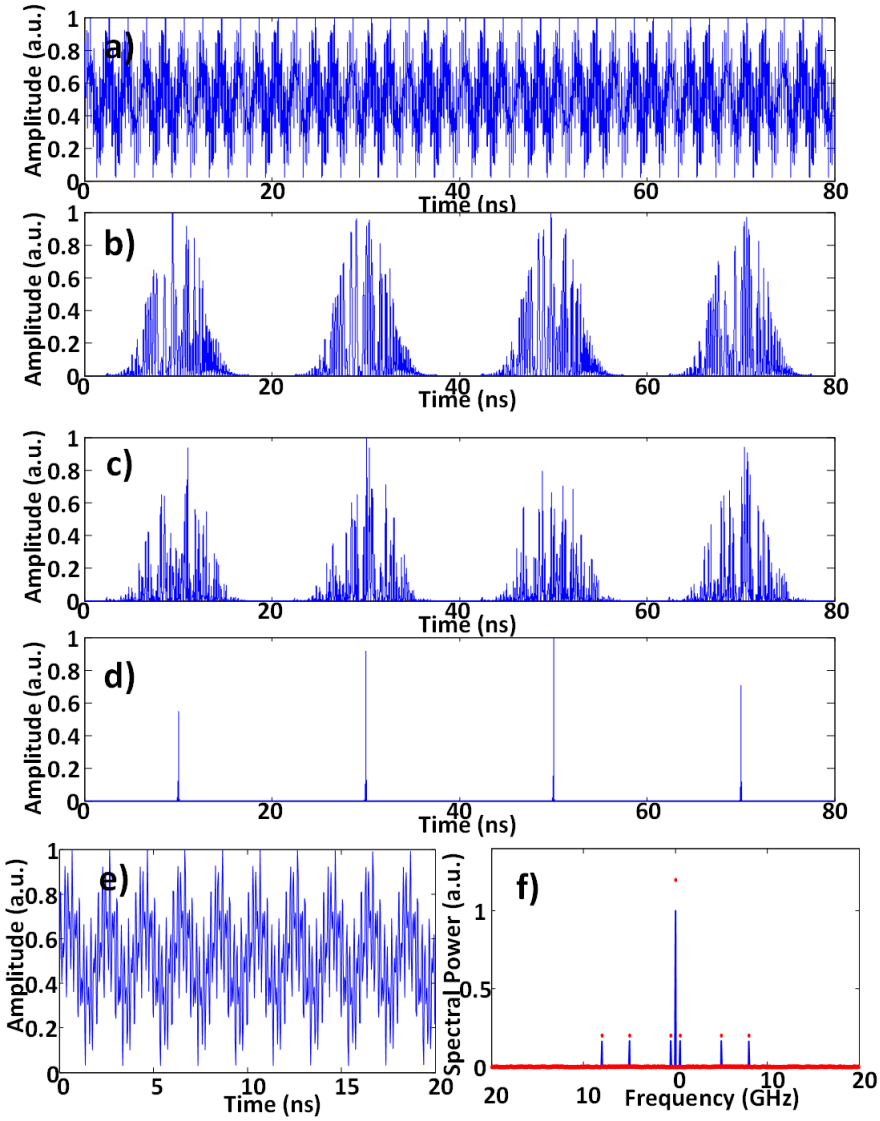

Fig. 3.17 Simulation results for 3 tone signal. a) a 3-tone RF signal input repetitive of 20 ns b) Gaussian random patterns with time delay varying from 1.25ps to 5ps c) Corresponding mixed signals d) Summed measurements of varying amplitude levels representing the dot product of random pattern with RF signal d) Output after electro optical mixing with RF signal e) Reconstructed output in time domain after l_1 reconstruction f) Reconstructed signal in Fourier domain showing successful reconstruction of all 3 tones blue representing reconstructed signal with red color representing original signal's FFT representation.

Each random pattern generated is electro optically mixed with a test 3-tone RF signal shown in Fig. 3.17.a. The Corresponding FFT domain representation is shown in Fig. 3.17.f in red color. Time domain random patterns with cascaded MZI response are shown in Fig. 3.17.b. First four patterns are shown with optical delay in second MZI varying from 1.25ps to 5ps. The mixed patterns are shown in Fig. 3.17.c. Corresponding integrated measurements are shown in Fig. 3.17.d. each representing the dot product of unknown RF signal with Gaussian random pattern. The random pattern is down sampled to N=800 as per maximum frequency condition represented in Eq. 3.10 for faithful reconstruction and for inputting to l_1 minimization program. After generating the random patterns with 40 different delay values, integration and reconstruction process, the reconstructed signal temporal domain representation is shown in Fig. 3.17.e and corresponding FFT domain representation is shown in Fig. 3.17.f in blue color with original FFT is shown in red color. A good match has been obtained between the original signal and reconstructed signal. The compression ratio in this case was 5%.

3.2.3 Experimental Results

To verify the utility of proposed SD-PCS system, a proof of concept experiment has been implemented as shown in Fig. 3.14. In the experiment, a passively mode locked laser (Calmar Mendocino FP laser) has been used as optical carrier which generates a series of ultrashort broadband optical pulses with 50MHz repetition and FWHM of 800fs. Following time stretch of -1.04ns/nm with DCF(OFS SMFDK-S-020-03-01), the optical pulses are processed with cascaded MZI structure with variable time delay to generate random patterns. The MZI-1 has fixed optical delay (VDL-001) in one arm and 50m fibre in another arm. The response of MZI-1 with time stretched optical pulse is shown in Fig. 3.18.a. MZI-2 has 500m SMF and variable optical delay (VDL-002) in one arm and few meter SMF in another to compensate for any static delay. The individual response of MZI-2 with optical delay 230ps, 330ps are

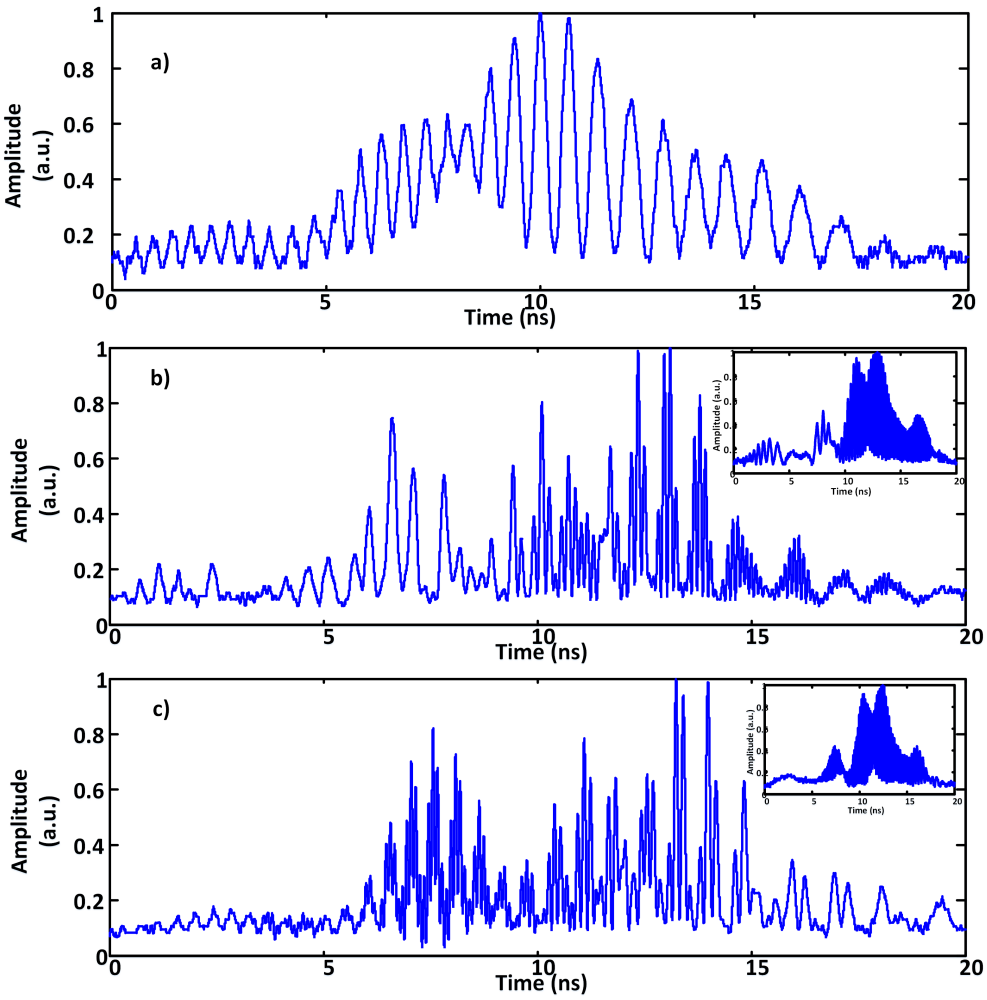

Fig. 3.18 Experimentally generated optical random patterns. a) Random pattern of MZI-1 b) c) Cascaded MZI response with 230ps as variable optical delay in MZI-2 set to 230ps e) Cascaded MZI response with 330ps as variable optical delay in MZI-2 set to 330ps.

shown in Fig. 3.18.b and 3.18.c in inset. The cascaded response of both MZIs are shown in Fig. 3.18.b and 3.18.c. The corresponding RF spectra of the cascaded response is shown in Fig. 3.22.a and 3.22.b. on a log scale.

As discussed in previous section, the distinctiveness between the random patterns can be best described by calculating the cross correlation between random patterns. The cross correlation for experimentally generated random patterns are shown in Fig. 3.19. The maximum cross correlation was 76% which is in good agreement with simulated random

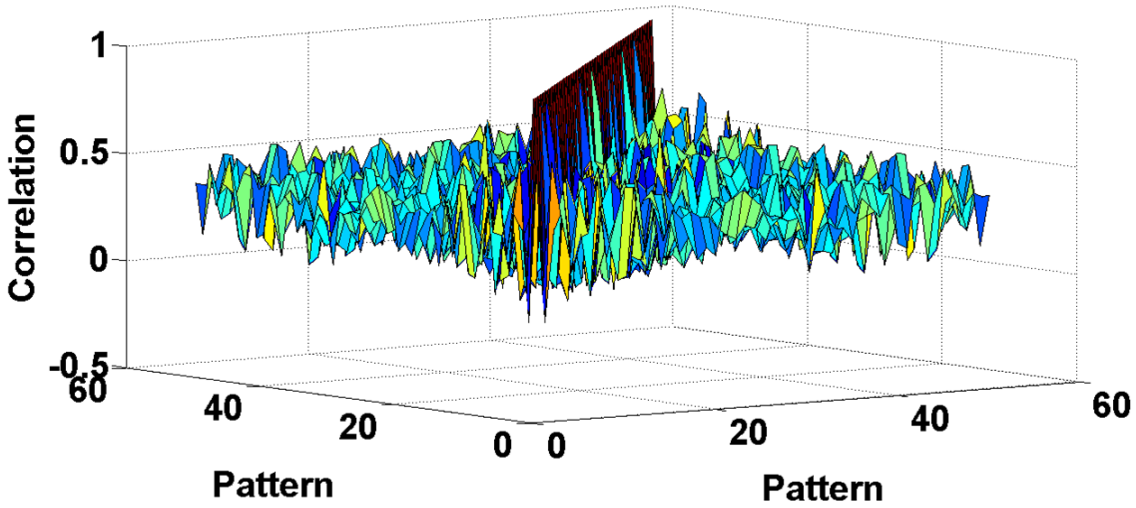

Fig. 3.19 Correlation of the random patterns generated by varying the delay in second MZI from 230ps to 330ps in steps of 2ps.

patterns. The cross correlation can be reduced further if the optical delay step is increased which in this case is 2ps.

The experimentally generated random patterns are used for compressed sensing approach and the results are presented in Fig.3.20. The input two tone RF signal is shown in Fig. 3.20.a. and corresponding FFT domain representation is shown in Fig. 3.20.b showing peaks at 0.4GHz and 1GHz. The FFT representation of reconstructed signal is shown in Fig. 3.20.d and time domain representation is shown in Fig. 3.20.c blue color. The smoothened version of the signal is shown in red color showing a good match with original signal shown in Fig. 3.20.a. With similar procedure, the single tones 0.5GHz and 1GHz were also reconstructed successfully and are shown in Fig. 3.21.

3.2.4 Discussions

The proposed system has significant advantage over conventional TD-PCS system by means of all-optical generation, mixing and integration of random patterns with temporally encoded information. However, finding the nyquist rate of the system is crucial to determine the

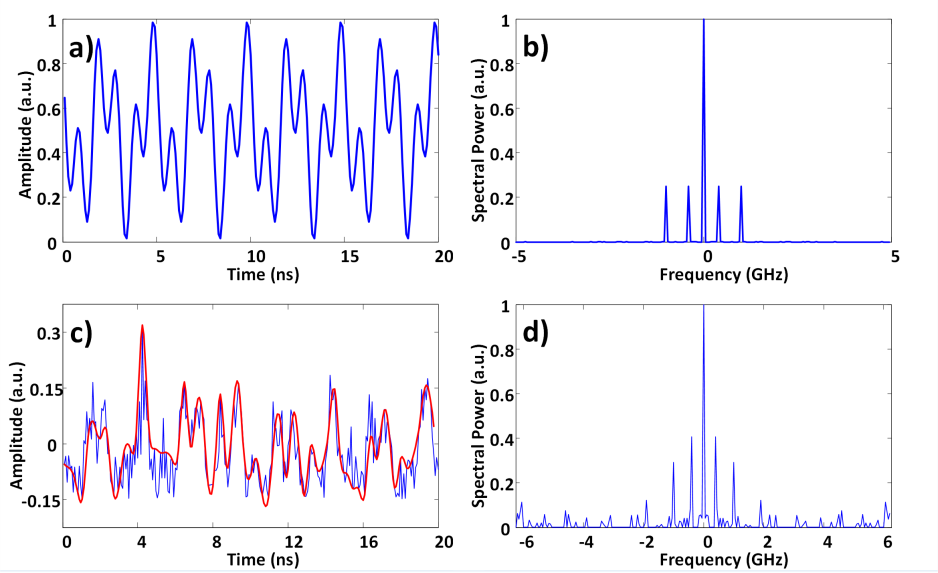

Fig. 3.20 Experimental results with two-tone RF spectrum a) Input test RF signal time domain b) Corresponding FFT representation c) Reconstructed RF signal in time domain shown in blue color. The smoothed version is shown in red color for comparison with original RF signal d) Corresponding FFT representation showing two strong peaks at 0.4GHz and 1GHz.

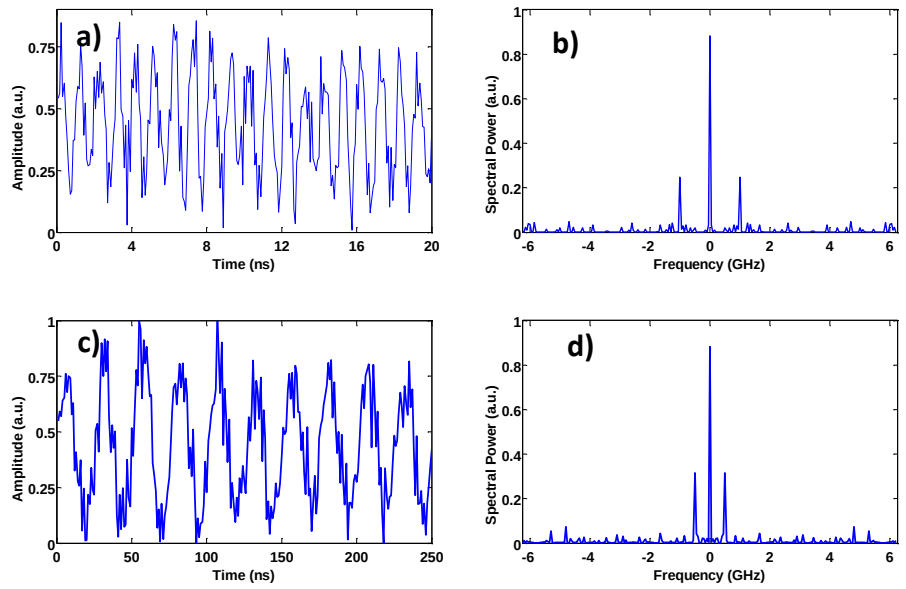

Fig. 3.21 Experimental results with single tone RF spectrum a) Reconstructed 1GHz tone in time domain b) Corresponding FFT representation c) Reconstructed 0.5GHz tone in time domain d) Corresponding FFT representation.

capability. In this section, one of the approach to determine the maximum RF frequency that can be captured by the system has been discussed. FFT of the random patterns on log scale has been shown in Fig. 3.22 for four different optical delay values. As it can be observed the FFT domain has spectral power variation for different frequencies and for different optical delay values, the spectral power varies for a specific frequency. It can be observed that the RF spectral power significantly drops after 10GHz implying that the remaining frequency components' presence is negligible in the pattern.

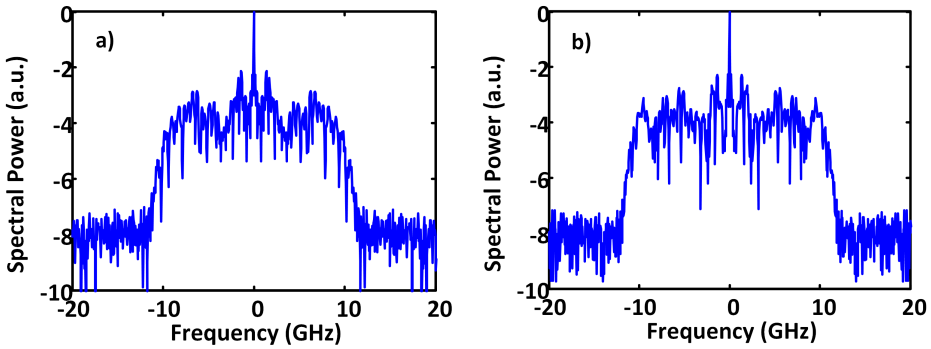

Fig. 3.22 FFT representations of the random patterns shown in Fig. 3.18 .a) FFT of the cascaded MZI structure when optical delay in MZI-2 set to 230ps. b) FFT of the cascaded MZI structure when optical delay in MZI-2 set to 330ps.

The maximum capturing frequency can be extended to tens of GHz by changing the length of SMF and adjusting the optical delay values. Few more simulation results have been presented explaining this proposal.

The proposed schematic is shown in Fig. 3.14. The SMF length in MZI-1 is 5km and optical delay is adjusted to be 50ps. SMF length in MZI-2 is 5km and optical delay is varied from 0 to 100ps in steps of 2ps. The cross correlation between the 51 patterns is shown in Fig. 3.23.a. The maximum cross correlation is calculated to be 67.48%. A 3 tone RF signal 5GHz, 8GHz and 60GHz has been applied as input and has been successfully reconstructed with 0.6% compression ratio. The Nyquist frequency limit in this case is 100GHz assuming that the random patterns are calibrated with high speed photo-detectors.

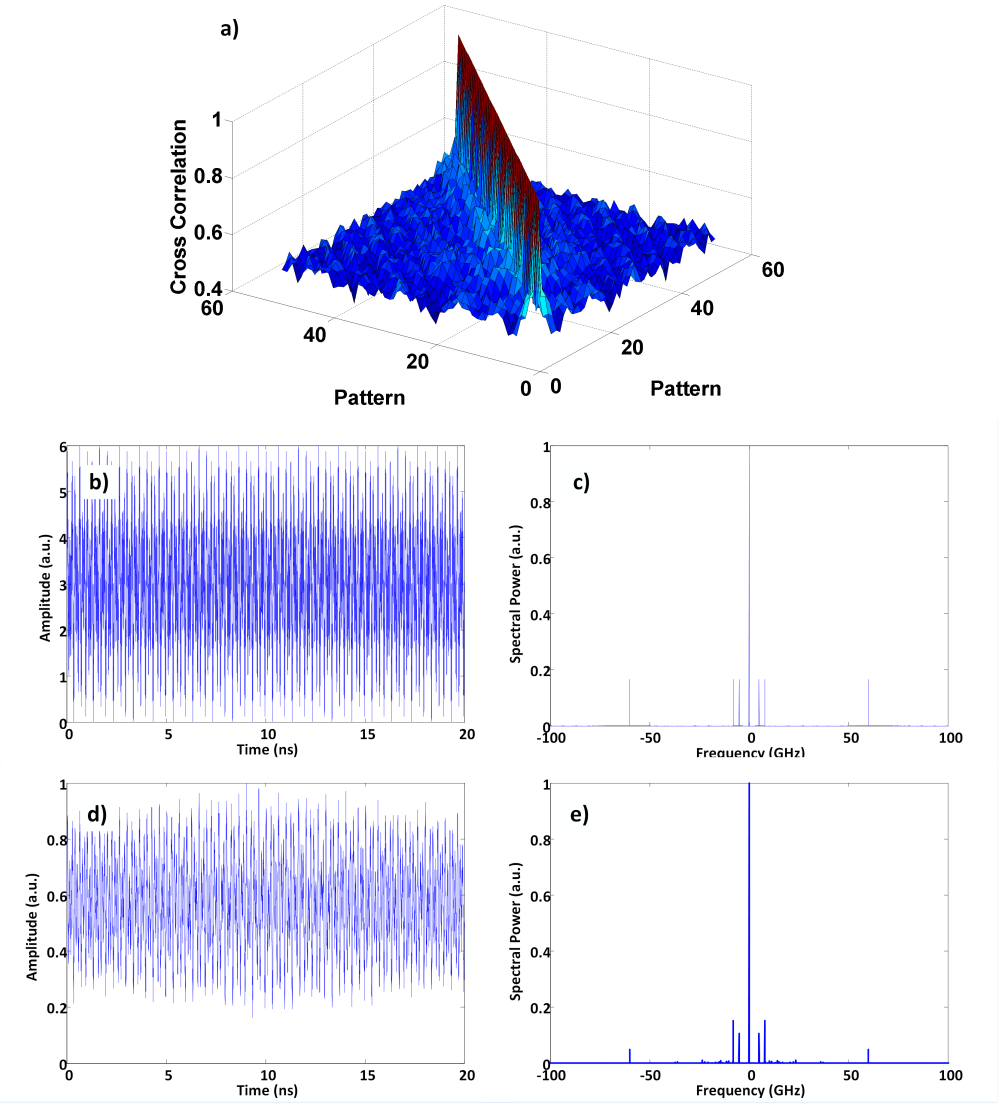

Fig. 3.23 Simulation results for verifying the bandwidth of the proposed setup using VPI-transmission maker software. a) Cross correlation between the random patterns b) Test RF signal in time domain c) Corresponding frequency domain showing RF frequencies 5GHz, 8GHz and 60GHz. d) Reconstructed RF signal from mixing and integration and l_1 reconstruction e) Reconstructed RF signal in FFT domain showing strong spectral powers at exact locations as input RF signal.

As observed in Fig. 3.23.b and 3.23.d, the spectral powers of original and reconstructed tones slightly differ as the reconstruction is due to spectral mixing and reconstructed spectral power is governed by the spectral powers of random patterns used in the system. The photonic compressed sensing system requires predictable random patterns i.e., the random patterns used for reconstruction and used in mixing should be identical. The optical phase and poilatization sensitivity will distort the random patterns and these effects need to be mitigated by either stabilizing the Mach-Zehnder interferometric setup or monolithic integration through Photonic Integrated Circuits.

3.2.5 Conclusions

A novel approach of SD-PCS system based on cascaded MZI structure has been demonstrated for RF signal detection. The technique has potential to sense higher frequency tones of few GHz and the compression ratio can be as low as 20%. The Nyquist frequency of the system can be increased further by changing the length of SMF in the MZI arms. Though bandwidth is ultimately limited by Mach-Zehnder modulator for blind spectrum sensing, this approach can find potential applications in imaging and optical coherence tomography such biomedical applications where spatial or spectral domain encoding takes place. However, one time calibration is needed for storing the random patterns during calibration phase using high speed digitizer before taking actual measurements.

3.3 High throughput compressed FBG sensing

High-throughput fully distributed fiber Bragg grating (FBG) sensors based on optical time-stretch frequency-domain reflectometry (OTS-FDR) [171, 28] has proved to be a promising tool for high temporal and spatial resolution distributed strain sensing. The dynamic distributed strain information along the FBG sensor can be reconstructed from the instantaneous

RF frequency of the captured temporal interference waveform. An unprecedented measurement speed of 50 MHz with high spatial resolution of 31.5 μm and strain resolution of 9.1 $\mu\varepsilon$ have been demonstrated per 25 mm gauge length. This approach has been successfully applied to high-speed strain and pressure sensing in dynamic extremes of magnetic materials [172]. However its capability is essentially limited by the sampling rate and bandwidth of back-end electronic digitizer. More importantly, this real-time FBG sensor interrogation system continuously generates huge volume of data at high data rate, which challenges current electronic circuitry, data storage device, and digital signal processing units. The electronic bottleneck and big-data challenge in high-throughput FBG sensor interrogation systems can be addressed with the help of photonic compressed sensing techniques addressed in previous sections of TD-PCS and SD-PCS systems.

In this section with numerical simulations, the first application of photonic compressive sensing technique in a data-efficient interrogation system has been proposed for high-throughput distributed FBG sensors, which reduces the bandwidth requirement for photodetectors and digitizers and compresses the overall data size using TD-PCS system. TD-PCS system for FBG sensing has been abbreviated as TD-PCS-FBG system. Followed by this, SD-PCS system based on cascaded MZI has been simulated as traditional TD-PCS system requires expensive binary PRBS mixing. With 60% compression ratio, the strain profile has been reconstructed with TD-PCS-FBG and SD-PCS-FBG systems. The following sections are purely simulation based approaches modelled in MATLAB.

The schematic of the proposed system is shown in Fig.3.24. The OTS-FBG module includes a pulsed laser, a reference FBG and a sensing FBG, and a dispersive fiber [171]. Due to the non-uniform strain applied to the FBG sensor, a chirped temporal interference waveform within a short interval of 20 ns was generated. Each chirped waveform carrying strain information is mixed with a set of PRBS in digital domain at a bit rate of 20 Gbps, and fully compressed to form one element of the outputting measurements. The measurements

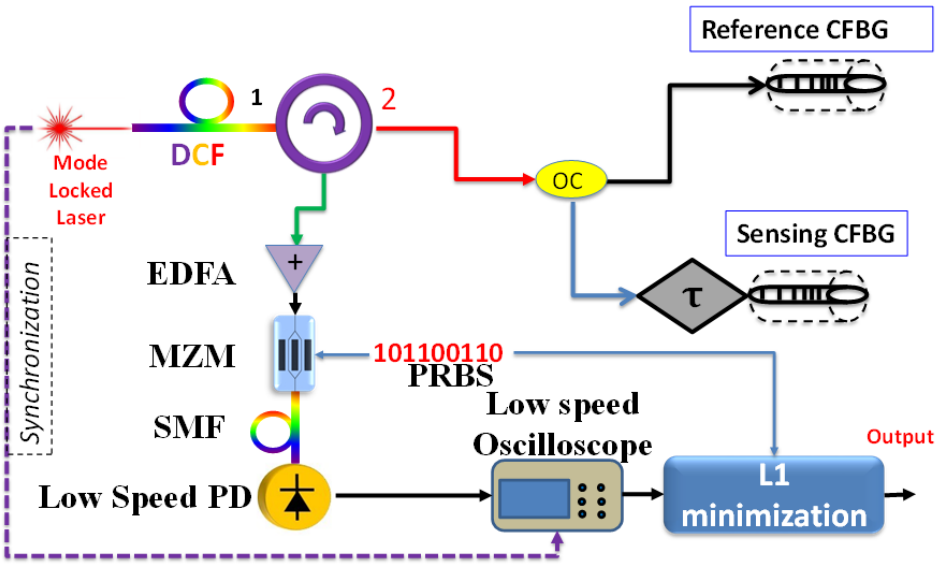

Fig. 3.24 Schematic of proposed and simulated TD-PCS-FBG system with traditional binary PRBS based random mixing.

can be down-sampled at 50MHz, which not only reduces the bandwidth requirement for the photodetector and digitizer, but also compresses the overall data size. With the knowledge of PRBS sequence and the measurements, the original chirped signal can be reconstructed from compressed data set using l_1 minimization. All useful frequency information, which represents the distributed non-uniform strain with a discrete jump, has been successfully recovered with 60% compression. As the number of measurements increases, the reconstructed signal asymptotes towards actual information signal.

3.3.1 Results with Time Domain Photonic Compressed Sensing

In this section, the results obtained with TD-PCS system have been presented for monotonic FBG strain profile and S-shaped strain profile.

3.3.1.1 Monotonic profile

As shown in Fig. 3.24, a passive mode locked laser is used to generate an optical pulse train with 20ns repetition rate with 800fs pulse width. The pulses are directed via 60km DCF

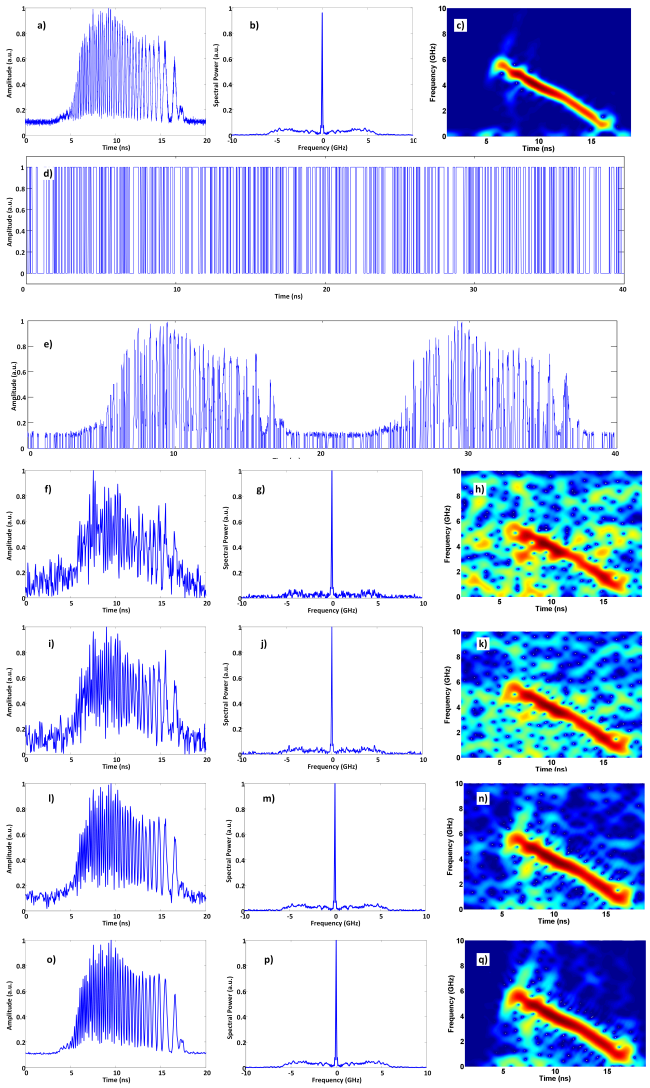

Fig. 3.25 Simulation results for TD-PCS-FBG system with monotonic strain profile. a. Original time stretched sensing signal in time domain b. FFT respresentation of the time domain signal c. Spectrogram of the sensing signal showing linear frequency chirp d. Two PRBS sequences used for mixing e. Mixed signal with PRBS and sensing signal. f. Time domain reconstruction of sensing signal upon l_1 reconstruction with 62.5% compression ratio g. Corresponding FFT domain representation h. Spectrogram showing clear chirp profile. The l_1 reconstruction results are repeated for 75 % ,87.5% and 100 % compression ratios and the time domain reconstruction is shown in Fig. i. l. and o. , corresponding FFT domain representation in Fig. j. m. and p. , and corresponding chirp profiles are shown in Fig. k. n. and q.

(Group Velocity Dispersion of -1.044ns/nm) resulting in a stretched optical pulse of around 12ns. The time stretched signal is processed through OTS-FBG interrogation setup and in

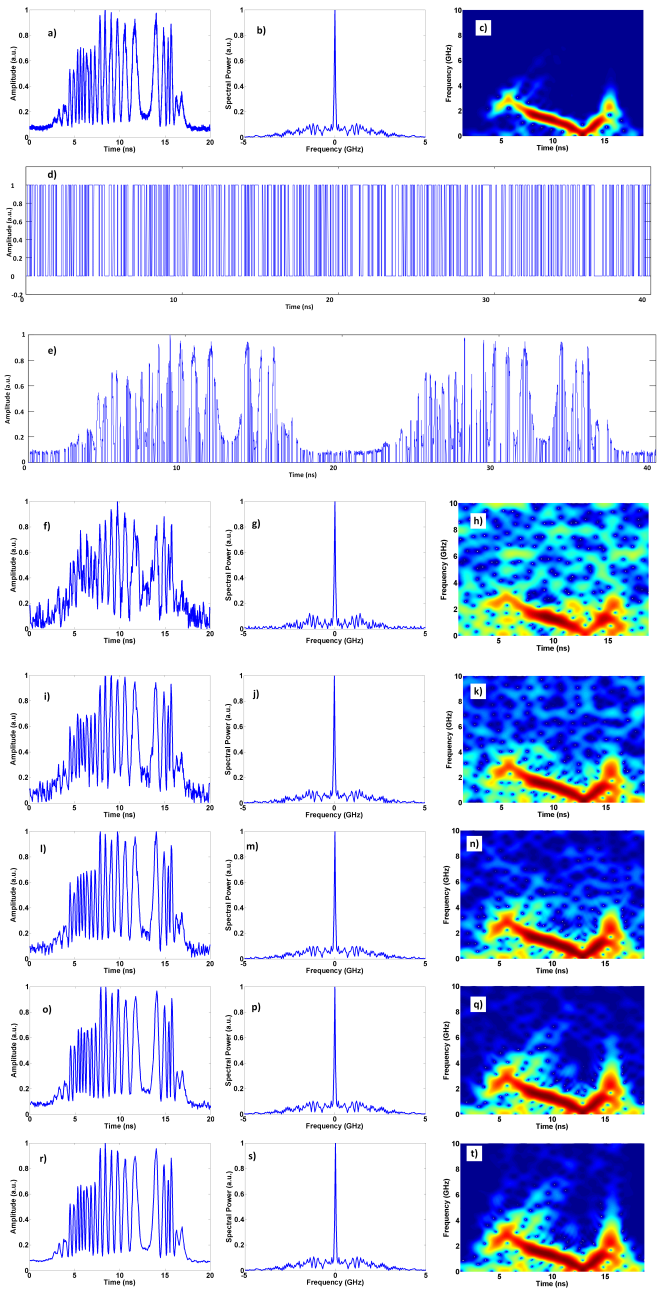

Fig. 3.26 Simulation results for TD-PCS-FBG system with S-shaped strain profile. a. Original time stretched sensing signal in time domain b. FFT respresentation of the time domain signal c. Spectrogram of the sensing signal showing linear frequency chirp d. Two PRBS sequences used for mixing e. Mixed signal with PRBS and sensing signal. f. Time domain reconstruction of sensing signal upon l_1 reconstruction with 50% compression ratio g. Corresponding FFT domain representation h. Spectrogram showing clear chirp profile. The l_1 reconstruciton results are repeated for 62.5%, 75 % ,87.5% and 100 % compression ratios and the time domain reconstruction is shown in Fig. i. l. o. and r. , corresponding FFT domain representation in Fig. j. m. p. and s. , and corresponding chirp profiles are shown in Fig. k. n. q. and t.

balanced setup, the output should be single tone sine signal with constant RF frequency. However, if the strain is introduced the signal is distorted and would produce a chirped signal. For one such setting the output signal is shown in Fig. 3.25.a and corresponding FFT representation is shown in Fig. 3.25.b where it can be observed that the wideband signal has 6GHz as maximum frequency. The spectrogram is shown in Fig. 3.25.c. showing downward chirp from few GHz to MHz. A binary PRBS is generated with 20Gbps bit rate or 50ps bit period making the signal length N=400. Two such sequences each with length 400 are shown in Fig. 3.25.d. and corresponding electro-optically mixed signal is shown in Fig. 3.25.e. The sensing signal is mixed with m number of PRBS sequences each of length 400 and are optically integrated to represent a single measurement which can be captured at 50MHz speed. The sensing signal can be reconstructed using l_1 minimization algorithm as described in section 2.2. Solving the equation 2.16, the signal can be reconstructed. With 250 measurements, a compression ratio of 62.5 %, the time domain and corresponding FFT and spectrogram is shown in Fig. 3.25.f,g,h respectively. As it can be observed from Fig. 3.25.h, the downward chirp can be easily recognized and the chirp slope determines the strain induced in the sensing FBG with respect to reference FBG. Similarly the number of measurements,m are increased from 250 to 400 in steps of 50 and the results are shown respectively. As it can be observed, the reconstructed signal,FFT and spectrograms are close to match original sensed signal. Hence, with 60 % measurements, the strain parameters can be obtained instead of sampling the complete signal saving the storage space with high speed electronic detectors [63].

3.3.1.2 S-shaped profile

The results are repeated for S-shaped strain profile and original sensed signal is shown in Fig. 3.26.a. and corresponding FFT and spectrograms are shown in Fig. 3.26.b and 3.26.c respectively. The PRBS sequences and mixed signals are shown in Fig. 3.26.d and 3.26.e

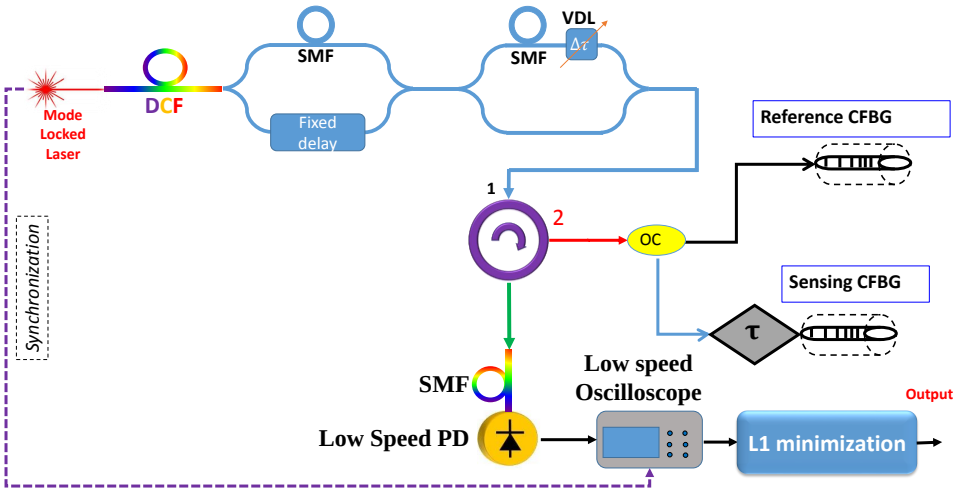

Fig. 3.27 Schematic of proposed and simulated SD-PCS-FBG system with all-optical random patterns generated from cascaded MZI setup

respectively. With number of measurements m = 200, the reconstructed signal along with FFT and spectrograms are shown in Fig. 3.26.f,g,h respectively and the results are repeated in steps of 50 from 250 to 400. The sensing signal has low maximum frequency of 3GHz compared to signal represented in 3.25.a. Hence it required few number of measurements to get the spectrogram with a compression ratio of 50 %.

3.3.2 Results with Spectral Domain Photonic Compressed Sensing

In this section, the results with SD-PCS system based on cascaded MZI structure have been presented.

As shown in proposed schematic Fig. 3.27, the time stretched pulses from passive mode locked laser and -1.044ns/nm DCF are directed through cascaded MZI setup where MZI-1 has variable delay in one arm and 500m Single mode Fibre(SMF) in another arm where as MZI-2 has optical variable delay and SMF in one arm and direct connection in another arm making both the MZIs of opposite chirp. The variable delay of the first MZI is varied from 0ps to 50ps in steps of 5ps and variable delay in MZI-2 is varied from 1.25ps to 50ps

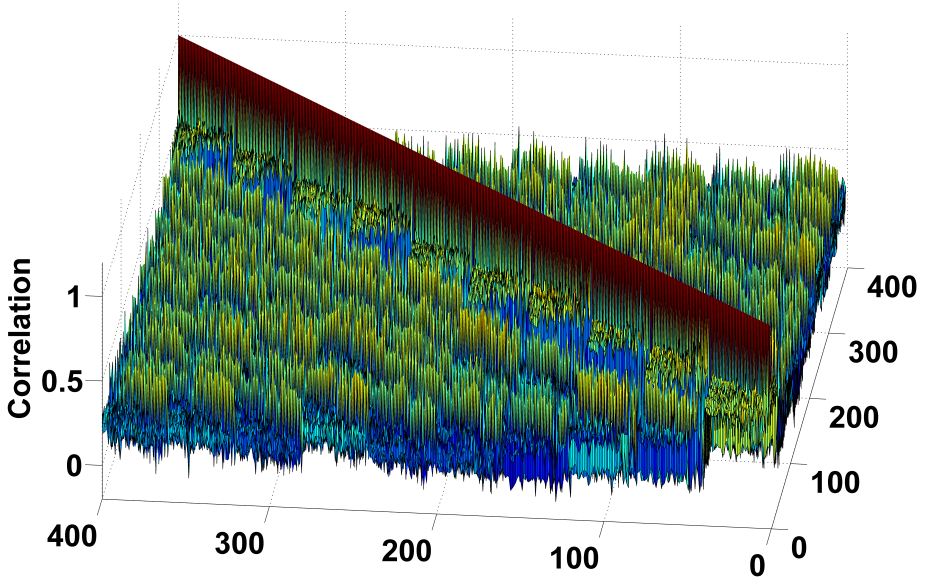

Fig. 3.28 Correlation between the patterns generated from cascaded MZI setup for SD-PCS-FBG system

insteps of 1.25ps producing overall 400 patterns. The patterns are quasi random and the cross correlation between the patterns are shown in Fig. 3.28 that has maximum cross correlation of 73 % removing the highly correlated tail part which can be further improved using high GVD single mode fibre. These patterns are now directed to FBG interrogation setup resulting in embedded strain information. The mixed patterns are compressed with 1.044ns/nm SMF for the purpose of optical integration which can be easily detected by low pass 50MHz photodetector followed by low speed electronic digitizer hence reducing the overall speed of electronic detectors and eliminating the need for high bandwidth binary PRBS generation. This also reduce the optical loss due to electro-optic mixing in the conventional PRBS mixing as all-optical random pattern generation has been used hence reducing the need for high optical amplification saving the energy. However, the patterns should be reproducible for faithful reconstruction.

The measurements acquired and corresponding patterns used for the process are given as inputs to l_1 reconstruction algorithm and the results for monotonic chirp signal are shown

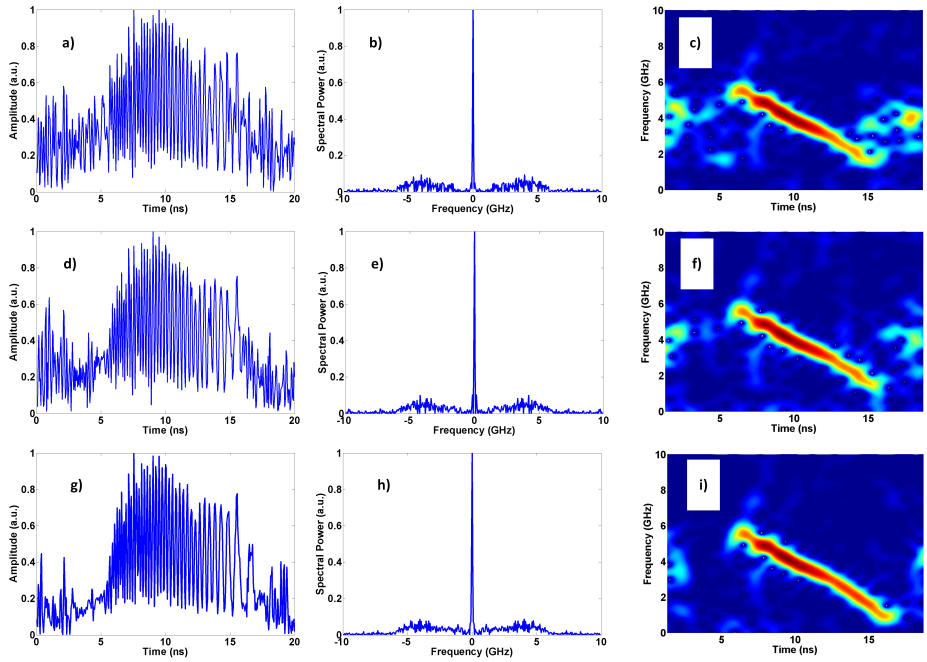

Fig. 3.29 Reconstruction results for downward chirp signal with all-optical random pattern generation and mixing. a. Temporal domain reconstruction with 200 measurements with 50% compression ratio. b. Corresponding FFT domain with 200 measurements with 50% compression ratio. c. Spectrogram of the reconstructed signal. The results with 62.5% and 72.5% compression ratios are shown respectively with time domain reconstruction in Fig. d. and g. , corresponding FFT domain representation in Fig. e. and h., and corresponding chirp profiles are shown in Fig. f. and i.

in 3.29. First column shows the time domain reconstruction of downward chirp signal with 50%, 62.5% and 72.5% compression ratio respectively and second column shows the FFT representation of reconstructed signal followed by third column with corresponding spectrograms confirming the chirp slope and the results are in agreement with actual input signal 3.25.a . The results for S-bend chirped signal are shown in Fig. 3.30 with 50%, 62.5% and 72.5% compression ratio respectively confirming proposed theory of all-optical random pattern generation for wideband signals and can be compared with the original signal 3.30.a.

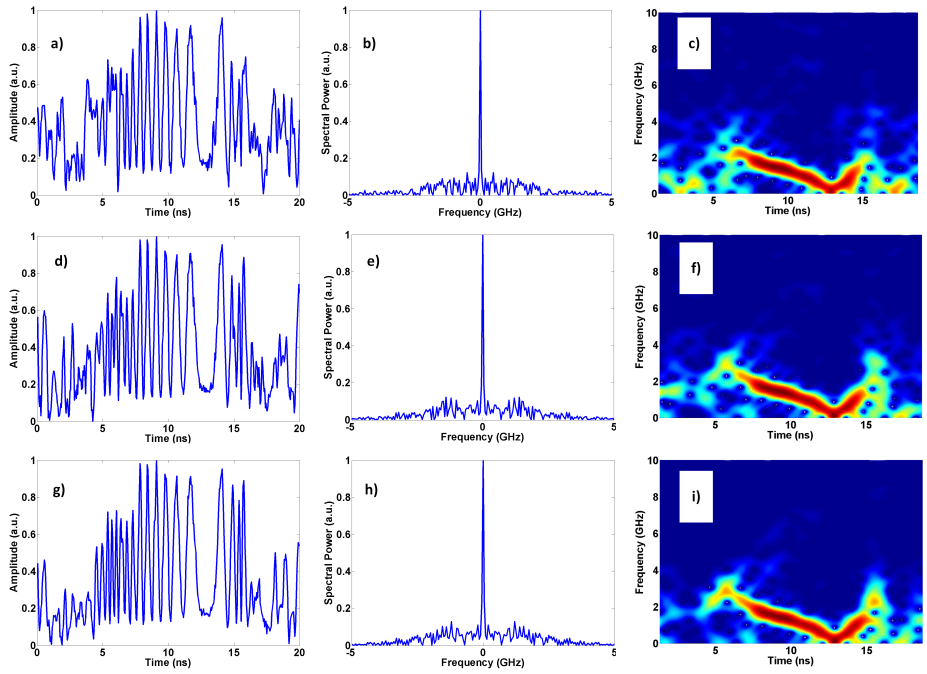

Fig. 3.30 Reconstruction results for S-bend chirp signal with all-optical random pattern generation and mixing. a. Temporal domain reconstruction with 200 measurements with 50% compression ratio. b. Corresponding FFT domain with 200 measurements with 50% compression ratio. c. Spectrogram of the reconstructed signal. The results with 62.5% and 72.5% compression ratios are shown respectively with time domain reconstruction in Fig. d. and g. , corresponding FFT domain representation in Fig. e. and h., and corresponding chirp profiles are shown in Fig. f. and i.

3.3.3 Discussion

In this section, Time Domain and Spectral Domain Photonic Compressed Systems have been demonstrated for strain profiles from distributed FBG interrogation method. As explain in section 3.1.8, the time stretched optical pulse is associated with 3dB electrical bandwidth of 200MHz. Hence, the actual spectrum to be detected will be a convolution of electrical bandwidth of time stretched optical pulse with actual wideband chirp signal that has been encoded. In TD-PCS-FBG system, the compression ratio is as high as 62.5% as the number of non zero tones to be retrieved are higher. However, SD-PCS-FBG system offers better compression ratio of 50% as the random pattern is guassian and works best if the random patterns generated are stable and reproducible. The RMSE has been calculated and repre-

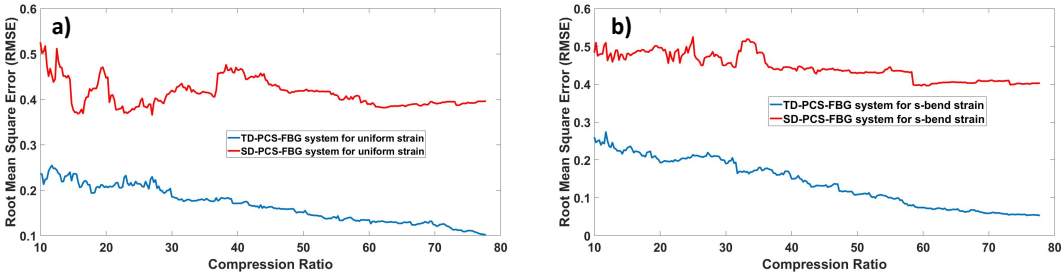

Fig. 3.31 Root Mean Square Error results for TD-PCS-FBG system and SD-PCS-FBG system. a) RMSE as a function of compression ratio for uniform strain signal b) RMSE as a function of compression ratio for S-shaped strain signal

sented in Fig. 3.31. It can be observed that RMSE is higher for SD-PCS system compared to TD-PCS system mainly due to the tail part of the random sequence which does not have any power.

3.3.4 Conclusion

Already existing TD-PCS and novel approach of SD-PCS system based on cascaded MZI system have been simulated for measuring strain signal encoded by distributed FBG interrogation. While a wideband signal has been sensed with low speed detectors in TD-PCS-FBG system, the compression of 50-70% has been achieved. SD-PCS-FBG system offers better compression ratio of 50% with careful calibration of random patterns.

3.4 Overall Summary

In this chapter, Time Domain Photonic Compressed Sensing method has been presented for Optical Coherence Tomography and achieved 66% data compression for single layer model with experiment results. This is achieved by encoding 33 sets of Pseudo Random Bit Sequence of 2.5GS/s data rate with OCT axial scanning information signal. The MLL generates optical pulses at 50MHz repetition rate. Since 33 pulses are required to reconstruct this information, the A-scan rate is 1.51MHz. A method has been proposed to improve the

resolution beyond the theoretical limitation of 50MHz by dual pulse integration. Spectral Domain Photonic Compressed Sensing method has been demonstrated using spectral filter built by cascaded MZI structure for RF spectrum sensing hence achieved 10% compression with reconstruction of dual tone signal. Approaches for compressed FBG sensing achieving 60% data compression have been proposed with results.

Chapter 4

Spatial Domain Photonic Compressed Sensing for Ultrafast Single-Pixel Imaging

This chapter is an extended version of a published paper[67].

In this chapter, real time ultra-fast imaging method based on compressed sensing has been proposed utilizing wavelength dependant spatial domain random patterns. This is second type of Photonic implementation of Compressed Sensing that has been discussed in chapter 2. This system has been abbreviated as UF-PCS imaging system through out this chapter.

Followed by introduction of Single-pixel imaging and ultra-fast imaging methods, the main principle of UF-PCS imaging system has been presented followed by experiment and numerical results.

4.1 Introduction

Single Pixel Imaging: As explained in chapter 2.2 and [44], Single Pixel Imaging has been emerged as an alternative modality to direct imaging with advantages such as reduction in size, complexity, cost and improved fill factor. Single Pixel Imaging can be implemented with Raster Scan, Basis Scan or Compressed Sensing approaches. While Raster Scan and Basis Scan methods takes same number of measurements as number of pixels resulting 100% sampling of the image, Compressed Sensing method reconstructs image with reduced number of measurements depending on the sparsity of acquiring image.

In general, Single Pixel Imaging based on Compressed Sensing can be implemented with SLM or DMD. However, these devices suffer from slower refresh rate of few Hz. Recently, this method has been improved and demonstrated with time domain Photonic Compressed Sensing required electronic PRBS generators for electro-optic mixing which are expensive and require electro-optic conversion along with significant amplification. However, the imaging rates cannot exceed few KHz as multiple pulses are needed to capture image. Research efforts have been made by pre-compressing low PRBS encoded optical pulse for enhanced bit rate requiring Electro-optic modulator and dispersive elements in photonics domain [165]. Efforts have been made by generating random patterns as an alternative to electronic PRBS to eliminate electronics part in generating random sequence through multi-mode interference methods which requires PD array to sense the compressed measurements[173] and multicore fibers requires wavelength scanning mainly for imaging[174], spatial resonance methods[133]with special component fabrication, generation of multiple path spectral filters based on customized fabrication micro-ring silicon based resonators.

Ultra-fast Single Pixel Imaging Ultrafast imaging systems are of essential for analysing transient and non repetitive events in single shot approach as explained and reviewed in [32]. The applications of the mentioned approaches being laser pulse characterization and other

non-linear phenomenon.Ultra-fast imaging systems can be broadly classified into 2 categories. 1) Burst sampling 2) Continuous sampling. Majority of ultra-fast imaging methods would either be applied only for very short time such as ps time scale[96] which included PTS based Sequentially Timed All-optical Mapping Photography (STAMP) method and CS based Compressed Ultrafast Photography (CUP) methods. These ultrafast burst imaging systems are hence limited to isolated ultra low time scales and are limited by electronic digitizers and sensors. On the other hand, real time continuous sampling has applications in biomedical imaging systems which, demands continuous sampling of diagnostics information[175]. The current state of the art STEAM imaging is a single pixel imaging method which has continuous sampling scheme however, this results in continuous generation of data that need to be sampled. Huge amount of data has to be compressed at the time of saving to disk using JPEG compression and other digital compression techniques which demands data compression in High speed imaging system. In this chapter, the ultra-fast imaging requirement has been combined with current Spatial Domain Photonic Compressed Sensing systems to demonstrate Spatial Domain Photonic compressed sensing enabled ultra-fast imaging system. This has been abbreviated as UF-PCS system. In UF-PCS system, a new approach for ultrafast (20 Mfps) structured illumination single-pixel imaging using light beam speckles out of a multimode fiber due to multimode interference. The experimental results show that excitation of high-order modes, and hence the multimode interference, are strongly wavelength-dependent. Cross correlation result of 500 wavelength-dependent optical speckle patterns shows flat and low correlation of 7.4% between different illumination patterns, verifying the utility of multimode interference based structured illumination in UF-PCS imaging system. By measuring multiple dot products of a sparse image with a set of known speckle based random patterns generated by wavelength dependent chaos inside multimode fibre structure, the image can be reconstructed using an l_1 minimization algorithm. Update of the random speckle pattern can be easily obtained by sweeping the incident

wavelength which is achieved by stretching ultra-fast optical pulses from a mode-locked laser using chromatic dispersion i.e., PTS principle. Therefore, imaging speed as high as the repetition rate of the pulse train, which is 20 MHz in our system, can be achieved. As the number of wavelengths are 500 in steps of 0.1 nm, a successful reconstruction of 27X27 pixel image with a compression ratio of upto 20% has been demonstrated.

4.2 Principles

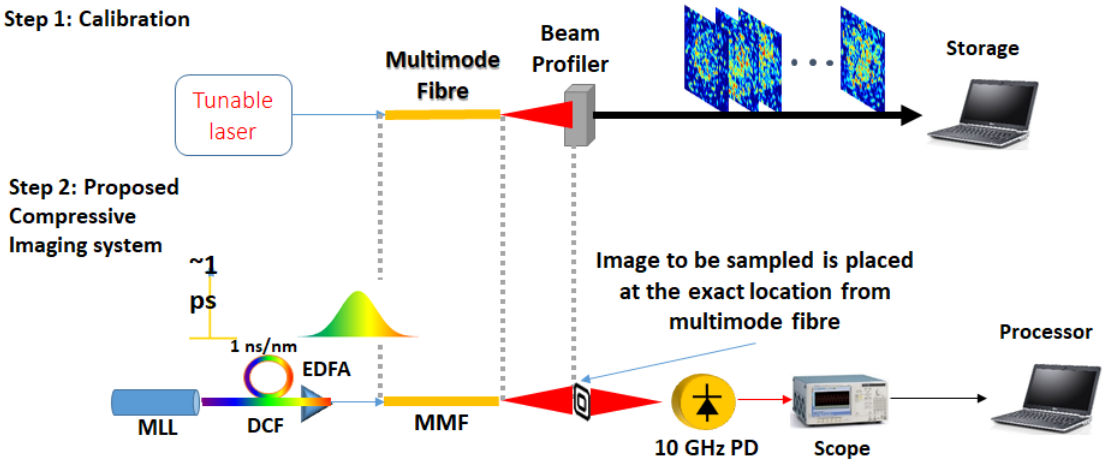

Fig. 4.1 Schematic of Proposed UF-PCS imaging system. Step-1 is performed with experimental setup with tuneable laser source. Step-2 is verified through simulations in MATLAB. Step 1:Experimental calibration. Step 2: Proposed Compressive Imaging system. MMF:Multimode Fibre, Storage: A computer used used to record and store the patterns, MLL:Mode locked laser with a pulse with of 800fs and repetition rate of 20MHz, DCF: Dispersion Compensating Fibre of 1ns/nm chromatic dispersion, PD:free space Photo Detector, Processor: A computer with signal processing capability to extract the image from measurements acquired from scope and patterns recorded from calibration

The schematic is shown in Fig. 4.1. The tunable laser source with wavelength range from 1518nm to 1568nm emits single wavelength continuous optical beam onto a collimator(NA = 0.49). The beam size is expanded using 4-f lens setup (two plano-convex lens with 30mm and 100mm focal lengths). An objective lens(X10, 0.4NA) is used to couple the light into

Multimode fibre(2m length, core diameter of 200 μm, 0.39 NA).The entire imaging process involves 2 steps. In step-1, the speckle patterns are recorded with a beam profiler with light passing through Multimode Fibre from a single wavelength source with optical lens setup. Because of the cross talk between different spatial modes, this causes intensity distribution in the spatial domain which can generate quasi random spatial pattern. The pattern is different for each wavelength. A tunable laser source is used to sweep the wavelengths from 1518 nm to 1567.9 nm with step width of 0.1 nm manually. Four of the recorded patterns are shown in Fig. 4.2.

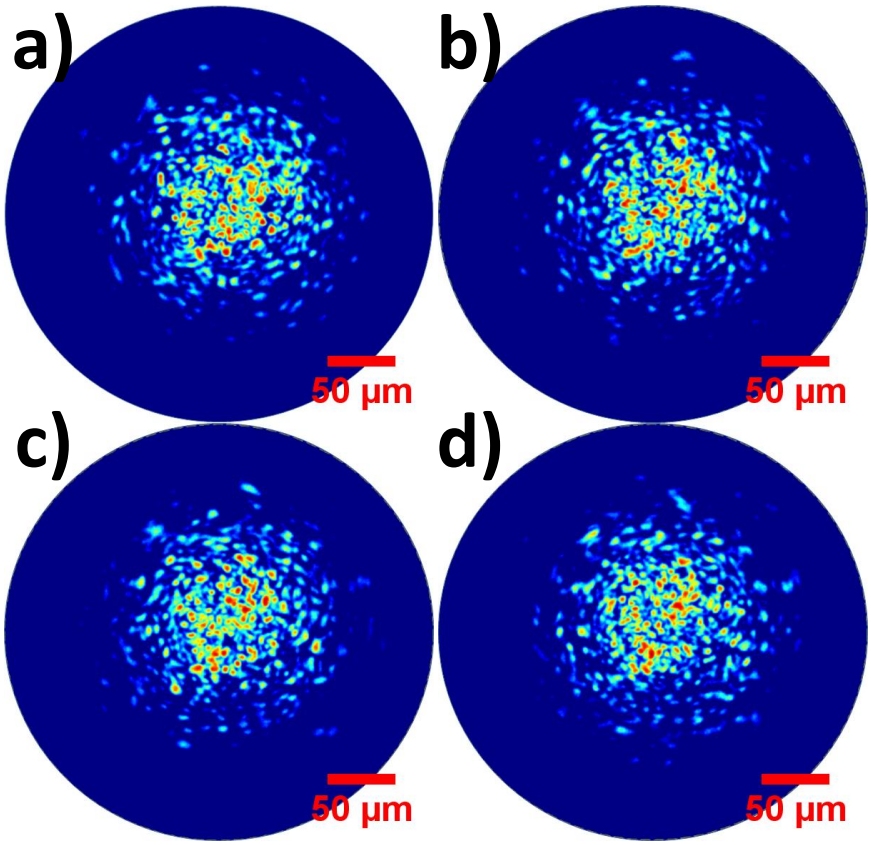

Fig. 4.2 Four of the recorded patterns from beam profiler. The wavelength step size considered is 0.1 nm from 1550 nm

As observed, The patterns are quite distinct from other and this can be evidenced by calculating cross correlation matrix shown in 4.3 for first 500 patterns observed with average cross correlation is calculated to be 7.4%.

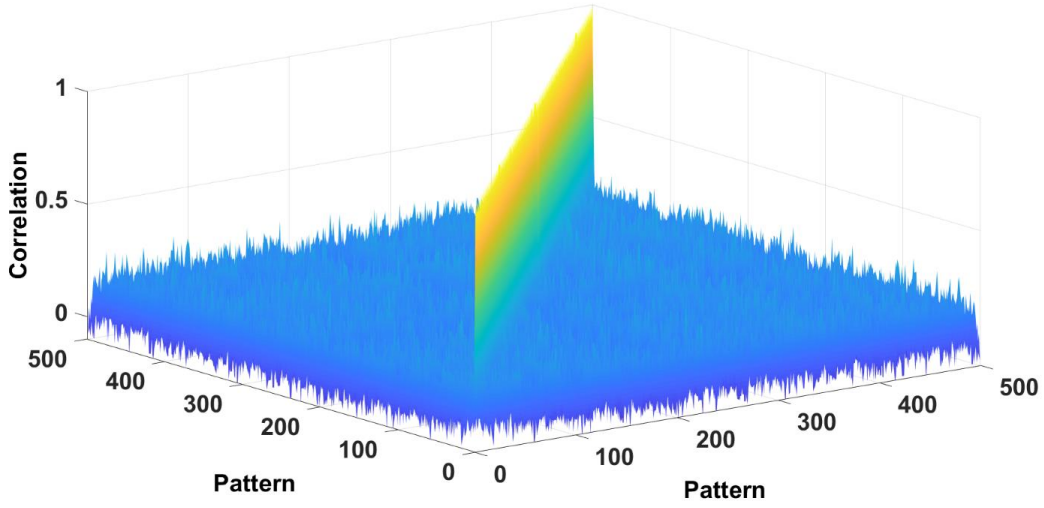

Fig. 4.3 Correlation matrix of the patterns recorded from beam profiler. This is a symmetric matrix with diagonal being represented by the auto correlation of the pattern which is close to unity.

In any compressed sensing process, a set of ideal random patterns are expected to be repeatable as accurately as possible. Since the random patterns are now generated using chaotic nature of Multimode Fibre, the stability of the patterns over the time has been recorded and is shown in Fig. 4.4. It has been observed that the correlation does not change significantly over time with 0.97 over the time of 2 hours. So the image can be mixed at a later time against the pattern being recorded with beam profiler. The difference in time can be a maximum of around 2 hours and calibration can be repeated there after for every 2 hours for reliable reconstruction.

Having recorded these patterns, the passive mode locked laser with 800fs pulse width and 20MHz repetition rate to generate a series of ultra-short pulses which are time stretched with 1ns/nm DCF hence creating injective mapping between temporal and wavelength domain thus achieving the high speed sweeping of wavelengths in time domain at a rate of 20MHz. Assuming that wavelength spacing as 0.1nm, this can generate 500 wavelengths in 50 ns. The stretched pulse goes through Multimode fibre and each wavelength undergoes chaotic spacial

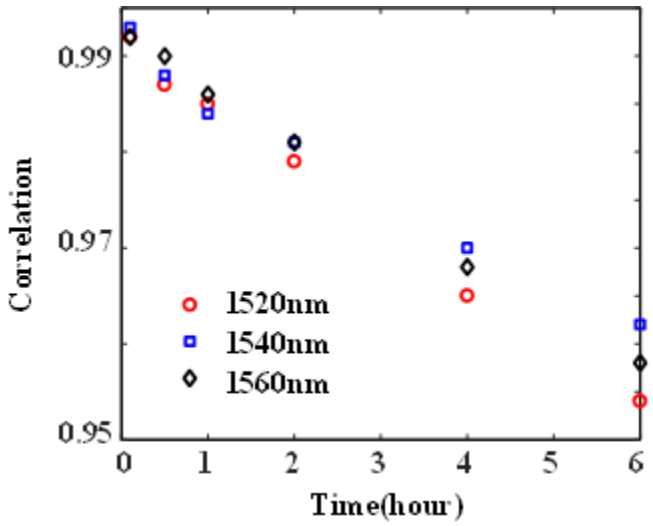

Fig. 4.4 Self correlation variation for three wavelengths against time duration.

mixing generating a random pattern and mixes with the image placed after the fibre and all 500 wavelengths mixes with the image generating 500 measurements which will be detected with high speed free space Photo detector 10GHz and high speed electronic oscilloscope. It is essential that scope and Mode locked laser are synchronized to get the corresponding measurement for corresponding wavelength. A naturally sparse image of 27X27 pixel size can be reconstructed with these many wavelength based patterns. A numerical demonstration has been presented here.

The post processing involves reconstruction of the image from the measurements captured from scope and patterns recorded from beam profiler. The theory of compressed sensing has been presented in chapter 2.

4.3 Results

Two aspects of results have been presented. One aspect describes the data compression by utilizing spectral sparsity and comparison of the reconstruction results against traditional STEAM output with same data size output.

Second aspect describes the resolution limit of the speckle patterns based compressive imaging system. Also, a detailed explanation of finding the Nyquist spatial frequency has been presented here.

4.3.1 Reconstruction of image and comparison with traditional STEAM imaging

The reconstruction results have been presented for a sample image shown in Fig. 4.5.a. with various number of wavelengths/measurements upto maximum of 500 wavelengths which is the fundamental limit of the proposed system hence maximum compression rate is 68% for 27X27 pixel image. The results are presented in comparison with direct down sampled images illustrating CCD images.

Speckle patterns based CS results obtained above have been compared with conventional binary patterns based CS. The results are presented in Fig. 4.6.

4.3.2 Resolution information from the random patterns

In this subsection, an approach to estimate Nyquist sampling rate has been presented for the proposed system by measuring the recognizable spectral power of the calibration equipment which in this case is beam profiler.

Though the pixel resolution is 540X540, the random pattern cannot resolve the image of that size as the spatial resolution is limited by the average grain size of speckle patterns. The actual random pattern captured by the beam profiler along with spectral profile of the

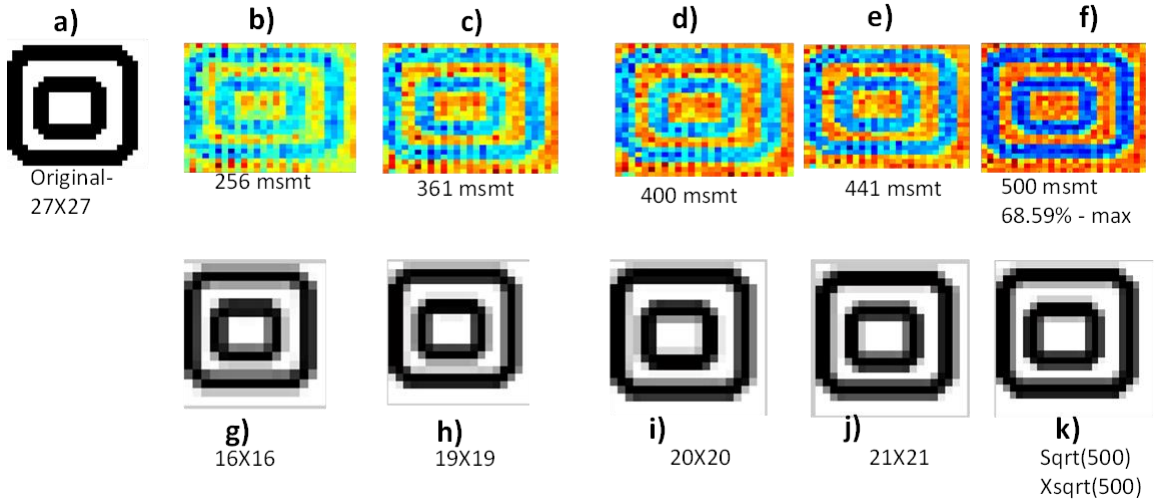

Fig. 4.5 Comparison of results with compressed imaging and conventional STEAM sensing. a) Original image with pixel size 27X27. b) to f) Reconstructed images with l_1 minimization algorithm from with increased number of measurements. g) to k) The sampled images from traditional STEAM imaging system which are emulated by downsampling the original image.

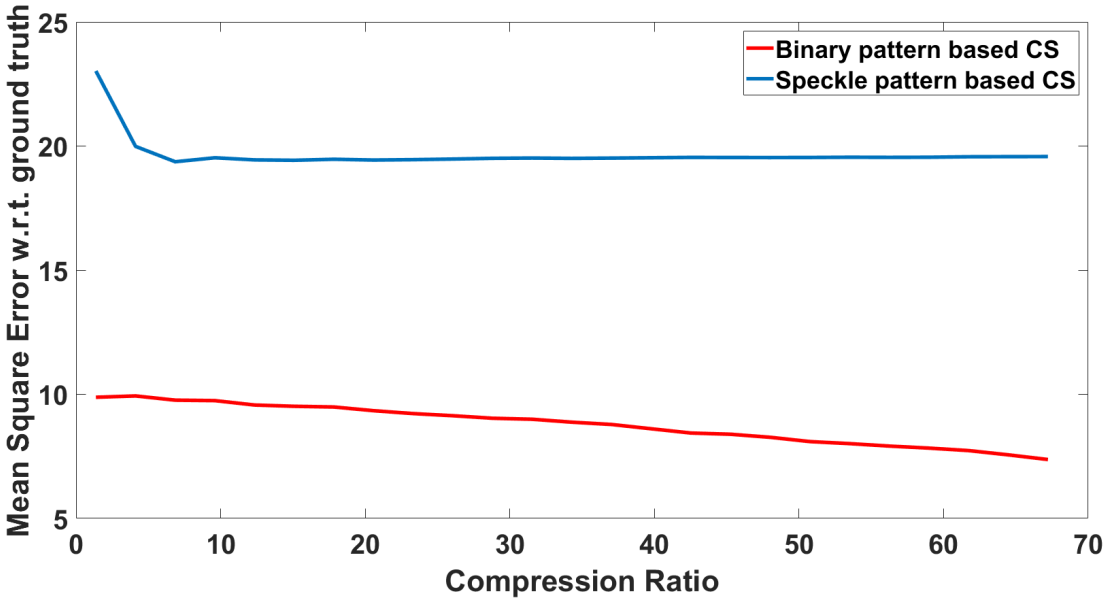

Fig. 4.6 Comparison of MSE for speckle based compressed imaging vs binary patterns based compressed imaging

random pattern is presented followed by several spatial low pass filters to remove the high frequency components to see any significant difference in the pattern.

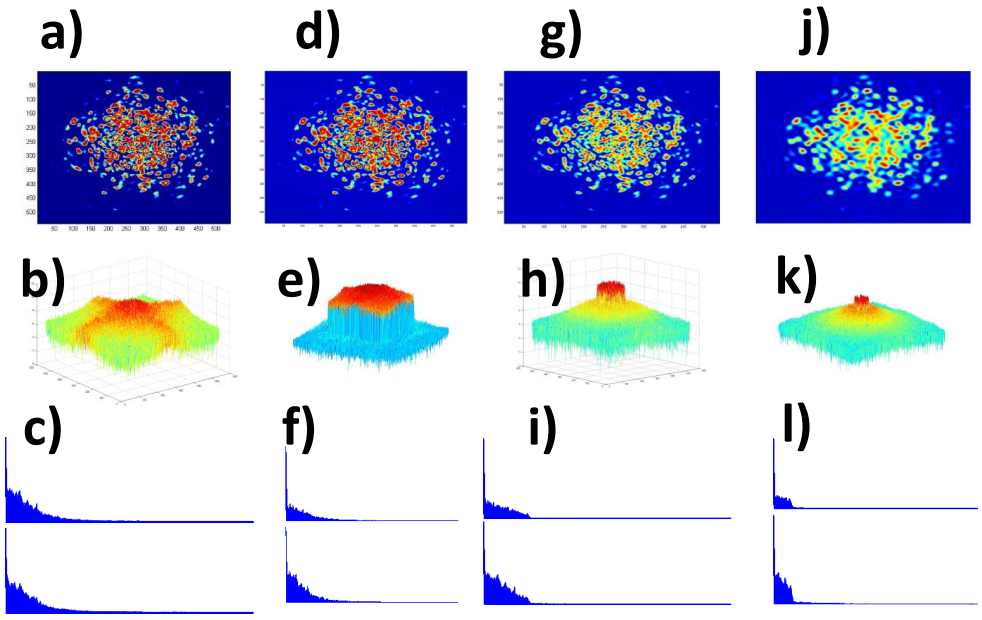

Fig. 4.7 Nyquist resolution limit. a)Pattern captured by beam profiler with 540X540 pixel resolution b) 2D spectral domain representation after removing the low frequency components c) Superimposed spectral domain representation of individual rows of the image followed by columns of the image shown in Fig. a. d) The random pattern after removing the high spatial frequency low spectral power components shown in Fig. f. e) Corresponding 2D spectral FFT f) superimposed representations after removal of high frequency components g) The random pattern after removing the high spatial frequency low spectral power components shown in Fig. i. h) Corresponding 2D spectral FFT i) superimposed representations after removal of high frequency components j) The random pattern after removing the high spatial frequency low spectral power components shown in Fig. f. k) Corresponding 2D spectral FFT l) superimposed representations after removal of high frequency components.

As observed, the actual figure captured by beam profiler with 540X540 pixel resolution is shown in Fig. 4.7.a. The corresponding 2D spectral domain representation is shown in Fig. 4.7.b. after removing the dominant low frequency component with a low pass filter and actual spectral power variation is shown in Fig. 4.7.c where the spectral power significantly falls for higher spatial frequencies. The higher spatial frequencies >150 are now suppressed using a low pass filter and the result is shown in Fig. 4.7.f. The corresponding random pattern is

shown in Fig. 4.7.d. and the corresponding 2D FFT representation is shown in Fig. 4.7.e. Similarly the superimposed spectral domain representations of the pattern after removing the higher spatial frequencies >50 are shown in Fig. 4.7.i and corresponding random pattern is shown in Fig. 4.7.g and 2D FFT representation is shown in Fig. 4.7.h. and the procedure is repeated for spatial frequencies >25 and are represented in Fig. 4.7.l, 4.7.k and 4.7.j. As observed from the patterns with original 4.7.a and suppressed high frequency random pattern in Fig. 4.7.j, some of the high frequency features have been lost marginally and this can be considered Nyquist frequency limit for the system. Hence any 50X50 image can be successfully reconstructed by the CS system.

4.4 Discussions

In this proposed setup, a tunable laser is used to sweep the wavelengths to record the speckle patterns at the distal end of the multimode fibre and the patterns are used for CS imaging method in simulation environment. However, in general case, a MLL is used to sweep the wavelengths at a faster rate determined by repetition rate of the laser and it is crucial to calibrate the each wavelength generated from MLL. This can be done by using programmable optical filter or a combination of diffraction grating and amplitude SLM to allow only one wavelength with linewidth. Once the imaging system is calibrated, the optical filter can be removed or all one pattern can be inputted to allow all wavelengths.

4.5 Conclusion

In this chapter, an ultrafast imaging technique(UF-PCS system) that captures sparse image within 50ns time scale has been demonstrated. This has been achieved by attributing wavelength dependant chaos of multimode fibre structure to conventional compressive time stretch imaging system. The random patterns were generated experimentally by sweeping the

wavelength from 1518nm to 1567.9nm with 0.1nm wavelength step followed by multimode fibre structure. Thus, generated random speckle patterns have been analysed for all 500 wavelengths. A 27X27 pixel image assumed to be sparse in some transformation domain has been considered and computationally mixed with experimentally generated patterns and integrated to single power measurements which represent the corresponding dot product of the wavelength dependant random speckle pattern with given 2D image and the results are compared against conventional STEAM imaging. The variation of random pattern as time duration is observed and it linearly reduces to 95% for a duration of 5 hours. The cross correlation of all 500 patterns are calculated to show the incoherence nature of these speckle patterns and minimum cross correlation is observed to be around 7.4% indicating the patterns are repeatable and incoherent. Hence can be used in compressive imaging system. A method to calculate the Nyquist resolution limit has been presented for generated random pattern. The pattern's 2D FFT is taken and using a digital lowpass filtering techniques, the high spatial frequency information is zeroed out to see any significant difference in the pattern. After removing the spatial frequencies from 25, the pattern varies significantly from original pattern, hence it can be concluded that the number of resolvable points in the random pattern is around 50X50. Since the considered image is 27X27, it is well within the expected resolution limit. The capability can be further improved by exciting more modes in the multimode fibre structure using mode scrambler enabling higher Nyquist rate limit.

Chapter 5

All-optical FFT scanning for blind spectrum sensing

This chapter is an extended version of a published conference paper[54].

In this chapter, an all-optical approach for FFT scanning for blind RF spectrum sensing has been proposed and experimentally demonstrated. This method can be classified as Basis Scan methodology of Single Pixel Imaging. Compressed sensing based on Single Pixel Imaging requires specific set of random patterns and information sparsity is a prerequisite for enabling data compression. In case of Basis Scan, any arbitrary signal can be sensed by scanning in a particular basis. Here, a novel all-optical approach of Fourier basis scan has been demonstrated with a proof-of-concept experimental demonstration for RF spectrum sensing.

5.1 Introduction

As discussed in chapter 2, there has been research on acquiring an image without direct line of sight by acquiring the Fourier spectrum. In [56], a technique has been proposed to illuminate

the image with a N-step phase shifting(N=4) sinusoidal harmonic patterns instead of binary patterns and the imaging can be reconstructed with IFT algorithm. However the method suffers from low imaging speed and low acquisition time. The method has been improved with photonic time stretch based phase shifting as proposed in [55] where pattern generation rate is increased and acquiring speed has been significantly improved by phase shifted RF generated sinusoidal patterns by employing Arbitrary waveform generator. However, the maximum scanning frequency is limited by AWG sampling rate and is also expensive. This technique requires Electro optic modulator which is also bandwidth limited and lossy.

In this chapter, a novel all-optical FFT scanning method has been proposed for sensing arbitrary RF signal based on variable optical delay and phase modulator based MZI which produces modulated and phase shifted gaussian pulses without any need for RF equipment and and also removes electro-optic modulator for generation. Upon electro-optic mixing of unknown RF signal and optical integration, the FFT can be acquired. With this approach, FFT reconstruction of single tone 1GHz, dual tone (1GHz, 2.5GHz) and multitone signals(0.4GHz, 1GHz, 1.8GHz, 2.5GHz) have been demonstrated experimentally.

The method and results are presented in subsequent sections with section 5.2 explaining the principles used in this set up and in section 5.3, the experimental results have been presented. In section 5.4, limitations and prospects of the method has been discussed followed by conclusions in section 5.5.

5.2 Principles

The schematic of proposed experimental setup is shown in Fig. 5.1. A passive MLL is time stretched using DCF thanks to Dispersive fourier transformation technique, time to wavelength mapping has been established and can be represented by,

$$\Delta\lambda = \frac{\Delta t}{\ddot{\Psi}} \tag{5.1}$$

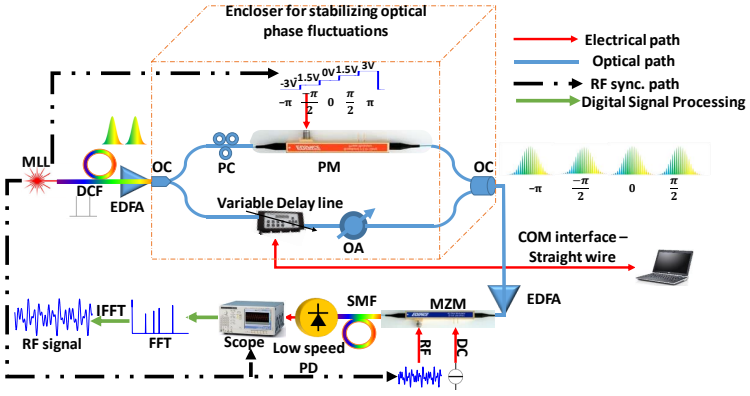

Fig. 5.1 Schematic of experimental set-up. OC:Optical Power splitter/Combiner, PC:Polarization Controller, PM:Phase Modulator, DC: DC bias signal, IFFT: Inverse FFT , RF Sync.:RF synchronization, EDFA: Erbium Doped Fibre Amplifier

The time stretched pulse has been directed to Mach-Zehnder interferometric setup with one arm being programmable/tunable optical delay and other arm equipped with polarization controller and electro-optic phase modulator with static delay compensated in both the arms at pre-experiment stage. By tuning the optical delay in MZI structure, Change in optical delay results in encoded gaussian pulse as per,

$$\Delta f_{RF} = \frac{c \times \Delta t}{\lambda^2 \times \ddot{\Psi}} \tag{5.2}$$

The input to the phase modulator is a variable power supply or programmable power supply with 5 different voltage levels synchronized with MLL at sampling rate same as repetition rate of the mode locked laser. This can be achieved by an FPGA or a low speed AWG followed by an RF amplifier. The output of MZI is a 4-phase shifted and modulated gaussian pulses. Modulating with unknown RF signal with help of electro-optic modulator biased at quadrature point and integrating the each RF mixed optical pulses and followed by digital signal processing, FFT magnitude spectrum of the original signal can be reconstructed and time domain waveform can be reconstructed with IFT algorithm as explained in chapter 2.

5.3 Experiment Results

A proof of concept experiment has been designed and implemented based on conceptual schematic shown in Fig. 5.1. In experiment, a passive MLL(Calmar Mendocino FP laser) generates a series of ultra-short optical pulses with FWHM 800fs and 50MHz repetition rate. Each pulse is time stretched with DCF(OFS SMFDK-S-020-03-01) and amplified to achieve observable time-frequency mapping and directed to MZI setup consisting of PM-PC in one arm and Variable Optical delay(VDL-001) in another arm. The optical time delay between paths of MZI converts to an RF frequency that can be described by eq. 5.2 . PM modulates the phase of the optical carrier with respect to the RF signal applied which in this case is a variable power supply, a stair case RF signal with 1.5V step size from -3V to 3V repetitive of 100ns.

5.3.1 System calibration

The static RF delay should be compensated at the pre-experimental stage and static optical delay in MZI arms is compensated by adding additional fibres of few cm length. By tuning the delay from 0ps to 50ps in steps of 0.5ps and by measuring the RF frequency for each delay step, the result is obtained as shown in Fig. 5.2 and are compared against theoretical calculations obtained from eq. 5.2 represented in black color. The offset occurs mainly due to adjustments in fibre arms to improve the visibility and position of Polarization Controller. Hence the system requires calibration of offset for every experiment and is not fixed. The offset is adjusted by shifting the experimental results as shown in Fig. 5.2. The time domain waveform for an optical delay of 10ps is shown in inset along with its RF frequency spectrum. As the optical delay is tuned from 0 to 50ps , the frequency of the time domain waveform shifted from 0 to 6 GHz. The optical pulses are observed for individual DC voltages are shown in Fig. 5.3 confirming the phase shift in interferogram upon DC voltage.

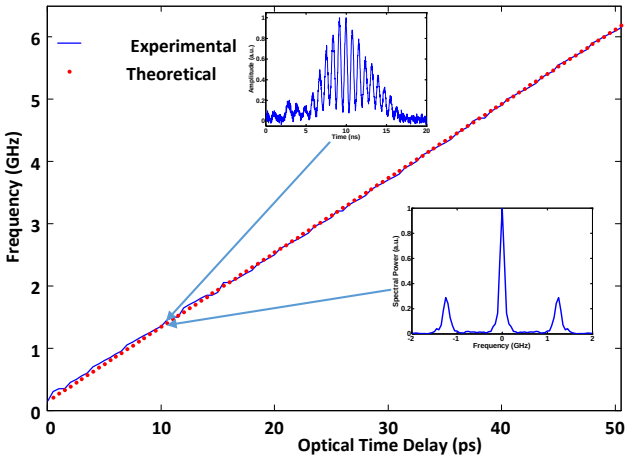

Fig. 5.2 Time delay - Frequency relation after adjusting the offset. The insets show the time domain and FFT representations at a particular optical delay of 130ps. Blue color shows the experimental result. The results from theoretical calculations is shown in red

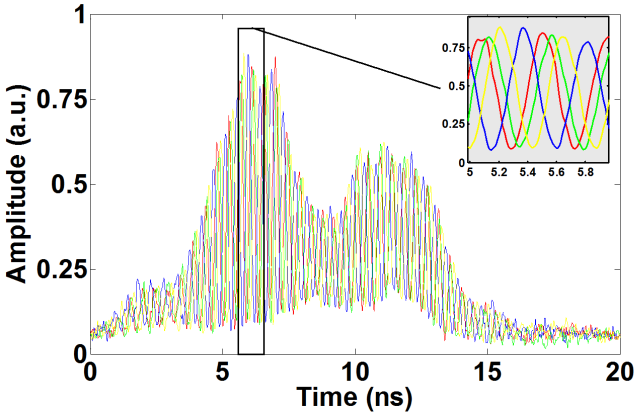

Fig. 5.3 Optical pulse comparison for individual DC voltage applied to phase modulator.

5.3.2 Single tone reconstruction

The output of MZI,phase shifted interferogram is electro-optically modulated with amplified arbitrary RF signal, in this case 1GHz RF signal. The output is captured for every optical delay with a delay step of 0.5ps acquiring 103 power measurements. Fig. 5.4 explains our single tone reconstruction result. Fig. 5.4.a shows phase shifted and time stretched optical pulses at an optical delay of 4ps. Electro-optically mixing this optical signal with single tone RF signal, the mixed signal is shown in Fig. 5.4.b. This optical output is acquired and digitally summed to represent single power measurement at a capture rate of 50MS/s. Hence each optical delay, 4 phase shifted measurements have been obtained. The process repeated for next step of optical delay of 0.5ps and is repeated 102 times. Vectorising the measurements as $msmt_0$ corresponding to -3V, $msmt_{\pi/2}$ corresponding to -1.5V, $msmt_{\pi}$ corresponding to 0V, $msmt_{3\pi/2}$ corresponding to +1.5V each of length 103 for 103 optical delay steps. The FFT of the unknown RF signal can be reconstructed with equation explained in [56]. The procedure has been explained in chapter 2. The frequency resolution is linearly proportional to delay step used in acquisition, dispersion $\ddot{\Psi}$ as determined in Eq. 5.2. The FFT obtained is shown in Fig. 5.4.c. showing the successful reconstruction of single 1GHz RF tone with a small error which is within 50MHz. The reconstructed tone in this case is 1.026GHz considering the adjustment of the offset. The absolute value of FFT optical power retrieves FFT magnitude spectrum of RF signal and is presented in Fig. 5.4.c along with calibration curve for this experiment to measure the RF frequency. Experimentally measured calibration is shown in blue and theoretically calculated curve is shown in blue. Time domain waveform can be reconstructed from IFFT of the obtained measurements. The result is represented in Fig. 5.4.d showing successful reconstruction after removing the noise floor in Fig. 5.4.c.

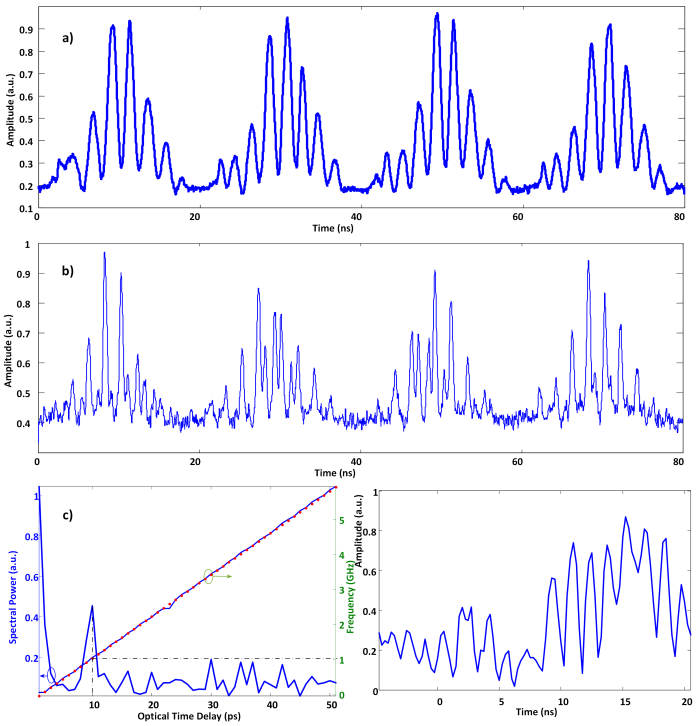

Fig. 5.4 Demonstration with single tone RF signal. a) Phase shifted and time stretched gaussian optical pulse carrier signal in time domain with 80ns duration at 4ps optical delay. b)Electro-optically mixed optical signal c)Fourier spectrum acquisition showing strong single tone at 9ps optical delay with calibration curve. Red line is the calculated while Blue line is experimental observation d) Time domain reconstruction of the acquired FFT

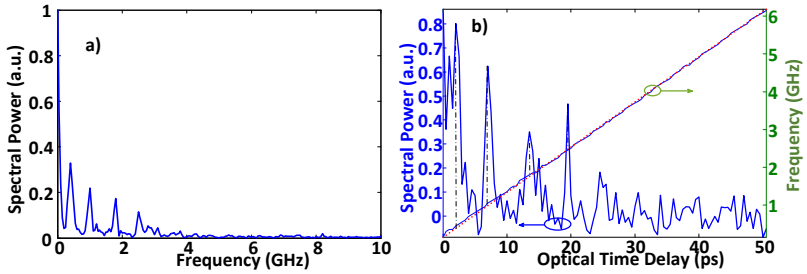

Fig. 5.5 Demonstration with multitone RF signal. a) Input RF spectrum. b) Reconstructed FFT spectrum. The experimental calibration line is shown in blue color while theoretical calculated line is shown in red color.

5.3.3 Multi tone reconstruction

In this demonstration, a multitone signal (0.4GHz, 1GHz, 1.8GHz and 2.5GHz) is considered to show the robustness of the proposed system and the input signal is shown in Fig. 5.5.a. Scanning with 0.5ps delay resolution from 0 to 50.5 ps, 408 measurements acquired. By vectorization and reconstruction, the reconstructed FFT is shown in Fig. 5.5.b. after adjusting the offset in the experiment calibration. The acquired FFT tones are 0.3891GHz, 0.9869GHz, 1.764GHz and 2.481GHz showing successful reconstruction of the tones.

5.4 Discussions

The aforementioned method senses information by entirely scanning the FFT through 4-phase shift method. However, if the region of interest is known or there has been prior information about the frequency distribution, the over all number of measurements can be reduced and the signal can be reconstructed faithfully. One such approach has been described below.

5.4.1 Dual tone reconstruction with non-uniform sampling

A dual tone signal 1GHz and 2.5GHz is reconstructed with the same method with 0.5ps optical delay resolution. The input signal FFT is shown in Fig. 5.6.a. and the reconstruction result is shown in Fig. 5.6.b. As observed, the low frequency Gaussian is not scanned is because of starting scanning RF frequency is 200MHz offset with respect to theoretical calculations shown in red line of 5.6.b. The proposed system can be demonstrated for anamorphic sampling the FFT of the signal by using high sampling density in the frequency interested region. Fig. 5.7.a. shows sparse uniform sampling of FFT with 3 ps optical delay resolution acquiring 68 power measurements resulting unsuccessful reconstruction as the scanning step misses the spectral distribution of the tones. With the same number of

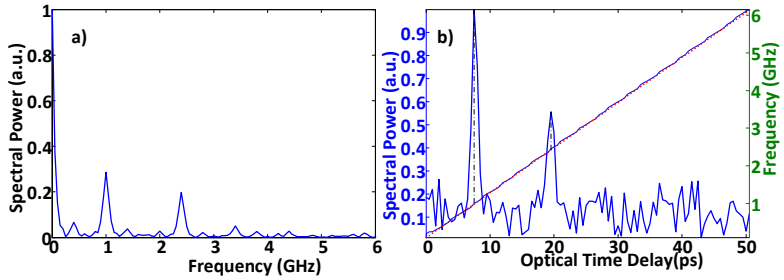

Fig. 5.6 Demonstration of dual tone reconstruction with 0.5ps resolution a) Original signal FFT representation b) reconstructed FFT with experimental calibration

measurements, the information rich region is over sampled as shown in Fig. 5.7.b in red color with 64 power measurements with successful reconstruction.

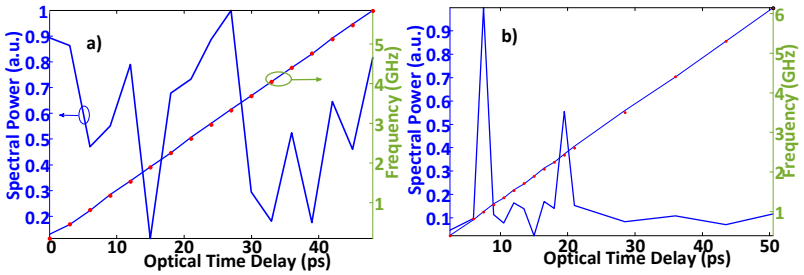

Fig. 5.7 Demonstration of anamorphic sampling of FFT. a) Unsuccessful FFT reconstruction by sparse uniform sampling with 3ps delay resolution with experiment calibration b) FFT reconstruction with anamorphic sampling with experiment calibration

The proposed method eliminates the use of electronic generators like AWG and enhances the frequency spectrum capability which scans upto 150 GHz if a commercial 1200ps optical delay line is used with careful calibration. However, the overall system capability is dependant on Mach-Zehnder modulator's commercial availability to sense the high frequency RF signals. As a proof of concept demonstration, a simulation result has been presented with schematic shown in Fig. 5.1 that senses a multitone(1GHz, 3.4GHz, 4.2GHz, 5GHz, 10.2GHz, 20.5GHz, 35.3GHz and 40.2GHz) RF signal as shown in Fig. 5.8.a. The corresponding FFT representation is given in Fig. 5.8.b. The MLL acts as passive ultrashort pulse generator with 20ns repetition time. The femtosecond pulses are time stretched with a dispersion compensating fibre of 0.96 ns/nm dispersion. The time stretched pulses are directed to an

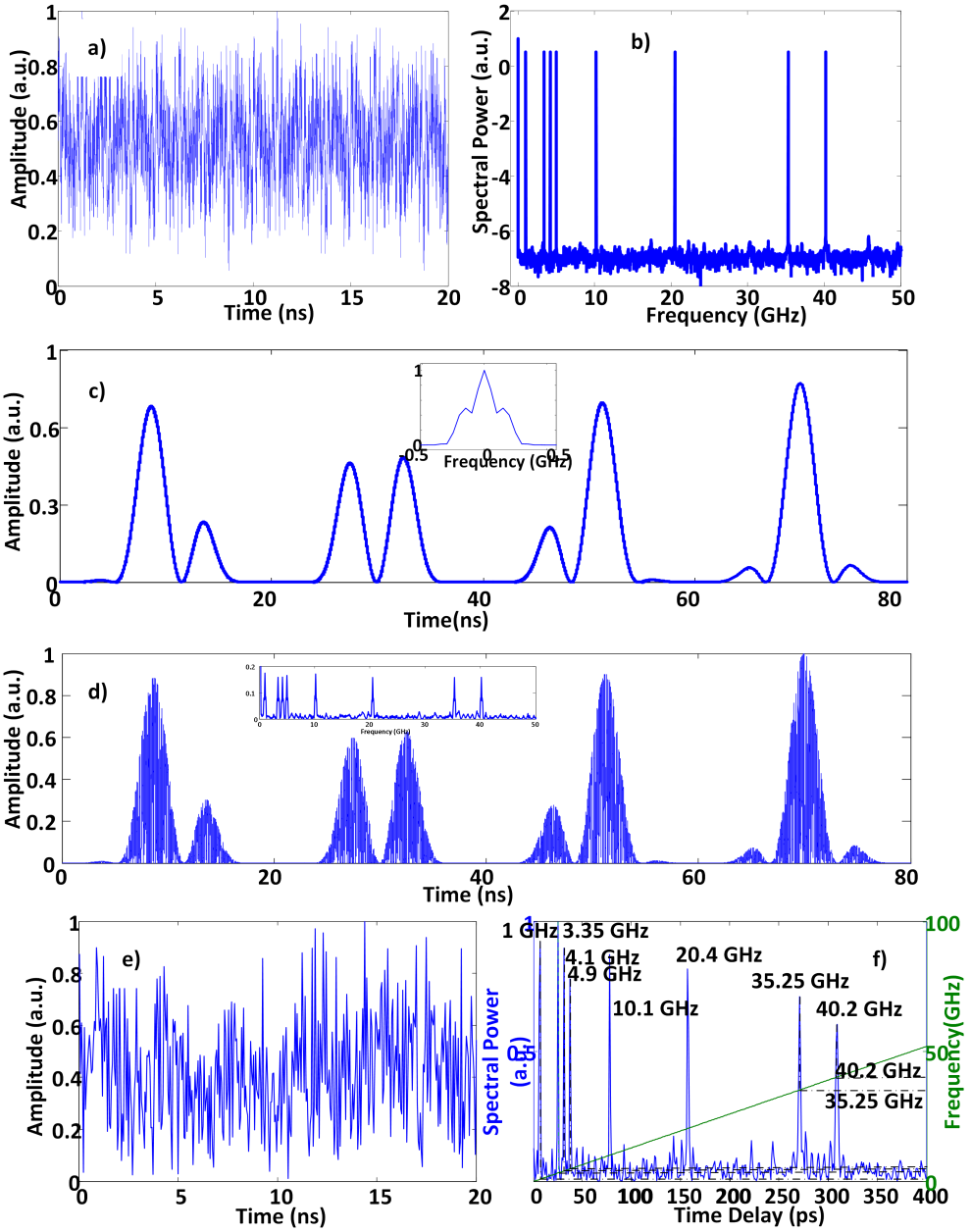

Fig. 5.8 Simulation results. a) Input multitoned RF signal with highest frequency 40.2GHz b) Corresponding FFT spectrum of signal c) Phase-shifted optical carrier. Inset shows RF magnitude spectrum d) Signal encoded phase-shifted optical carrier. Inset shows RF magnitude spectrum e) Reconstructed time domain signal from inverse transformation f) Reconstructed FFT spectrum with frequency shown in green color. Optical time delay is shown in X-axis.

MZI setup consisting of PM in one arm and optical delay line in another arm. The phase modulator is given a stair case input changing the phase from 0 , pi/2, pi, and 3 pi/2 with 80ns duration. The optical delay is varied from 1ps to 400ps in steps of 1ps. The phase shifted and phase stretched optical carrier is shown in 5.8.c. and corresponding electro-optically mixed signal is shown in 5.8.d. with their RF spectra shown in individual insets. The calibration curve is shown in Fig. 5.8.e in blue color while theoretically calculated calibration line is shown in red and the obtained FFT spectrum using Eq. 2.30. The corresponding time domain reconstruction is shown in Fig. 5.8.f. is obtained from IFFT of spectrum obtained.

5.5 Conclusion

A novel all-optical approach for spectrum sensing with Fourier spectrum acquisition has been proposed using Phase Modulator and optical delay line in interferometric manner followed by phase shifting, sensing and integration to sense the RF signals up to 3GHz experimentally and up to 40GHz with simulations without any need for high speed electronic RF generators. Reconstruction of single tone and multitoned signals have been presented. A new approach of anamorphic sampling[176] has been demonstrated using only selective range of basis scanning by tuning optical delay.

Chapter 6

Adaptive non-uniform photonic time stretch for high-speed signal detection for data compression

An AST Method that reduces TBP there by reducing the number of samples to be stored on the storage. This chapter continues the detailed version of AST explained in chapter 2 with the research work done in this thesis work in order to reduce the number of samples there by attaining data compression. This chapter is a revised version of a published paper[68].

As explained in section 2.1, the Anamorphic Stretch Transform technique is mainly used in optical domain in order to highly sample pre-known information rich region and coercive sample the remaining region mimicking the biological human eye. In this chapter, a method of compressing the data volume of high speed input RF signal without knowing the region of interest with compressed time band width product has been proposed and verified through numerical simulations. However, the method sacrifices the measurement speed at the benefit of rich sampling and data compression.

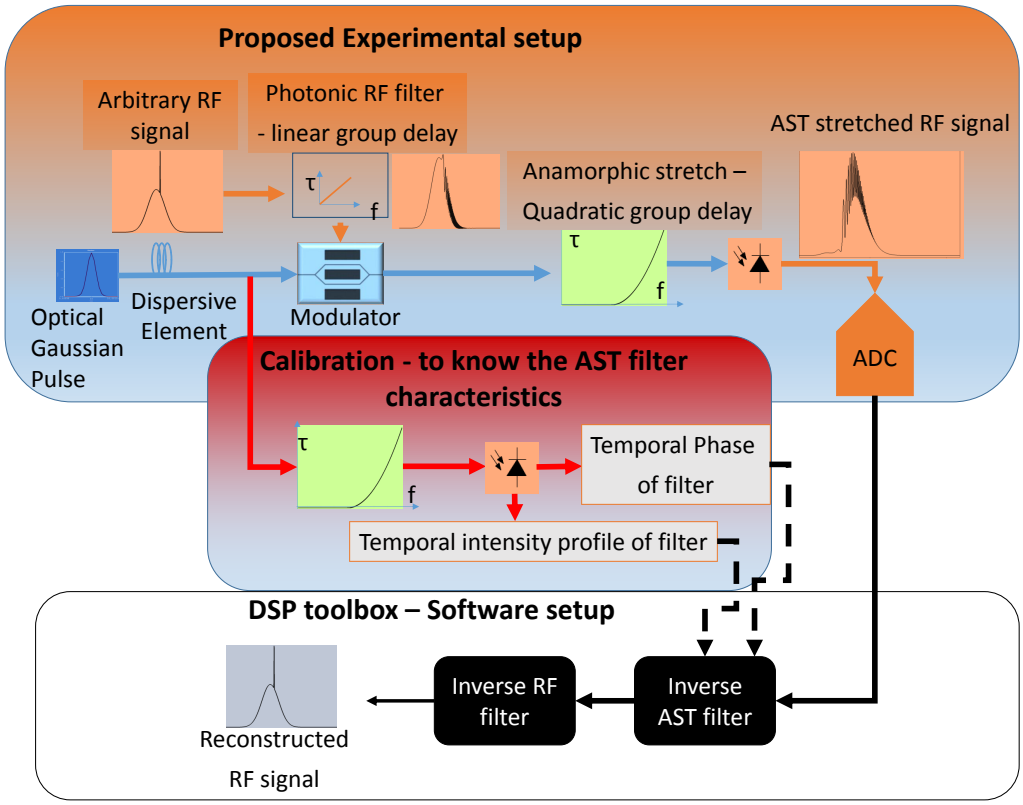

Fig. 6.1 Schematic diagram of the proposed and simulated adaptive non-uniform photonic time stretch system.

6.1 Principle

Schematic diagram of the proposed adaptive non-uniform photonic time stretch system for blind detection of arbitrary RF signals has been shown in Fig. 6.1. Optical pulses generated from a passively mode-locked laser were pre-stretched by a first dispersive element e.g., dispersion compensating fibre. The initially time stretched optical pulse serves as the quasi-continuous wave optical carrier. Different from previous PTS-ADC [103, 98, 104] and AST [38, 35, 40, 42] systems, in the proposed method the input RF signal is first pre-stretched by a microwave photonic phase filter with frequency-dependent time delay response using a quadratic phase function instead of conventional amplitude before direct modulation on the stretched optical carrier at an electro-optical modulator. Due to the large microwave dispersion introduced by the microwave photonic phase filter, the high frequency components of the unknown RF signal were separated from its low frequency elements in time, leading to a frequency-chirped RF signal with its spectral-temporal profile mainly determined by the microwave photonic phase filter. The transformed RF signal then modulates the optical carrier at the modulator. A second dispersive element, serving as the AST filter, further stretches the modulated optical pulse to slow down the high-speed part of the RF signal such that it can be captured using a lower-speed PD and electronic ADC reducing the TBP and number of samples representing the overall RF information. Low speed ADC collects few number of samples as per the Nyquist sampling theorem. To achieve this, the AST filter has a non-uniform group delay response such that particular part of the optical spectrum carrying high-frequency components (fine features) of the RF signal will be selectively stretched (slowed down) more than those carrying low-frequency RF elements. Therefore, TBP of the detected RF signal has been greatly reduced. Design of AST filter was usually signal-dependent in previous systems [38, 35, 40, 42]. As the time frequency distribution of the modulating RF signal is uniquely determined by the microwave photonic phase filter, the AST filter has been designed based on the time delay response of the microwave photonic

phase filter, which is independent of the RF information. Finally the non-uniformly stretched optical pulse, which carries the selectively slowed RF signal is detected by a low-speed PD with a reduced TBP. RF signal recovery is implemented in the digital domain or post processing after acquisition using electronic digitizers. Signal recovery algorithm consists of two steps: inverse AST processing and inverse RF phase filtering. Its important to note that a calibration need to be performed to note the phase and magnitude spectra of both AST and microwave photonic RF filters where an un-modulated optical pulse passes through the same AST filter, is included to remove the effect of Gaussian envelope of the optical carrier, as shown in Fig. 6.1.

6.2 Results

Numerical simulations have been implemented using a commercial simulation tool (VPIphotonics) to demonstrate the utility of the proposed approach in TBP-reduced blind detection of arbitrary RF signals. In the proposed system, an input RF signal under test is firstly pre-stretched by a microwave photonic phase filter, which provides deliberately designed nonlinear phase response corresponding to a frequency-dependent time delay, or microwave dispersion. The pre-stretched RF signal then modulates an optical carrier at a MZM, which has been biased at quadrature point to ensure linear intensity modulation. The optical carrier has been obtained by stretching ultrashort optical Gaussian pulses from a 50 MHz passive mode-locked laser with full-width at half-maxim (FWHM) pulse width of 800 fs using a first dispersive element with total group velocity dispersion (GVD) of -1050 ps/nm. An optical AST filter with deliberately designed non-linear time delay response then selectively slowed down the RF-encoded optical pulse to compress the TBP of the detected RF signal.

6.2.1 AST filter with quadratic time delay

As a proof-of-the-concept demonstration, a time-limited RF signal involving both high frequency features (a narrow Gaussian spike) and low frequency components (a slow Gaussian envelope with limited time duration) has been used as the input RF information signal under test, as shown in Fig. 6.2.a. Fig. 6.2.c shows the spectrogram of the input signal, from which it can be observed that most RF frequency components are confined within a narrow time window. The microwave photonic phase filter has been designed to provide quadratic

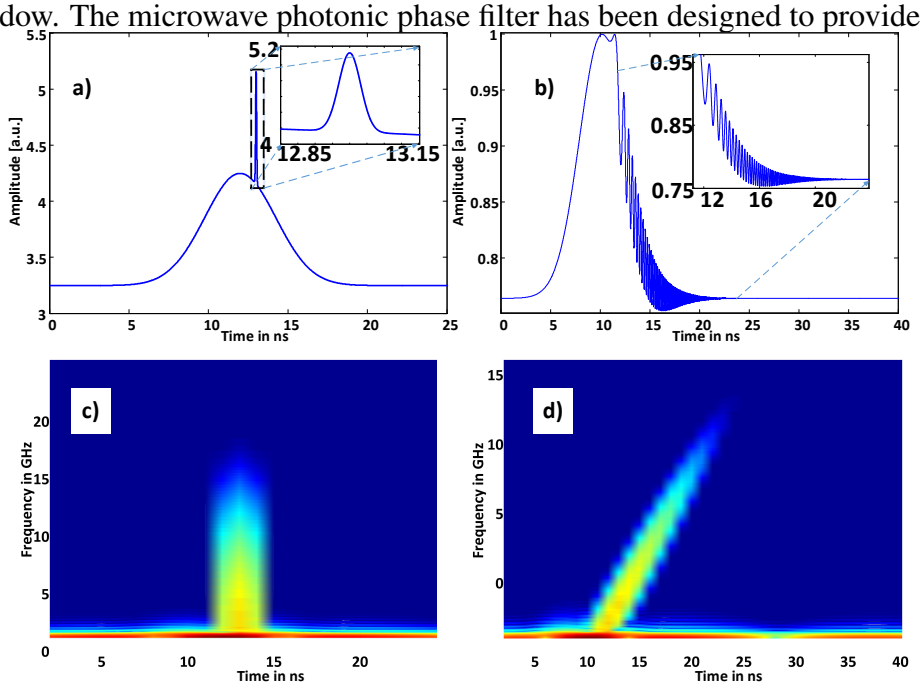

Fig. 6.2 Simulation results on the microwave photonic phase filtering. (a) The original input RF signal under test. (b) Stretched RF signal by the microwave photonic phase filter with a linear frequency-dependent time delay response. (c) Spectrogram of the original RF signal. (d) Spectrogram of the RF signal after microwave photonic filtering, showing a frequency chirp rate of 2 GHz/ns.

phase response corresponding to a linear frequency-dependent group delay of 2 GHz/ns. Despite that microwave photonic filters normally provide amplitude-only variation with linear phase response or constant microwave delay [18], microwave photonic phase filters with tunable highly nonlinear phase response, hence frequency-dependent group delay response up to several GHz/ns have been reported based on nonlinear optical chromatic dispersion

[177, 178] and successfully applied in chirped microwave waveform compression [179]. Enabled by microwave frequency-dependent time delay, the high frequency Gaussian spike in the original input RF signal is shifted with longer delay and stretched as per the designed chirp rate. As a result, the instantaneous frequency components of the transformed RF signal are separated in ascending order as shown in Fig. 6.2.b. Fig. 6.2.d presents the spectrogram of the RF signal after microwave photonic pre-stretching, clearly showing a frequency chirp rate of 2 GHz/ns. Therefore, significant microwave dispersion from the microwave photonic phase filter has transformed the input RF signal with unknown frequency profile to a linearly chirped microwave waveform with its spectral-temporal profile determined by the microwave photonic filter. Note that despite the increased TBP for the transformed chirped microwave signal due to pre-stretching, overall TBP compression will be achieved thanks to the following non-uniform optical time stretch at the designed AST filter. The pre-stretched RF signal then modulates an optical carrier at an MZM. The stretched optical pulse carrier also has a temporal Gaussian shape as shown in Fig. 6.3.a, which verifies the dispersion-induced wavelength-to-time mapping [180]. After intensity modulation at the MZM, the observed modulated optical pulse is shown in Fig. 6.3.b and the corresponding optical spectrum is shown in Fig. 6.3.c. By comparing the spectral and temporal representations of the modulated optical pulse, a linear relationship between time and frequency is obtained as shown in Fig. 6.3.d and can be represented in the form of equation as shown in equation 6.1 where c is velocity of light, D is the dispersion of the dispersive element used in ps/nm/km, L is length of dispersive element in km, f_c is the central optical frequency which is 193.55 THz mapped to time instant t_c.

$$t - t_c = \left(\frac{c.D.L}{f_c^2}\right) \times (f - f_c) \tag{6.1}$$

Thanks to this one-to-one mapping, it can be observed that the RF signal is encoded onto the optical spectrum of the pulse carrier. To achieve the desired TBP compression through non-

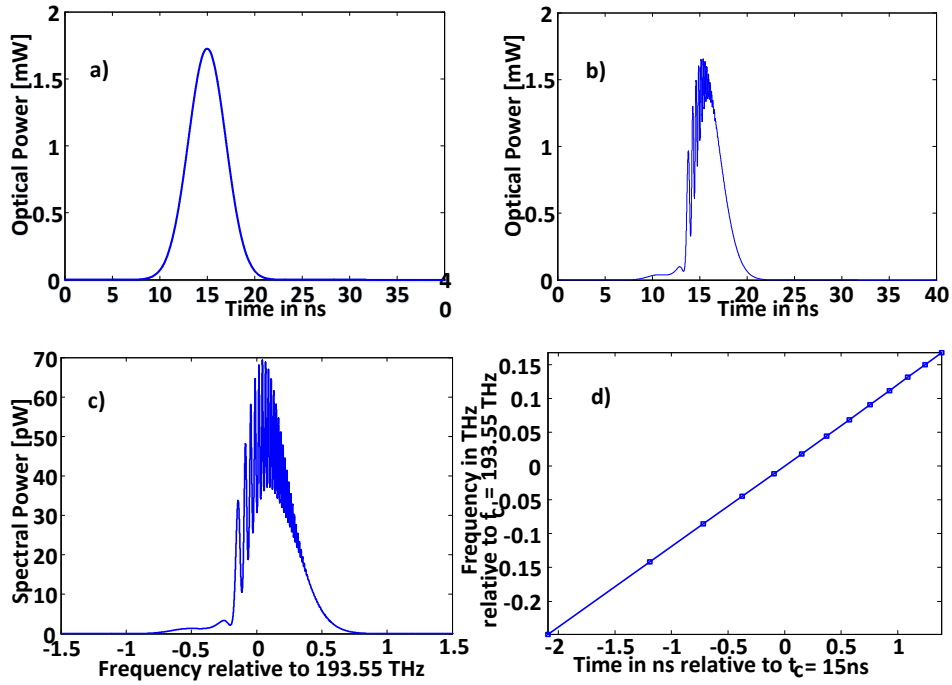

Fig. 6.3 (a) Time stretched optical pulse by the first dispersive element. (b) Optical pulse modulated with the pre-stretched RF signal. (c) Corresponding optical spectrum verifying that the RF signal is also encoded in to spectral domain. (d) One-to-one mapping between time and frequency according to (b) and (c).

uniform optical time stretch, an AST filter providing quadratic time delay is first designed according to the quadratic phase response of the microwave photonic filter. The group delay response of the AST filter is given by

$$\Delta\tau(f) = K_1 \times (f - f_0)^2 \tag{6.2}$$

where f is the instantaneous optical frequency, f_0 denotes the central optical frequency with zero time delay, and K_1 is the second-order dispersion coefficient of the AST, which has been determined by the chirp rate of the microwave photonic phase filter. The time delay characteristics of the designed AST filter is shown in Fig. 6.4.a. The central frequency f_0 is carefully selected such that the whole optical pulse spectrum falls in the frequency region $f > f_0$. Therefore, higher optical frequency components of the modulated optical

pulse, which also carry higher RF frequency information, will experience higher chromatic dispersion and hence being stretched more than those carrying lower RF frequency. As a result, the modulated optical pulse is selectively stretched due to nonuniform dispersion in the AST filter and TBP of the resulting signal can be greatly compressed. Fig. 6.4.b shows the non-uniformly stretched optical pulse by the AST filter. The selectively stretched RF signal is detected using a highspeed PD and its spectrogram is shown in Fig. 6.4.d. It can be observed that RF frequency chirp becomes nonlinear and higher frequency components have been stretched more compared to lower frequency parts. TBP of the captured RF signal is reduced in our proposed system. Table 6.1 summaries TBP of the original RF signal (1) and the non-uniformly stretched signal in our proposed system. It can be observed that TBP value has been reduced by 28%, corresponding to a compression ratio of 72%. Reconstruction of the original RF signal from the captured stretched RF signal is implemented in digital domain following two steps: (1) inverse AST processing, which recoveries the pre-stretched RF signal before AST stretching; (2) inverse RF phase filtering, which transforms the pre-stretched RF signal back to the original one according to the microwave photonics filter response. Note that a small portion of pre-stretched optical pulse bypasses MZM but goes through the same AST filter to allow an optical calibration process, which removes the effect of Gaussian envelope of the optical carrier. The reconstructed RF signal is shown in Fig. 6.4.c. Compared to the signal as shown in Fig. 6.2.a, a good match with the original RF signal has been clearly evidenced. To demonstrate that the proposed approach is valid for different RF signals with unknown instantaneous frequency profile, a second RF signal 2 with high frequency information occurring at different position is selected as the original input signal, as shown in Fig. 6.5.a. Fig. 6.5.b shows the pre-stretched RF signal by the same microwave photonic phase filter with a chirp rate of 2 GHz/ns. Fig. 6.5.c and d. present the corresponding spectrograms for the original and filtered RF signals respectively. The recovery results for the second RF signal are shown in Fig. 6.6.

Table 6.1 TBP Reduction for two different RF signals using AST filter with quadratic time delay

Parameters	Original RF signal	Stretched RF signal	Original RF signal 2	Stretched RF signal 2
Time Duration	25 ns	45 ns	25 ns	40 ns
Max. Frequency	15 GHz	6 GHz	15 GHz	7 GHz
TBP	375	270	375	280

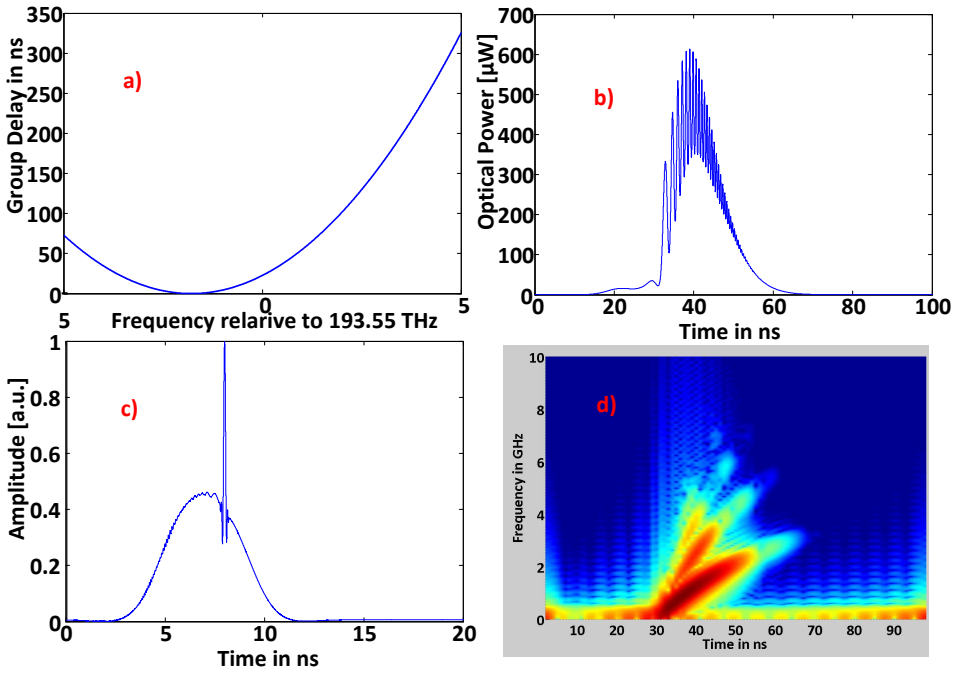

Fig. 6.4 (a) The time delay function of the designed AST filter with quadratic group delay. (b) Non-uniformly stretched optical pulse by the AST filter. (c) The reconstructed RF signal following the signal recovery algorithm implemented in digital domain. (d) Spectrogram of AST stretched optical pulse after photo-detection showing the non-uniform photonic time stretch

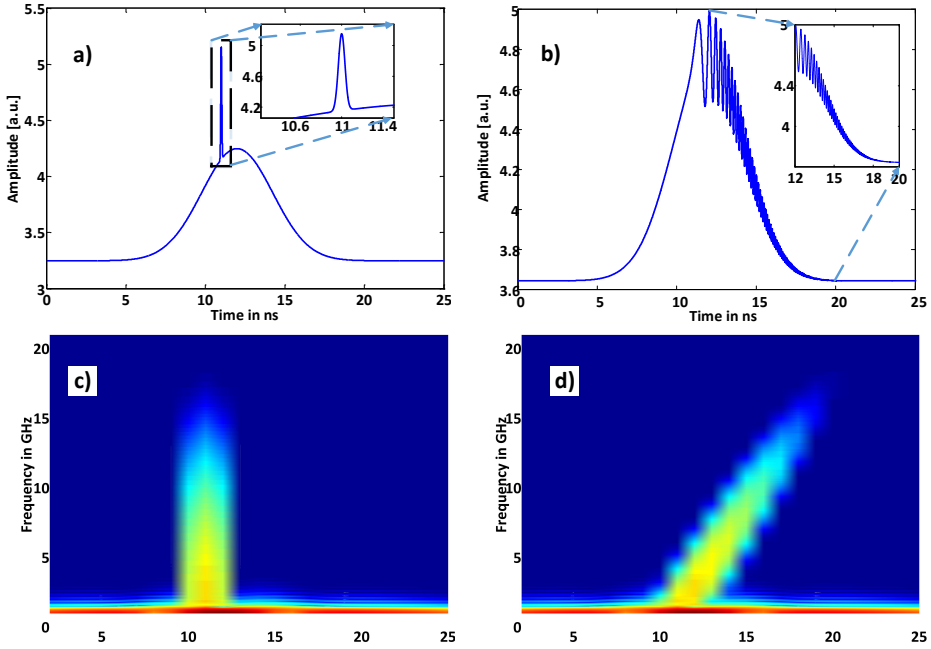

Fig. 6.5 (a) A second RF signal under test. (b) Pre-stretched RF signal by the same microwave photonic phase filter with linear frequency-dependent time delay response. (c) Spectrogram of the original RF signal. (d) Spectrogram of the pre-stretched RF signal by the microwave photonic phase filter

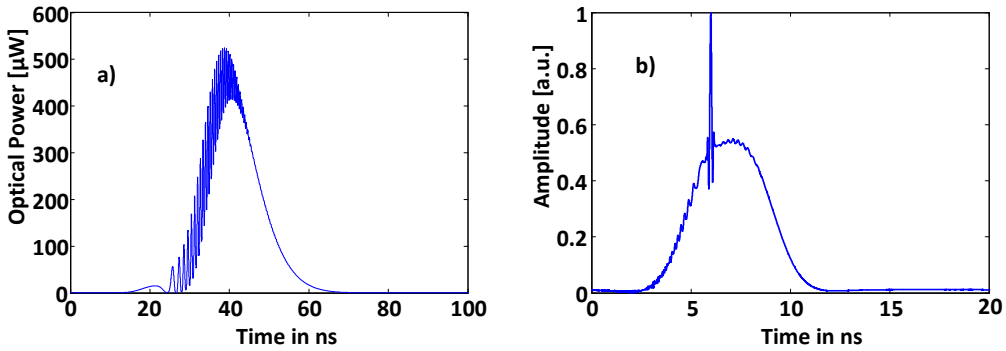

Fig. 6.6 (a) Modulated optical pulse carrier after non-uniform stretching at the AST filter. (b) The reconstructed RF signal after digital signal recovery

The reconstructed RF signal matches well with the original signal as shown in Fig. 6.5.a. Characteristics of non-uniform time stretch for the second RF signal are also summarized in Table 6.1, and TBP reduction by 25% has been achieved. It has been verified that the proposed method works for time-limited RF signals with different spectra-temporal profiles.

6.2.2 AST filter with cubic time delay

To explore the capability of the proposed approach for better TBP reduction in high-frequency RF signal detection, a second AST filter providing cubic time delay response has been designed. The group delay response of the AST filter is given by

$$\Delta\tau(f) = K_2 \times (f - f_0)^3 \tag{6.3}$$

where K_2 is the third-order dispersion coefficient of the AST filter, which can be determined by the chirp rate of the microwave photonic phase filter. The characteristic of the designed AST filter is shown in Fig. 6.7.a. The central frequency is selected such that the whole pulse spectrum falls in the region $f > f_0$. The RF signal 1 as shown in Fig. 6.2.a is used again as the original input signal. Fig. 6.7.b presents the modulated optical pulse carrying the transformed RF signal after being non-uniformly stretched by the AST filter with cubic time delay response. Its spectrogram is shown in Fig. 6.7.d. It can be observed that RF frequency chirp becomes nonlinear and higher frequency components have been stretched more compared to lower frequency parts. Due to the large nonlinear time delay produced by the AST filter, the resulting non-uniformly stretched optical pulse has a longer time duration (140 ns). At the same time, the maximum RF frequency carried by the stretched optical pulse has been reduced to 1.5 GHz. Therefore, the overall effect is that TBP of the captured RF signal is reduced in our proposed system thanks to the highly nonlinear time delay at the AST filter. Table 6.2 summaries the TBP of the original RF signal and the corresponding

non-uniformly stretched signal in the case of an AST filter with cubic time delay response. It can be observed that TBP value has been reduced by 44%. Reconstruction of the original RF signal is implemented in digital domain following the two abovementioned steps, with the result shown in Fig. 6.7.c, which matches well with the original RF signal as shown in Fig. 6.2.a. The AST filter with cubic time delay is also tested with a different input RF signal 2 as shown in Fig. 6.5.a to demonstrate that the proposed system is independent of the instantaneous frequency profile of the input RF signals. The same microwave photonic phase filter with a chirp rate of 2 GHz/ns is used to pre-stretch the input RF signal before modulating the

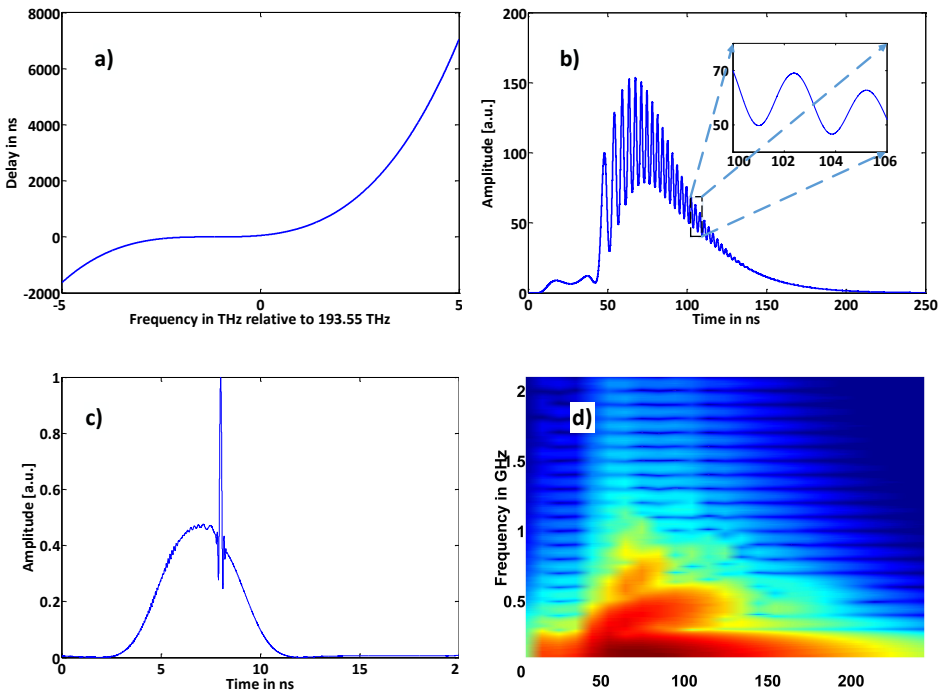

Fig. 6.7 (a) Time delay as a function of optical frequency in the AST filter with cubic group delay response. (b) Non-uniformly stretched optical pulse carrying RF signal by the AST filter. (c) The reconstructed RF signal following the signal recovery algorithm implemented in digital domain. (d) Spectrogram of non-uniformly stretched optical pulse confirming TBP reduction of the captured RF signal.

optical carrier. Fig. 6.8.a shows the modulated optical pulse after nonuniform stretching at the AST filter. It can be observed that the high frequency components have been stretched

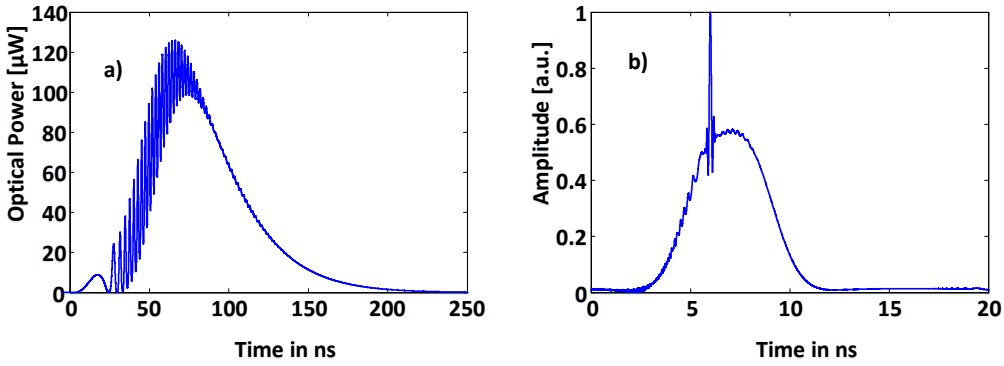

Fig. 6.8 (a) Modulated optical pulse after non-uniform stretching with the AST filter with cubic time delay. (b) The recovered RF signal 2 after digital signal processing

Table 6.2 TBP Reduction for the first RF signals using an AST filter with cubic time delay

Parameters	Original RF signal	Stretched RF signal
Time Duration	25 ns	140 ns
Max. Frequency	15 GHz	1.5 GHz
TBP	375	210

further, evidenced by TBP reduction of 44%. The recovery result for the second RF signal is shown in Fig. 6.8.b. It can be seen that the proposed method works for RF signals with different time-frequency distributions.

6.2.3 Discussions

The utility of the proposed adaptive approach in RF signal detection with reduced TBP has been demonstrated using numerical simulations which can guide in implementing the actual filters in experiments such as frequency dependant time delay filter and AST filter. The simulations have verified that if the filters are calibrated to record the phase profiles, the information can be reconstructed with high probability of capturing high frequency information or transient events in the signal.The most important element in the system is the microwave photonic phase filter with frequency dependent time delay, which transforms the spectra-temporal profile of the RF signal. The designed microwave photonic phase filter can be implemented based on nonlinear optical chromatic dispersion [177, 178], optical delay to microwave delay conversion [179], and non-uniformly spaced delay-line filter [181]. A second key element in the proposed system is the AST filter. Despite extensive theoretical and simulation studies on the AST approach including this work, quite little experimental study on this topic has been reported so far, mainly due to the lack of good optical filter offering an engineered group delay or dispersion profile. Potential good candidates to achieve the particularly designed AST filter include customized fibre Bragg gratings [40, 182, 183], chromo-modal dispersion mechanism [184] with the aid of mode-selective excitation [185], and photonic crystal fibre (PCF) with precisely controlled chromatic dispersion profile [84]. In the presented demonstrations, only time-limited RF signals have been tested using the proposed method. This is due to the limited time aperture of the photonic time stretch system, which is the reciprocal of the pulse repetition rate. Passively mode-locked laser has

a repetition rate in the order of 10 MHz, corresponding to a time aperture of 100 ns, which would suffice for many high-frequency RF signals.

6.3 Conclusion

Non-uniform photonic time stretch enables TBP reduction in high-speed RF signal detection by selectively stretching the RF spectrum of interest. However, prior knowledge of the spectral-temporal profile of the RF signal is always needed. In this chapter, a new adaptive photonic time stretch scheme by pre-chirping the input RF signal using a microwave photonic phase shift is proposed to overcome this limitation. Using the proposed approach, blind detection of RF signals with different spectra-temporal profiles have been demonstrated. TBP compression ratios of 72% and 56% have been achieved using non-uniform time stretch filters with quadratic and cubic time delays respectively. The proposed adaptive photonic time-stretch system works without the knowledge of the unknown RF signals, hence providing a more promising solution for real-time detection of arbitrary RF signal with reduced TBP. The concept developed can be adapted to address data compression issues in wider fields such as high-speed communications, ultrafast measurement and massive sensor network.

Chapter 7

Summary and Future Work

7.1 Summary

This thesis mainly focussed on optical techniques to boost the capturing capability of ultrafast measurement systems by exploring signal processing techniques such as anamorphic stretch transform, compressed sensing and fourier spectrum sensing in optical domain.

The Photonic compressed sensing, a sub-nyquist sampling technique to sense sparse signals in optical domain has been explored for Optical Coherence Tomography for Bio-Medical applications and distributed strain sensing for industrial applications. The numerical and experimental results have been presented in this thesis. First, Time Domain Photonic Compressed Sensing system has been demonstrated with electrically generated binary random patterns. The advantages with this method is that, (1) Data compression (2) Reduced the high speed requirement of electronic detection systems. However, there have been limitations such as, (1) High speed electronic random pattern generator requirement to enable time domain compressed sensing (2) Usage of electro-optic effect which some extent is lossy and may require amplifier for faithful detection (3) Electrical bandwidth of pulsed source compromises data compression (4) Huge physical size of electronic generator.

To reduce these limitations, electrically generated binary PRBS sequences are replaced with all-optical analog random patterns generated from cascaded Mach-Zehnder Interferometric configuration utilizing dispersion in single mode fibres and optical delay lines in opposite chirp configurations. This has been referred as Spectral Domain Photonic Compressed Sensing system based on cascaded MZI. The method has been applied for blind RF spectrum sensing and FBG sensing. This method have several advantages such as, (1) Data compression (2) Reduced the high speed requirement of electronic detection systems (3) Reducing the need for high speed electronic random pattern generator (4) Avoided usage of electro-optic conversion followed by amplification, hence improved the energy efficiency (5) Reduced the effect of Electrical bandwidth of optical pulse on data compression (6) The physical size of overall system has been reduced as there is no electronic high speed equipment involved. However, this method has a few limitations such as, (1) Sensitivity to environment issues such as polarization, disturbance to interferometric structure (2) Periodic calibration for random patterns is essential with high speed equipment once before capturing actual measurements.

The research on generating 2D optical speckle patterns caused by wavelength dependant chaos inside multimode fibre structure has been discussed and for a set of 500 wavelengths, uncorrelated patterns have been generated and successful reconstruction of a 2D image with compressed sensing has been presented.

The thesis presented experimental investigation of Fourier spectrum sensing with all-fibre interferometric time stretched harmonic sinusoidal patterns with optical delay line and electro-optic phase modulator. The RF spectrum has been scanned non-linearly with tunable optical delay and the successful reconstruction of single tone and multi-toned RF signals have been presented.

Microwave group delay filter followed by Dispersive Fourier Transform has been utilized for mapping the RF frequency spectrum to optical spectrum. Anamorphic stretch

transform(AST) has been processed to stretch the high frequency information to bring the overall information signal into the bandwidth limit of electronic sensing equipment. Two types of AST filters, quadrautic and cubic group delay filters have been investigated and TBP compression has been achieved.

In conclusion, various enhancement techniques have been presented for measurement systems utilizing photonic time stretch as main tool. Different compression schemes have been studied and enhancement techniques have been presented with numerical and experimental demonstrations for various application fields such as bio-medical imaging and distributed FBG sensing, microwave spectrum sensing. A tabular summary has been presented with various parameters as per this thesis work in Fig. 7.1.

Parameters specific to this thesis work	Time domain Photonic Compressed Sensing(chap:3.1)	Spectral domain Photonic Compressed Sensing(chap:3.2)	Spatial domain Photonic Compressed Sensing for High speed Imaging(chap:4)	All-optical FFT scanning for blind spectrum sensing(chap:5)	AST(chap:6)
Type of investigation	Experimental	Experimental	Simulation and experimental	Experimental	Simulation
Type of information	1D	1D	2D	1D	1D
Dependancy on electronics	Low speed detector/digitizer , high speed frontend AWG,EOM	Low speed detector/digitizer, No frontend	High speed electronic detector, No frontend	Low speed detector, Very Low speed frontend, EOM	Low speed Digitizers; High speed frontend modulator
Dependancy on Information	Should be sparse	Should be sparse	Naturally sparse	Not required; User selective	High
Measurement speed	1.51MHz	Few 10's Hz	50MHz	Few 10's Hz	Few MHz
Compression ratio	m/N – 50-70%	m/N – 10%	m/N – 66%	4m/N User selective	Information dependant
Post-processing time	High	Low	Very High	Very Low	Low
Calibration	May not be required as PRBS is binary and electronically generated	Required	Required	Required	Required twice for AST filter and RF filter
Environmental issues sensitivity	Low	High	High	High	Simulation
Loss	High; Electro-optic modulator	Very Low	Medium	Low	Simulated
Accuracy	The information spectrum is always associated with gaussian distribution due to the nature of optical carrier				

Fig. 7.1 Summary of thesis work

7.2 Outlook

The current thesis work can be extended further as follows.

7.2.1 Future work based on AST system proposed in this thesis:

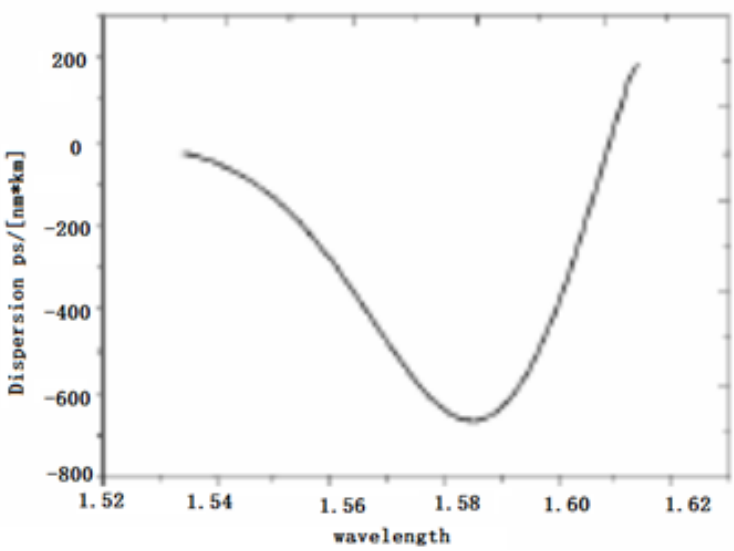

Fig. 7.2 AST quad filter using Photonic Crystal Fibre

The AST filter proposed and explained in chapter 6, can be extended and demonstrated with Photonic Crystal Fibre which has non-linear dispersion curve w.r.t. wavelength.

7.2.2 Future work for SD-PCS system based on cascaded MZI proposed in this thesis:

Spectral domain photonic compressed sensing based on cascaded MZI structure has low electronic bottleneck with low loss and RF blind spectral sensing has been demonstrated in chapter 3. This can be extended to imaging, Strain sensing or OCT volumetric scanning. The proposed schematic of spectral domain photonic compressed sensing based Michelson interferometry OCT system has been presented in Fig. 7.3

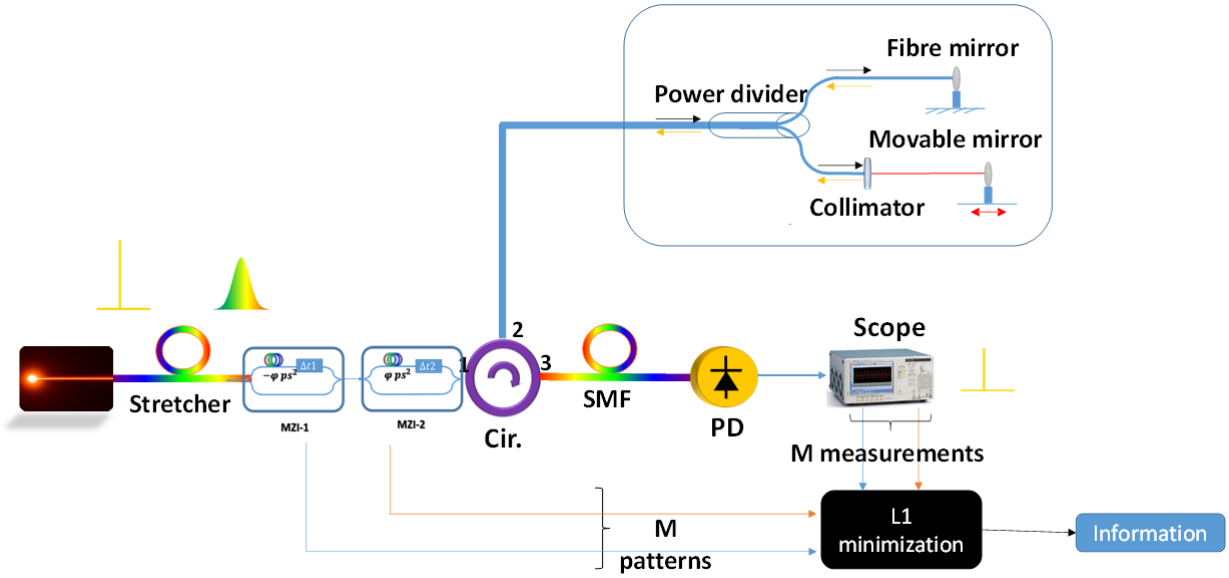

Fig. 7.3 Proposed spectral domain photonic time stretch compressed sensing based OCT system that can sense the A-scan profile of sample

7.2.3 Future work for UF-PCS imaging system

High speed compressed imaging based on multimode interference enables us to continuously sample images at 50MHz rate which can be used for video rate imaging for microscopy and flow-cytometry based applications. A proof-of-concept demonstration is presented in chapter 4. However, the computer interface units for realtime data acquisition, post-processing and streaming of images can be further investigated.

7.2.4 Potential future work for compressed sensing

Each of the frequency band of EM spectrum can be used for imaging. Microwave imaging has been explored to find hidden objects[186]. Using compressed sensing, the objects can be sensed with low speed detectors. Recently in-fibre diffraction has been demonstrated as an alternative for the free-space diffraction grating structure. Photonic information processing is an emerging area which has been used for forecast systems, reducing non-linear distortions in communication channel, pattern recognition. Determining a 2D image based on neural networks can be a complex idea but has big prospects such as automated cell labelling and detection.

As explained in chapter 1, the compactness or physical size of measurement system can be reduced with Photonic Integrated Circuits(PIC). The advantages with PIC include, reduction to the sensitivity to environment issues, improving operational stability, reduced size and low power consumption[20]. The proposed work can be integrated to PIC to envision compact ultrafast measurement systems.

References

[1] A. J. Seeds, "Microwave photonics," *IEEE Transactions on Microwave Theory and Techniques*, vol. 50, no. 3, pp. 877–887, 2002.

[2] A. J. Seeds and K. J. Williams, "Microwave Photonics," *Journal of Lightwave Technology*, vol. 24, no. 12, pp. 4628–4641, 2006.

[3] J. Capmany and D. Novak, "Microwave photonics combines two worlds," *Nat Photon*, vol. 1, pp. 319–330, jun 2007.

[4] J. Yao, "Microwave Photonics," vol. 27, no. 3, pp. 314–335, 2009.

[5] X. Zou, W. Bai, W. Chen, P. Li, B. Lu, G. Yu, W. Pan, B. Luo, L. Yan, and L. Shao, "Microwave photonics for featured applications in high-speed railways: Communications, detection, and sensing," *Journal of Lightwave Technology*, vol. 36, pp. 4337–4346, Oct 2018.

[6] A. Kanno, P. T. Dat, N. Sekine, I. Hosako, N. Yamamoto, Y. Yoshida, K.-I. Kitayama, and T. Kawanishi, "Seamless Fiber-Wireless Bridge in the Millimeter- and Terahertz-Wave Bands," *J. Lightwave Technol.*, vol. 34, pp. 4794–4801, oct 2016.

[7] T. Nagatsuma, S. Hisatake, M. Fujita, H. H. N. Pham, K. Tsuruda, S. Kuwano, and J. Terada, "Millimeter-Wave and Terahertz-Wave Applications Enabled by Photonics," *IEEE Journal of Quantum Electronics*, vol. 52, no. 1, pp. 1–12, 2016.

[8] H. Shams and A. Seeds, "Photonics, Fiber and THz Wireless Communication," *Opt. Photon. News*, vol. 28, no. 3, pp. 24–31, 2017.

[9] F. Zhang, Q. Guo, and S. Pan, "Photonics-based real-time ultra-high-range-resolution radar with broadband signal generation and processing," *Scientific Reports*, vol. 7, no. 1, p. 13848, 2017.

[10] F. Zhang, Q. Guo, Z. Wang, P. Zhou, G. Zhang, J. Sun, and S. Pan, "Photonics-based broadband radar for high-resolution and real-time inverse synthetic aperture imaging," *Opt. Express*, vol. 25, pp. 16274–16281, jul 2017.

[11] Z. G. Tegegne, C. Decroze, P. D. Bin, T. Fromenteze, and C. Aupetit-Berthelemot, "Single Channel Microwave Photonics Digital Beamforming Radar Imaging System," *J. Lightwave Technol.*, vol. 36, pp. 675–681, feb 2018.

[12] A. G. PODOLEANU, "Optical coherence tomography," *Journal of Microscopy*, vol. 247, no. 3, pp. 209–219, 2012.

[13] J. Benítez, M. Bolea, and J. Mora, "High-Performance Low Coherence Interferometry Using SSB Modulation," *IEEE Photonics Technology Letters*, vol. 29, no. 1, pp. 90–93, 2017.

[14] K. Goda, A. Fard, O. Malik, G. Fu, A. Quach, and B. Jalali, "High-throughput optical coherence tomography at 800 nm," *Opt. Express*, vol. 20, pp. 19612–19617, aug 2012.

[15] T. Klein and R. Huber, "High-speed OCT light sources and systems [Invited]," *Biomedical Optics Express*, vol. 8, no. 2, pp. 828–859, 2017.

[16] C. Wang, "Dispersive fourier transformation for versatile microwave photonics applications," in *Photonics*, vol. 1, pp. 586–612, Multidisciplinary Digital Publishing Institute, 2014.

[17] Y. Tong, Q. Zhou, D. Han, B. Li, W. Xie, Z. Liu, J. Qin, X. Wang, Y. Dong, and W. Hu, "Photonic generation of phase-stable and wideband chirped microwave signals based on phase-locked dual optical frequency combs," *Optics Letters*, vol. 41, no. 16, pp. 3787–3790, 2016.

[18] J. Capmany, B. Ortega, and D. Pastor, "A tutorial on microwave photonic filters," *Journal of Lightwave Technology*, vol. 24, no. 1, pp. 201–229, 2006.

[19] J. Yao, "Photonics to the Rescue: A Fresh Look at Microwave Photonic Filters," vol. 16, no. 8, pp. 46–60, 2015.

[20] X. Zou, B. Lu, W. Pan, L. Yan, A. Stöhr, and J. Yao, "Photonics for microwave measurements," *Laser & Photonics Reviews*, vol. 10, no. 5, pp. 711–734.

[21] R. A. Minasian, "Ultra-wideband and adaptive photonic signal processing of microwave signals," *IEEE Journal of Quantum Electronics*, vol. 52, no. 1, pp. 1–13, 2016.

[22] H. A. Haus, "Mode-locking of lasers," *IEEE Journal of Selected Topics in Quantum Electronics*, vol. 6, no. 6, pp. 1173–1185, 2000.

[23] R. R. Alfano, *The supercontinuum laser source*. Springer, 1989.

[24] Z. Zhu, H. Chi, T. Jin, S. Zheng, X. Yu, X. Jin, and X. Zhang, "Photonics-enabled compressive sensing with spectral encoding using an incoherent broadband source," *Opt. Lett.*, vol. 43, pp. 330–333, jan 2018.

[25] H. Chen, C. Lei, F. Xing, Z. Weng, M. Chen, S. Yang, and S. Xie, "Multiwavelength time-stretch imaging system," *Opt. Lett.*, vol. 39, pp. 2202–2205, apr 2014.

[26] Q. Guo, H. Chen, Z. Weng, M. Chen, S. Yang, and S. Xie, "Fast time-lens-based line-scan single-pixel camera with multi-wavelength source," *Biomedical Optics Express*, vol. 6, no. 9, pp. 3610–3617, 2015.

[27] B. Jalali, A. Mahjoubfar, and C. L. Chen, "Deep Learning Smart Microscope," in *Conference on Lasers and Electro-Optics*, p. STh3L.1, Optical Society of America, 2018.

[28] E. J. Ahmad, C. Wang, D. Feng, Z. Yan, and L. Zhang, "High Temporal and Spatial Resolution Distributed Fiber Bragg Grating Sensors Using Time-Stretch Frequency-Domain Reflectometry," *Journal of Lightwave Technology*, vol. 35, no. 16, pp. 3289–3295, 2017.

[29] G. Wang, Z. Yan, L. Yang, L. Zhang, and C. Wang, "Improved Resolution Optical Time Stretch Imaging Based on High Efficiency In-Fiber Diffraction," *Scientific Reports*, vol. 8, no. 1, p. 600, 2018.

[30] H. R. Petty, "Spatiotemporal chemical dynamics in living cells: From information trafficking to cell physiology," *Biosystems*, vol. 83, no. 2, pp. 217 – 224, 2006. 5th International Conference on Systems Biology.

[31] K. Goda, K. K. Tsia, and B. Jalali, "Serial time-encoded amplified imaging for real-time observation of fast dynamic phenomena," *Nature*, vol. 458, pp. 1145–1149, apr 2009.

[32] J. Liang and L. V. Wang, "Single-shot ultrafast optical imaging," *Optica*, vol. 5, pp. 1113–1127, sep 2018.

[33] K. Wang, A. Nirmalathas, C. Lim, E. Wong, K. Alameh, H. Li, and E. Skafidas, "High-speed indoor optical wireless communication system employing a silicon integrated photonic circuit," *Opt. Lett.*, vol. 43, pp. 3132–3135, Jul 2018.

[34] K. Goda and B. Jalali, "Dispersive Fourier transformation for fast continuous single-shot measurements," *Nat Photon*, vol. 7, pp. 102–112, feb 2013.

[35] B. Jalali and M. H. Asghari, "The Anamorphic Stretch Transform: Putting the Squeeze on Big Data," *Optics and Photonics News*, vol. 25, no. 2, pp. 24–31, 2014.

[36] J. Romberg, "Imaging via compressive sampling," *IEEE Signal Processing Magazine*, vol. 25, pp. 14–20, March 2008.

[37] E. J. Candes and M. B. Wakin, "An Introduction To Compressive Sampling," vol. 25, no. 2, pp. 21–30, 2008.

[38] M. H. Asghari and B. Jalali, "Anamorphic transformation and its application to time-bandwidth compression," *Appl. Opt.*, vol. 52, pp. 6735–6743, sep 2013.

[39] B. Jalali, J. Chan, and M. H. Asghari, "Time-bandwidth engineering," *Optica*, vol. 1, pp. 23–31, jul 2014.

[40] M. H. Asghari and B. Jalali, "Experimental demonstration of optical real-time data compression," *Applied Physics Letters*, vol. 104, no. 11, p. 111101, 2014.

[41] J. Chan, A. Mahjoubfar, M. Asghari, and B. Jalali, "Reconstruction in time-bandwidth compression systems," *Applied Physics Letters*, vol. 105, no. 22, p. 221105, 2014.

[42] A. Mahjoubfar, C. L. Chen, and B. Jalali, "Design of Warped Stretch Transform," vol. 5, p. 17148, nov 2015.

[43] C. L. Chen, A. Mahjoubfar, and B. Jalali, "Optical data compression in time stretch imaging," *PLOS ONE*, vol. 10, pp. 1–11, 04 2015.

[44] M. F. Duarte, M. A. Davenport, D. Takhar, J. N. Laska, T. Sun, K. F. Kelly, and R. G. Baraniuk, "Single-pixel imaging via compressive sampling," vol. 25, no. 2, pp. 83–91, 2008.

[45] D. L. Donoho, "Compressed sensing," *IEEE Transactions on information theory*, vol. 52, no. 4, pp. 1289–1306, 2006.

[46] J. A. Tropp, J. N. Laska, M. F. Duarte, J. K. Romberg, and R. G. Baraniuk, "Beyond nyquist: Efficient sampling of sparse bandlimited signals," *IEEE Transactions on Information Theory*, vol. 56, no. 1, pp. 520–544, 2010.

[47] R. G. Baraniuk, "Compressive sensing [lecture notes]," *IEEE Signal Processing Magazine*, vol. 24, pp. 118–121, July 2007.

[48] M. Mishali and Y. C. Eldar, "From theory to practice: Sub-nyquist sampling of sparse wideband analog signals," *IEEE Journal of Selected Topics in Signal Processing*, vol. 4, no. 2, pp. 375–391, 2010.

[49] C. M. Watts, D. Shrekenhamer, J. Montoya, G. Lipworth, J. Hunt, T. Sleasman, S. Krishna, D. R. Smith, and W. J. Padilla, "Terahertz compressive imaging with metamaterial spatial light modulators," *Nat Photon*, vol. 8, pp. 605–609, aug 2014.

[50] W. L. Chan, K. Charan, D. Takhar, K. F. Kelly, R. G. Baraniuk, and D. M. Mittleman, "A single-pixel terahertz imaging system based on compressed sensing," *Applied Physics Letters*, vol. 93, no. 12, p. 121105, 2008.

[51] R. I. Stantchev, D. B. Phillips, P. Hobson, S. M. Hornett, M. J. Padgett, and E. Hendry, "Compressed sensing with near-field THz radiation," *Optica*, vol. 4, pp. 989–992, aug 2017.

[52] M.-J. Sun, M. P. Edgar, G. M. Gibson, B. Sun, N. Radwell, R. Lamb, and M. J. Padgett, "Single-pixel three-dimensional imaging with time-based depth resolution," *Nature Communications*, vol. 7, p. 12010, jul 2016.

[53] M. P. Edgar, G. M. Gibson, and M. J. Padgett, "Principles and prospects for single-pixel imaging," *Nature Photonics*, vol. 13, no. 1, pp. 13–20, 2019.

[54] D. F. Chaitanya K. Mididoddi and C. Wang, "Optical phase shifting Fourier transform scanning for bandwidth-efficient blind RF spectrum sensing," in *European Conference on Optical Communication (ECOC)*, p. 1, 2018.

[55] Q. Guo, H. Chen, Y. Wang, Y. Guo, P. Liu, X. Zhu, Z. Cheng, Z. Yu, S. Yang, M. Chen, *et al.*, "High-speed compressive microscopy of flowing cells using sinusoidal illumination patterns," *IEEE Photon. J.*, vol. 9, p. 3900111, 2017.

[56] Z. Zhang, X. Ma, and J. Zhong, "Single-pixel imaging by means of fourier spectrum acquisition," *Nature communications*, vol. 6, p. 6225, 2015.

[57] A. Escobet-Montalbán, R. Spesyvtsev, M. Chen, W. A. Saber, M. Andrews, C. Simon Herrington, M. Mazilu, and K. Dholakia, "Wide-field multiphoton imaging through scattering media without correction," *Science Advances*, vol. 4, oct 2018.

[58] S. D. Johnson, D. B. Phillips, Z. Ma, S. Ramachandran, and M. J. Padgett, "A light-in-flight single-pixel camera for use in the visible and short-wave infrared," *Opt. Express*, vol. 27, pp. 9829–9837, apr 2019.

[59] M. Alemohammad, J. R. Stroud, B. T. Bosworth, and M. A. Foster, "High-speed all-optical Haar wavelet transform for real-time image compression," *Opt. Express*, vol. 25, pp. 9802–9811, may 2017.

[60] C. K. Mididoddi, G. Wang, and C. Wang, "Data compressed photonic time-stretch optical coherence tomography," in *Proc. IEEE Photon. Conf.*, pp. 13–14, 2016.

[61] C. K. Mididoddi, F. Bai, G. Wang, J. Liu, S. Gibson, and C. Wang, "High-Throughput Photonic Time-Stretch Optical Coherence Tomography with Data Compression," *IEEE Photonics Journal*, vol. 9, pp. 1–15, aug 2017.

[62] C. K. Mididoddi, G. Wang, L. Su, and C. Wang, "Photonic time-stretch optical coherence tomography with data compression and improved resolution," in *2017 Conference on Lasers and Electro-Optics Pacific Rim (CLEO-PR)*, pp. 1–3, July 2017.

[63] C. K. Mididoddi, E. J. Ahmad, and C. Wang, "Data-efficient high-throughput fiber bragg grating sensors using photonic time-stretch compressive sensing," in *2017 Conference on Lasers and Electro-Optics Europe European Quantum Electronics Conference (CLEO/Europe-EQEC)*, pp. 1–1, June 2017.

[64] C. K. Mididoddi and C. Wang, "Photonic compressive sensing enabled data efficient time stretch optical coherence tomography," in *2nd Canterbury Conference on OCT with Emphasis on Broadband Optical Sources*, vol. 10591, p. 105910F, International Society for Optics and Photonics, 2018.

[65] C. K. Mididoddi, D. Feng, and C. Wang, "All-optical high-speed temporal random pattern generation based on photonic time stretch," in *2016 15th International Conference on Optical Communications and Networks (ICOCN)*, pp. 1–4, 2016.

[66] C. Mididoddi, E. J. Ahmad, and C. Wang, "All-Optical Random Sequence Generation For Compressive Sensing Detection of RF Signals," in *2017 International Topical Meeting on Microwave Photonics (MWP) (MWP 2017)*, (Beijing, P.R. China), oct 2017.

[67] C. K. Mididoddi, G. Wang, and C. Wang, "Ultrafast single-pixel optical imaging based on multimode interference and compressed sensing (Conference Presentation)," vol. 10677, p. 106770C, 2018.

[68] C. K. Mididoddi and C. Wang, "Adaptive non-uniform photonic time stretch for blind RF signal detection with compressed time-bandwidth product," *Optics Communications*, vol. 396, no. Supplement C, pp. 221–227, 2017.

[69] B. H. Kolner, "Space-time duality and the theory of temporal imaging," *IEEE Journal of Quantum Electronics*, vol. 30, no. 8, pp. 1951–1963, 1994.

[70] A. Papoulis, "Pulse compression, fiber communications, and diffraction: a unified approach," *J. Opt. Soc. Am. A*, vol. 11, pp. 3–13, jan 1994.

[71] K. Goda and B. Jalali, "Dispersive fourier transformation for fast continuous single-shot measurements," *Nature Photonics*, vol. 7, no. 2, pp. 102–112, 2013.

[72] C. Wang and N. J. Gomes, "Photonics-enabled sub-nyquist radio frequency sensing based on temporal channelization and compressive sensing," in *Microwave Photonics (MWP) and the 2014 9th Asia-Pacific Microwave Photonics Conference (APMP), 2014 International Topical Meeting on*, pp. 335–338, IEEE, 2014.

[73] S. Gupta and B. Jalali, "Time stretch enhanced recording oscilloscope," *Applied Physics Letters*, vol. 94, no. 4, p. 041105, 2009.

[74] K. Goda, K. Tsia, and B. Jalali, "Serial time-encoded amplified imaging for real-time observation of fast dynamic phenomena," *Nature*, vol. 458, no. 7242, pp. 1145–1149, 2009.

[75] J. Chou, D. R. Solli, and B. Jalali, "Real-time spectroscopy with subgigahertz resolution using amplified dispersive fourier transformation," *Applied Physics Letters*, vol. 92, no. 11, p. 111102, 2008.

[76] T. Jannson, "Real-time fourier transformation in dispersive optical fibers," *Optics letters*, vol. 8, no. 4, pp. 232–234, 1983.

[77] M. A. Muriel, J. Azaña, and A. Carballar, "Real-time fourier transformer based on fiber gratings," *Optics letters*, vol. 24, no. 1, pp. 1–3, 1999.

[78] C. Wang, F. Zeng, and J. Yao, "All-fiber ultrawideband pulse generation based on spectral shaping and dispersion-induced frequency-to-time conversion," *IEEE Photonics Technology Letters*, vol. 19, no. 3, pp. 137–139, 2007.

[79] D. E. Leaird, A. M. Weiner, *et al.*, "Dispersion requirements in coherent frequency-to-time mapping," *Optics express*, vol. 19, no. 24, pp. 24718–24729, 2011.

[80] L. R. Chen, "Photonic generation of chirped microwave and millimeter wave pulses based on optical spectral shaping and wavelength-to-time mapping in silicon photonics," *Optics Communications*, vol. 373, pp. 70–81, 2016.

[81] D. Peng, Z. Zhang, Z. Zeng, L. Zhang, Y. Lyu, Y. Liu, and K. Xie, "Single-shot photonic time-stretch digitizer using a dissipative soliton-based passively mode-locked fiber laser," *Opt. Express*, vol. 26, pp. 6519–6531, mar 2018.

[82] J. R. Klauder, A. C. Price, S. Darlington, and W. J. Albersheim, "The theory and design of chirp radars," *The Bell System Technical Journal*, vol. 39, no. 4, pp. 745–808, 1960.

[83] G. Campbell and R. Foster, *Fourier integrals for practical applications*. Bell Telephone Laboratories series, D. Van Nostrand Co., 1948.

[84] S. K. Varshney, T. Fujisawa, K. Saitoh, and M. Koshiba, "Design and analysis of a broadband dispersion compensating photonic crystal fiber Raman amplifier operating in S-band," *Opt. Express*, vol. 14, pp. 3528–3540, apr 2006.

[85] J.-L. Wu, Y.-Q. Xu, J.-J. Xu, X.-M. Wei, A. C. S. Chan, A. H. L. Tang, A. K. S. Lau, B. M. F. Chung, H. Cheung Shum, E. Y. Lam, K. K. Y. Wong, and K. K. Tsia, "Ultrafast laser-scanning time-stretch imaging at visible wavelengths," vol. 6, p. e16196, jan 2017.

[86] C. Kong, X. Wei, K. K. M. Tsia, and K. K. Y. Wong, "Ultrafast Green-Light Swept-Source Imaging Through Advanced Fiber-Optic Technologies," *IEEE Journal of Selected Topics in Quantum Electronics*, vol. 24, no. 3, pp. 1–5, 2018.

[87] S. Tan, X. Wei, J. Wu, L. Yang, K. K. Tsia, and K. K. Y. Wong, "Flexible pulse-stretching for a swept source at 2.0um using free-space angular-chirp-enhanced delay," *Opt. Lett.*, vol. 43, pp. 102–105, jan 2018.

[88] H. Guillet de Chatellus, L. R. Cortés, and J. Azaña, "Optical real-time Fourier transformation with kilohertz resolutions," *Optica*, vol. 3, no. 1, pp. 1–8, 2016.

[89] C. Zhang, Y. Xu, X. Wei, K. K. Tsia, and K. K. Y. Wong, "Time-stretch microscopy based on time-wavelength sequence reconstruction from wideband incoherent source," *Applied Physics Letters*, vol. 105, no. 4, p. 41113, 2014.

[90] X. Xu, J. Wu, T. G. Nguyen, T. Moein, S. T. Chu, B. E. Little, R. Morandotti, A. Mitchell, and D. J. Moss, "Photonic microwave true time delays for phased array antennas using a 49GHz FSR integrated optical micro-comb source \[Invited\]," *Photon. Res.*, vol. 6, pp. B30—-B36, may 2018.

[91] P. Del'Haye, A. Schliesser, O. Arcizet, T. Wilken, R. Holzwarth, and T. J. Kippenberg, "Optical frequency comb generation from a monolithic microresonator," *Nature*, vol. 450, p. 1214, dec 2007.

[92] D. Huang, E. A. Swanson, C. P. Lin, J. S. Schuman, W. G. Stinson, W. Chang, M. R. Hee, T. Flotte, K. Gregory, C. A. Puliafito, *et al.*, "Optical coherence tomography," *Science (New York, NY)*, vol. 254, no. 5035, p. 1178, 1991.

[93] W. Drexler, U. Morgner, R. K. Ghanta, F. X. Kärtner, J. S. Schuman, and J. G. Fujimoto, "Ultrahigh-resolution ophthalmic optical coherence tomography," *Nature medicine*, vol. 7, no. 4, pp. 502–507, 2001.

[94] J. Xu, X. Wei, L. Yu, C. Zhang, J. Xu, K. K. Y. Wong, and K. K. Tsia, "Performance of megahertz amplified optical time-stretch optical coherence tomography (AOT-OCT)," *Optics Express*, vol. 22, no. 19, pp. 22498–22512, 2014.

[95] J. Kang, P. Feng, X. Wei, E. Y. Lam, K. K. Tsia, and K. K. Y. Wong, "102-nm, 44.5-MHz inertial-free swept source by mode-locked fiber laser and time stretch technique for optical coherence tomography," *Opt. Express*, vol. 26, pp. 4370–4381, feb 2018.

[96] B. T. Bosworth, J. R. Stroud, D. N. Tran, T. D. Tran, S. Chin, and M. A. Foster, "High-speed flow microscopy using compressed sensing with ultrafast laser pulses," *Opt. Express*, vol. 23, pp. 10521–10532, apr 2015.

[97] C. Lei, B. Guo, Z. Cheng, and K. Goda, "Optical time-stretch imaging: Principles and applications," *Applied Physics Reviews*, vol. 3, no. 1, p. 11102, 2016.

[98] Y. Han and B. Jalali, "Photonic time-stretched analog-to-digital converter: fundamental concepts and practical considerations," *Journal of Lightwave Technology*, vol. 21, no. 12, p. 3085, 2003.

[99] Y. Han and B. Jalali, "Continuous-time time-stretched analog-to-digital converter array implemented using virtual time gating," *IEEE Transactions on Circuits and Systems I: Regular Papers*, vol. 52, no. 8, pp. 1502–1507, 2005.

[100] G. C. Valley, "Photonic analog-to-digital converters," *Optics Express*, vol. 15, no. 5, pp. 1955–1982, 2007.

[101] G. Wang, U. Habib, Z. Yan, N. J. Gomes, L. Zhang, and C. Wang, "In-fibre diffraction grating based beam steering for full duplex optical wireless communication," in *2017 International Topical Meeting on Microwave Photonics (MWP)*, pp. 1–4, 2017.

[102] HerinkG., JalaliB., RopersC., and S. R., "Resolving the build-up of femtosecond mode-locking with single-shot spectroscopy at 90 MHz frame rate," *Nat Photon*, vol. 10, pp. 321–326, may 2016.

[103] F. Coppinger, A. Bhushan, and B. Jalali, "Photonic time stretch and its application to analog-to-digital conversion," *IEEE Transactions on microwave theory and techniques*, vol. 47, no. 7, pp. 1309–1314, 1999.

[104] J. Chou, O. Boyraz, D. Solli, and B. Jalali, "Femtosecond real-time single-shot digitizer," *Applied Physics Letters*, vol. 91, no. 16, p. 161105, 2007.

[105] C. Investigations, "Fill in the Blanks: Using Math to Turn Lo-Res Datasets Into Hi-Res Samples," *https://www.wired.com/2010/02/ff_algorithm/*, no. 50, 2009.

[106] E. J. Candès, J. Romberg, and T. Tao, "Robust uncertainty principles: Exact signal reconstruction from highly incomplete frequency information," *IEEE Transactions on information theory*, vol. 52, no. 2, pp. 489–509, 2006.

[107] S. Foucart and H. Rauhut, *A Mathematical Introduction to Compressive Sensing*. 2013.

[108] B. J. Erickson, "PACS: A Guide to the Digital Revolution," pp. 229–247, New York, NY: Springer New York, 2006.

[109] L. V. Amitonova and J. F. de Boer, "Compressive imaging through a multimode fiber," *Opt. Lett.*, vol. 43, pp. 5427–5430, nov 2018.

[110] M. Mishali and Y. C. Eldar, "Sub-Nyquist Sampling," vol. 28, no. 6, pp. 98–124, 2011.

[111] M. Mishali, Y. C. Eldar, O. Dounaevsky, and E. Shoshan, "Xampling: Analog to digital at sub-Nyquist rates," vol. 5, no. 1, pp. 8–20, 2011.

[112] M. Mishali and Y. C. Eldar, "From Theory to Practice: Sub-Nyquist Sampling of Sparse Wideband Analog Signals," vol. 4, no. 2, pp. 375–391, 2010.

[113] J. A. Tropp, J. N. Laska, M. F. Duarte, J. K. Romberg, and R. G. Baraniuk, "Beyond Nyquist: Efficient Sampling of Sparse Bandlimited Signals," *IEEE Transactions on Information Theory*, vol. 56, no. 1, pp. 520–544, 2010.

[114] Y. C. Eldar and T. Michaeli, "Beyond bandlimited sampling," vol. 26, no. 3, pp. 48–68, 2009.

[115] J. Romberg, "Imaging via Compressive Sampling," *IEEE Signal Processing Magazine*, vol. 25, no. 2, pp. 14–20, 2008.

[116] R. Baraniuk, "Compressive Sensing [Lecture Notes]," *IEEE Signal Processing Magazine*, vol. 24, pp. 118–121, jul 2007.

[117] S. Kirolos, J. Laska, M. Wakin, M. Duarte, D. Baron, T. Ragheb, Y. Massoud, and R. Baraniuk, "Analog-to-Information Conversion via Random Demodulation," 2006.

[118] J. M. Nichols and F. Bucholtz, "Beating nyquist with light: a compressively sampled photonic link," *Opt. Express*, vol. 19, pp. 7339–7348, Apr 2011.

[119] F. Yin, Y. Gao, Y. Dai, J. Zhang, K. Xu, Z. Zhang, J. Li, and J. Lin, "Multifrequency radio frequency sensing with photonics-assisted spectrum compression," *Optics Letters*, vol. 38, no. 21, pp. 4386–4388, 2013.

[120] H. Chi, Y. Mei, Y. Chen, D. Wang, S. Zheng, X. Jin, and X. Zhang, "Microwave spectral analysis based on photonic compressive sampling with random demodulation," *Opt. Lett.*, vol. 37, pp. 4636–4638, nov 2012.

[121] L. Yan, Y. Dai, K. Xu, J. Wu, Y. Li, Y. Ji, and J. Lin, "Integrated multifrequency recognition and downconversion based on photonics-assisted compressive sampling," *IEEE Photonics Journal*, vol. 4, no. 3, pp. 664–670, 2012.

[122] Y. Liang, M. Chen, H. Chen, C. Lei, P. Li, and S. Xie, "Photonic-assisted multi-channel compressive sampling based on effective time delay pattern," *Optics Express*, vol. 21, no. 22, pp. 25700–25707, 2013.

[123] Y. Chen, X. Yu, H. Chi, X. Jin, X. Zhang, S. Zheng, and M. Galili, "Compressive sensing in a photonic link with optical integration," *Opt. Lett.*, vol. 39, pp. 2222–2224, apr 2014.

[124] T. P. McKenna, J. H. Kalkavage, M. D. Sharp, and T. R. Clark, "Wideband photonic compressive sampling system," *Journal of Lightwave Technology*, vol. 34, no. 11, pp. 2848–2855, 2016.

[125] B. T. Bosworth and M. A. Foster, "High-speed ultrawideband photonically enabled compressed sensing of sparse radio frequency signals," *Optics Letters*, vol. 38, p. 4892, nov 2013.

[126] H. Chen, Z. Weng, Y. Liang, C. Lei, F. Xing, M. Chen, and S. Xie, "High speed single-pixel imaging via time domain compressive sampling," in *2014 Conference on Lasers and Electro-Optics (CLEO) - Laser Science to Photonic Applications*, pp. 1–2, 2014.

[127] Q. Guo, H. Chen, Z. Weng, M. Chen, S. Yang, and S. Xie, "Compressive sensing based high-speed time-stretch optical microscopy for two-dimensional image acquisition," *Optics Express*, vol. 23, no. 23, pp. 29639–29646, 2015.

[128] A. C. Chan, A. K. Lau, K. K. Wong, E. Y. Lam, and K. K. Tsia, "Arbitrary two-dimensional spectrally encoded pattern generation—a new strategy for high-speed patterned illumination imaging," *Optica*, vol. 2, no. 12, pp. 1037–1044, 2015.

[129] G. M. Gibson, B. Sun, M. P. Edgar, D. B. Phillips, N. Hempler, G. T. Maker, G. P. A. Malcolm, and M. J. Padgett, "Real-time imaging of methane gas leaks using a single-pixel camera," *Opt. Express*, vol. 25, pp. 2998–3005, feb 2017.

[130] G. C. Valley, G. A. Sefler, and T. J. Shaw, "Compressive sensing of sparse radio frequency signals using optical mixing," *Opt. Lett.*, vol. 37, pp. 4675–4677, nov 2012.

[131] C. Lei, Y. Wu, A. C. Sankaranarayanan, S. M. Chang, B. Guo, N. Sasaki, H. Kobayashi, C. W. Sun, Y. Ozeki, and K. Goda, "Ghz optical time-stretch microscopy by compressive sensing," *IEEE Photonics Journal*, vol. 9, pp. 1–8, April 2017.

[132] J. Shin, B. Bosworth, and M. A. Foster, "Compressive Optical Imaging Using a Multi-core Fiber and Spatially Dependent Scattering," in *Conference on Lasers and Electro-Optics*, p. SW1G.5, Optical Society of America, 2016.

[133] E. Huang, Q. Ma, and Z. Liu, "Ultrafast imaging using spectral resonance modulation," *Scientific reports*, vol. 6, p. 25240, 2016.

[134] G. C. Valley, G. A. Sefler, and T. Justin Shaw, "Multimode waveguide speckle patterns for compressive sensing," *Optics Letters*, vol. 41, no. 11, pp. 2529–2532, 2016.

[135] A. Liutkus, D. Martina, S. Popoff, G. Chardon, O. Katz, G. Lerosey, S. Gigan, L. Daudet, and I. Carron, "Imaging with nature: Compressive imaging using a multiply scattering medium," *Scientific reports*, vol. 4, p. 5552, 2014.

[136] J. Shin, B. T. Bosworth, and M. A. Foster, "Single-pixel imaging using compressed sensing and wavelength-dependent scattering," *Optics Letters*, vol. 41, no. 5, pp. 886–889, 2016.

[137] Z. Zhu, H. Chi, S. Zheng, T. Jin, X. Jin, and X. Zhang, "Analysis of compressive sensing with optical mixing using a spatial light modulator," *Applied Optics*, vol. 54, no. 8, pp. 1894–1899, 2015.

[138] B. C. Grubel, B. T. Bosworth, M. R. Kossey, H. Sun, A. B. Cooper, M. A. Foster, and A. C. Foster, "Silicon photonic physical unclonable function," *Optics Express*, vol. 25, no. 11, pp. 12710–12721, 2017.

[139] H. Sun, B. T. Bosworth, B. C. Grubel, M. Kossey, M. A. Foster, and A. Foster, "Compressed Sensing of Sparse RF Signals Based on Silicon Photonic Microcavities," in *Conference on Lasers and Electro-Optics*, OSA Technical Digest (online), (San Jose, California), p. SM1O.5, Optical Society of America, 2017.

[140] M. Li and J. Yao, "Ultrafast all-optical wavelet transform based on temporal pulse shaping incorporating a 2-d array of cascaded linearly chirped fiber bragg gratings," *IEEE Photonics Technology Letters*, vol. 24, pp. 1319–1321, Aug 2012.

[141] C. Hoessbacher, A. Josten, B. Baeuerle, Y. Fedoryshyn, H. Hettrich, Y. Salamin, W. Heni, C. Haffner, C. Kaiser, R. Schmid, D. L. Elder, D. Hillerkuss, M. Möller, L. R. Dalton, and J. Leuthold, "Plasmonic modulator with >170 GHz bandwidth demonstrated at 100 GBd NRZ," *Opt. Express*, vol. 25, pp. 1762–1768, feb 2017.

[142] B. Dai, S. Yin, Z. Gao, K. Wang, D. Zhang, S. Zhuang, and X. Wang, "Data Compression for Time-Stretch Imaging Based on Differential Detection and Run-Length Encoding," *J. Lightwave Technol.*, vol. 35, pp. 5098–5104, dec 2017.

[143] A. G. Podoleanu and R. B. Rosen, "Combinations of techniques in imaging the retina with high resolution," *Progress in retinal and eye research*, vol. 27, no. 4, pp. 464–499, 2008.

[144] X. Shu, L. J. Beckmann, and H. F. Zhang, "Visible-light optical coherence tomography: a review," *Journal of Biomedical Optics*, vol. 22, pp. 1–14, dec 2017.

[145] B. Potsaid, B. Baumann, D. Huang, S. Barry, A. E. Cable, J. S. Schuman, J. S. Duker, and J. G. Fujimoto, "Ultrahigh speed 1050nm swept source/Fourier domain OCT retinal and anterior segment imaging at 100,000 to 400,000 axial scans per second," *Optics express*, vol. 18, pp. 20029–20048, sep 2010.

[146] D. Stifter, "Beyond biomedicine: a review of alternative applications and developments for optical coherence tomography," *Applied Physics B*, vol. 88, pp. 337–357, aug 2007.

[147] N. M. Israelsen, C. R. Petersen, A. Barh, D. Jain, M. Jensen, G. Hannesschläger, P. Tidemand-Lichtenberg, C. Pedersen, A. Podoleanu, and O. Bang, "Real-time high-resolution mid-infrared optical coherence tomography," *Light: Science & Applications*, vol. 8, no. 1, p. 11, 2019.

[148] D. Stifter, "Beyond biomedicine: a review of alternative applications and developments for optical coherence tomography," *Applied Physics B*, vol. 88, no. 3, pp. 337–357, 2007.

[149] R. Leitgeb, C. Hitzenberger, and A. F. Fercher, "Performance of fourier domain vs. time domain optical coherence tomography," *Optics express*, vol. 11, no. 8, pp. 889–894, 2003.

[150] R. Huber, M. Wojtkowski, and J. Fujimoto, "Fourier domain mode locking (fdml): A new laser operating regime and applications for optical coherence tomography," *Optics express*, vol. 14, no. 8, pp. 3225–3237, 2006.

[151] D. Choi, H. Hiro-Oka, H. Furukawa, R. Yoshimura, M. Nakanishi, K. Shimizu, and K. Ohbayashi, "Fourier domain optical coherence tomography using optical demultiplexers imaging at 60,000,000 lines/s," *Optics letters*, vol. 33, no. 12, pp. 1318–1320, 2008.

[152] A. G. Podoleanu and A. Bradu, "Master–slave interferometry for parallel spectral domain interferometry sensing and versatile 3d optical coherence tomography," *Optics express*, vol. 21, no. 16, pp. 19324–19338, 2013.

[153] S. Moon and D. Y. Kim, "Ultra-high-speed optical coherence tomography with a stretched pulse supercontinuum source," *Optics express*, vol. 14, no. 24, pp. 11575–11584, 2006.

[154] K. Goda, A. Fard, O. Malik, G. Fu, A. Quach, and B. Jalali, "High-throughput optical coherence tomography at 800 nm," *Optics express*, vol. 20, no. 18, pp. 19612–19617, 2012.

[155] J. Xu, C. Zhang, J. Xu, K. Wong, and K. Tsia, "Megahertz all-optical swept-source optical coherence tomography based on broadband amplified optical time-stretch," *Optics letters*, vol. 39, no. 3, pp. 622–625, 2014.

[156] J. Xu, X. Wei, L. Yu, C. Zhang, J. Xu, K. Wong, and K. K. Tsia, "High-performance multi-megahertz optical coherence tomography based on amplified optical time-stretch," *Biomedical optics express*, vol. 6, no. 4, pp. 1340–1350, 2015.

[157] E. Lebed, P. J. Mackenzie, M. V. Sarunic, and M. F. Beg, "Rapid volumetric oct image acquisition using compressive sampling," *Optics express*, vol. 18, no. 20, pp. 21003–21012, 2010.

[158] X. Liu and J. U. Kang, "Compressive sd-oct: the application of compressed sensing in spectral domain optical coherence tomography," *Opt. Express*, vol. 18, pp. 22010–22019, Oct 2010.

[159] N. Zhang, T. Huo, C. Wang, T. Chen, J.-g. Zheng, and P. Xue, "Compressed sensing with linear-in-wavenumber sampling in spectral-domain optical coherence tomography," *Optics letters*, vol. 37, no. 15, pp. 3075–3077, 2012.

[160] C. Liu, A. Wong, K. Bizheva, P. Fieguth, and H. Bie, "Homotopic, non-local sparse reconstruction of optical coherence tomography imagery," *Optics express*, vol. 20, no. 9, pp. 10200–10211, 2012.

[161] S. Schwartz, C. Liu, A. Wong, D. A. Clausi, P. Fieguth, and K. Bizheva, "Energy-guided learning approach to compressive fd-oct," *Optics express*, vol. 21, no. 1, pp. 329–344, 2013.

[162] D. Xu, Y. Huang, and J. U. Kang, "Real-time compressive sensing spectral domain optical coherence tomography," *Optics letters*, vol. 39, no. 1, pp. 76–79, 2014.

[163] B. Jalali and M. H. Asghari, "The anamorphic stretch transform: Putting the squeeze on "big data"," *Optics and Photonics News*, vol. 25, no. 2, pp. 24–31, 2014.

[164] C. V. McLaughlin, J. M. Nichols, and F. Bucholtz, "Basis mismatch in a compressively sampled photonic link," *IEEE Photonics Technology Letters*, vol. 25, no. 23, pp. 2297–2300, 2013.

[165] B. T. Bosworth, J. R. Stroud, D. N. Tran, T. D. Tran, S. Chin, and M. A. Foster, "Ultra-wideband compressed sensing of arbitrary multi-tone sparse radio frequencies using spectrally encoded ultrafast laser pulses," *Optics Letters*, vol. 40, no. 13, pp. 3045–3048, 2015.

[166] K. Koh, S.-J. Kim, and S. Boyd, "An interior-point method for large-scale l1-regularized logistic regression," *Journal of Machine learning research*, vol. 8, no. Jul, pp. 1519–1555, 2007.

[167] S. Boyd, N. Parikh, E. Chu, B. Peleato, and J. Eckstein, "Distributed optimization and statistical learning via the alternating direction method of multipliers," *Foundations and Trends® in Machine Learning*, vol. 3, no. 1, pp. 1–122, 2011.

[168] J. Friedman, T. Hastie, and R. Tibshirani, "Regularization paths for generalized linear models via coordinate descent," *Journal of statistical software*, vol. 33, no. 1, p. 1, 2010.

[169] S. Becker, J. Bobin, and E. J. Candès, "Nesta: A fast and accurate first-order method for sparse recovery," *SIAM Journal on Imaging Sciences*, vol. 4, no. 1, pp. 1–39, 2011.

[170] C. Wang and J. Yao, "Ultrahigh-resolution photonic-assisted microwave frequency identification based on temporal channelization," *IEEE Transactions on Microwave Theory and Techniques*, vol. 61, no. 12, pp. 4275–4282, 2013.

[171] E. J. Ahmad, C. Wang, D. Feng, Z. Yan, and L. Zhang, "High temporal and spatial resolution distributed fiber bragg grating sensors using time-stretch frequency-domain reflectometry," *Journal of Lightwave Technology*, vol. 35, pp. 3289–3295, Aug 2017.

[172] G. Rodriguez, M. Jaime, F. Balakirev, C. H. Mielke, A. Azad, B. Marshall, B. M. L. Lone, B. Henson, and L. Smilowitz, "Coherent pulse interrogation system for fiber bragg grating sensing of strain and pressure in dynamic extremes of materials," *Opt. Express*, vol. 23, pp. 14219–14233, Jun 2015.

[173] G. C. Valley, G. A. Sefler, and T. J. Shaw, "Use of optical speckle patterns for compressive sensing of rf signals in the ghz band," in *Terahertz, RF, Millimeter, and Submillimeter-Wave Technology and Applications IX*, vol. 9747, p. 97470B, International Society for Optics and Photonics, 2016.

[174] J. Shin, B. T. Bosworth, and M. A. Foster, "Compressive fluorescence imaging using a multi-core fiber and spatially dependent scattering," *Opt. Lett.*, vol. 42, pp. 109–112, jan 2017.

[175] B. W. Pogue, "Ultrafast imaging takes on a new design," *Nature*, vol. 516, p. 46, dec 2014.

[176] D. B. Phillips, M.-J. Sun, J. M. Taylor, M. P. Edgar, S. M. Barnett, G. M. Gibson, and M. J. Padgett, "Adaptive foveated single-pixel imaging with dynamic supersampling," *Science Advances*, vol. 3, no. 4, 2017.

[177] M. Bolea, J. Mora, L. R. Chen, and J. Capmany, "Highly Chirped Reconfigurable Microwave Photonic Filter," *IEEE Photonics Technology Letters*, vol. 23, pp. 1192–1194, sep 2011.

[178] M. Bolea, J. Mora, B. Ortega, and J. Capmany, "Highly chirped single-bandpass microwave photonic filter with reconfiguration capabilities," *Opt. Express*, vol. 19, pp. 4566–4576, feb 2011.

[179] C. Wang and J. Yao, "Chirped Microwave Pulse Compression Using a Photonic Microwave Filter With a Nonlinear Phase Response," *IEEE Transactions on Microwave Theory and Techniques*, vol. 57, no. 2, pp. 496–504, 2009.

[180] C. Wang, F. Zeng, and J. Yao, "All-Fiber Ultrawideband Pulse Generation Based on Spectral Shaping and Dispersion-Induced Frequency-to-Time Conversion," *IEEE Photonics Technology Letters*, vol. 19, no. 3, pp. 137–139, 2007.

[181] Y. Dai and J. Yao, "Nonuniformly Spaced Photonic Microwave Delay-Line Filters and Applications," *IEEE Transactions on Microwave Theory and Techniques*, vol. 58, no. 11, pp. 3279–3289, 2010.

[182] X. Dong, P. Shum, N. Q. Ngo, C. C. Chan, J. H. Ng, and C. Zhao, "Largely tunable CFBG-based dispersion compensator with fixed center wavelength," *Opt. Express*, vol. 11, pp. 2970–2974, nov 2003.

[183] C. Wang and J. Yao, "Photonic Generation of Chirped Millimeter-Wave Pulses Based on Nonlinear Frequency-to-Time Mapping in a Nonlinearly Chirped Fiber Bragg Grating," *IEEE Transactions on Microwave Theory and Techniques*, vol. 56, no. 2, pp. 542–553, 2008.

[184] E. D. Diebold, N. K. Hon, Z. Tan, J. Chou, T. Sienicki, C. Wang, and B. Jalali, "Giant tunable optical dispersion using chromo-modal excitation of a multimode waveguide," *Opt. Express*, vol. 19, pp. 23809–23817, nov 2011.

[185] G. Stepniak, L. Maksymiuk, and J. Siuzdak, "Binary-Phase Spatial Light Filters for Mode-Selective Excitation of Multimode Fibers," *Journal of Lightwave Technology*, vol. 29, no. 13, pp. 1980–1987, 2011.

[186] D. L. Marks, O. Yurduseven, and D. R. Smith, "Sparse blind deconvolution for imaging through layered media," *Optica*, vol. 4, pp. 1514–1521, dec 2017.

Appendix A

Publications produced from work reported in this thesis

Journal Publications:

- **C. K. Mididoddi,** F. Bai, G. Wang, J. Liu, S. Gibson and C. Wang, “High-Throughput Photonic Time-Stretch Optical Coherence Tomography with Data Compression,” *IEEE Photonics Journal*, 9(4), 1-15, (2017). (doi:10.1109/JPHOT.2017.2716179)

- **C. K. Mididoddi**, C. Wang, “Adaptive non-uniform photonic time stretch for high-speed signal detection with compressed time-bandwidth product," 2017. - *Optics Communications*,
  vol. 396, pp. 221-227, Aug. 2017. (https://doi.org/10.1016/j.optcom.2017.03.052)

Conference papers:

- **C. K. Mididoddi**, G. Wang and C. Wang, “Data Compressed Photonic Time-Stretch Optical Coherence Tomography," *2016 IEEE Photonics Conference (IPC),* Waikoloa, HI, USA, 2016, pp. 13-14.(doi:10.1109/IPCon.2016.7830959)

- **C. K. Mididoddi**, D. Feng, and C. Wang , “All-optical temporal random pattern generation based on photonic time-stretch”, *2016 15th IEEE International Conference on Optical Communications and Networks (ICOCN)*, 2016, Hangzhou, China, pp. 1-4. (doi:10.1109/ICOCN.2016.7875814)

- **C. K. Mididoddi**, E. J. Ahmed, C. Wang, “All-Optical Random Sequence Generation For Compressed Sensing Detection of RF Signals" - *IEEE MWP conference, Beijing, 2017*.(doi:10.1109/MWP.2017.8168639)

- **C. K. Mididoddi**, C. Wang, “Photonic compressive sensing enabled data efficient time stretch optical coherence tomography" - *Proc. SPIE 10591, 2nd Canterbury Conference on OCT with Emphasis on Broadband Optical Sources 105910F.* doi: 10.1117/12.2283035.

- **C. K. Mididoddi,** G. Wang, L. Su and C. Wang, “Photonic time-stretch optical coherence tomography with data compression and improved resolution," *2017 Conference on Lasers and Electro-Optics Pacific Rim (CLEO-PR),* Singapore, 2017, pp. 1-3. doi: 10.1109/CLEOPR.2017.8118840

- **C. K. Mididoddi,** E. J. Ahmad and C. Wang, “Data-efficient high-throughput fiber Bragg grating sensors using photonic time-stretch compressive sensing," *2017 Conference on Lasers and Electro-Optics Europe & European Quantum Electronics Conference (CLEO/Europe-EQEC),* Munich, 2017, pp. 1-1.doi: 10.1109/CLEOE-EQEC.2017.8086896

- **C. K. Mididoddi**, G. Wang, C. Wang, “Ultrafast single-pixel optical imaging based on multimode interference and compressed sensing" *2018 SPIE Photonics Europe, paper 10677-12*, 22 – 26 Apr. 2018, Strasbourg, France.

- **C. K. Mididoddi**, D. Feng, C. Wang, “Optical Phase Shifting Fourier Transform Scanning for Bandwidth-Efficient Blind RF Spectrum Sensing" *2018 European Conference on Optical Communication* (ECOC), 23 Sep. 2018, Rome, Italy..
- **C. K. Mididoddi**, G. Wang, U. Habib, H. Zhang and C. Wang, “Ultrafast User Localization and Beam Steering in Optical Wireless Communication Using an In-Fibre Diffraction Grating" - *IEEE MWP conference, Toulouse, 2018.*
- X. Liu, **C. K. Mididoddi**, G. Wang, Z. Tan and C. Wang, “Tunable Multimode Optical Delay Line for Single-Wavelength Microwave Photonic Transversal Filter" - *IEEE MWP conference, Toulouse, 2018.*
- S. Liu, **C. K. Mididoddi**, H. Zhou, B. Li, W. Xu and C. Wang, “Single-Shot Sub-Nyquist RF Signal Reconstruction Based on Deep Learning Network" - *IEEE MWP conference, Toulouse, 2018.*

Appendix B

Equipment used in the experiments

Following are the list of equipment used in the experiments and their specifications.

Fig. B.1 Mendocino series FPL type C -band Desktop 1550nm femtosecond laser

Table B.1 Specifications of MLL

Parameters	Typical values
Central Wavelength	1550 nm
Optical bandwidth	9-16 nm
Pulse width	800 fs
Repetition rate	50 MHz
Optical Power	10-20 mW

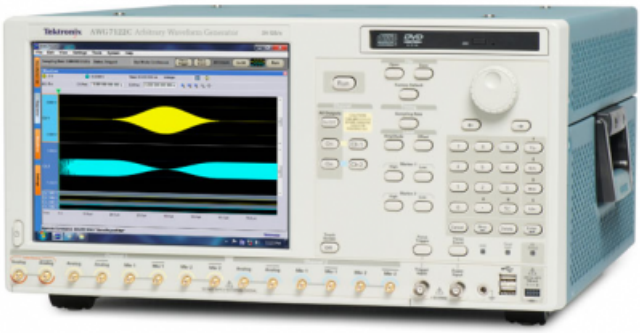

Fig. B.2 Tektronix Arbitrary Waveform Generator 7122C

Table B.2 Specifications of AWG:

Parameters	Typical Values
Sampling Rate	12 GS/s
Amplitude	+4 dBm
Resolution	10 bit
Modulation Bandwidth	4.8 GHz

Fig. B.3 Agilent 86100A Wideband sampling scope

Table B.3 Specifications of sampling oscilloscope:

Parameters	Typical Values
Optical channel	9/125 SMF, 53 GHz RF bandwidth PD, max. optical power: 20 mW
Electrical channel	1.85mm male input, 63GHz RF bandwidth, max. signal input: $\pm 2V_{dc}$
TBP	375

Fig. B.4 Tektronix realtime oscilloscope

Table B.4 Specifications of realtime oscilloscope:

Parameters	Typical Values
Analog Bandwidth	23 GHz
Sampling rate	100 GS/s
Maximum number of samples recorded	31.25 M

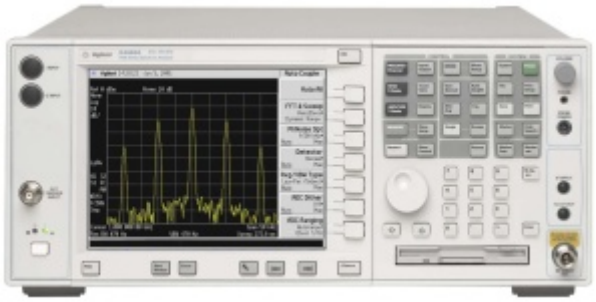

Fig. B.5 E4440A PSA Spectrum Analyzer

Table B.5 Specifications of electrical spectrum analyser:

Parameters	Typical Values
Detection Bandwidth	3 Hz to 26.5 GHz

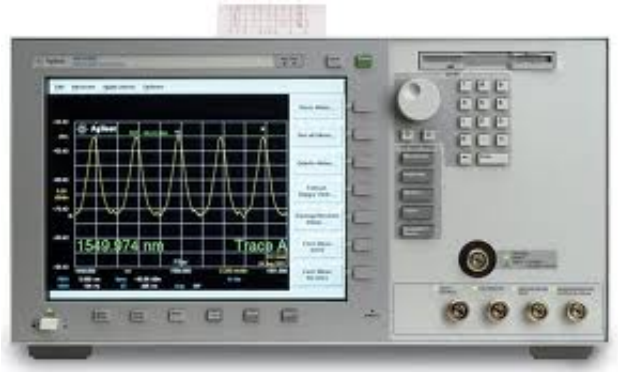

Fig. B.6 Optical Spectrum Analyzer Agilent 86146B

Table B.6 Specifications of optical spectrum analyser:

Parameters	Typical Values
Wavelength range	600-1700 nm
Resolution bandwidth	0.06 nm
Sensitivity	-90 dBm
Dynamic Range	-70 dB

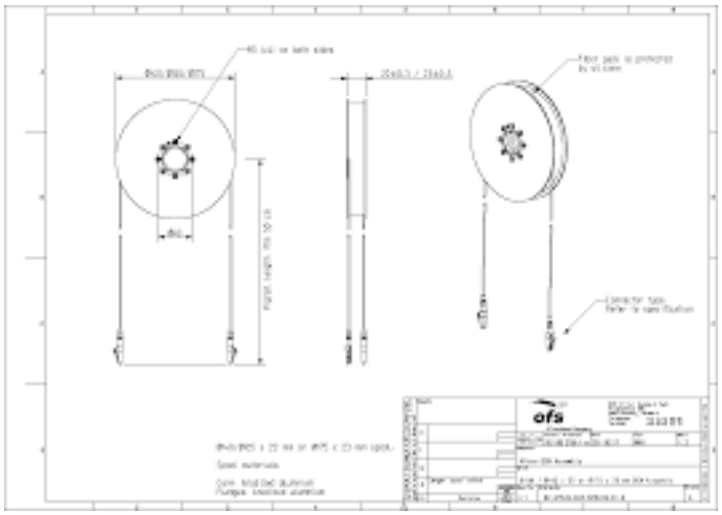

Fig. B.7 Dispersion Compensating Fibre OFS SMFDK-S-020-03-01

Table B.7 Specifications of DCF:

Parameters	Typical Values
Wavelength range	1550 nm
Compensated fibre length	20 km
Dispersion	-330 ps/nm
Connector type	FC/APC

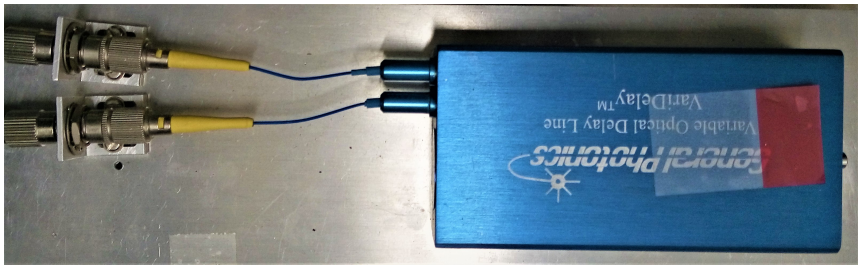

Fig. B.8 General Photonics Variable Optical Delay Line VDL-001

Table B.8 Specifications of optical delay line:

Parameters	Typical Values
Maximum Optical Delay	600 ps
Insertion Loss	1 dB
Optical Wavelength	1550 nm $\pm 50nm$

Fig. B.9 General Photonics Motorized Optical Delay Line MDL-001

Table B.9 Specifications of motorized optical delay line:

Parameters	Typical Values
Maximum Optical Delay	330 ps
Insertion Loss	1 dB
Optical Wavelength	1550 nm $\pm 50nm$

Fig. B.10 Amonics Optical Fibre Amplifier Pre Amplifier AEDFA-PA-35-B-FA

Table B.10 Specifications of optical amplifier:

Parameters	Typical Values
Optical Wavelength Range	1530-1563 nm
Connector Type	FC/APC
Maximum optical gain	35 dB
Input Signal Range	-40 - -10 dBm

Appendix C

Sample MATLAB code used for post-processing

```
% l1eq_pd.m
%
% Solve
% min_x ||x||_1  s.t.  Ax = b
%
% Recast as linear program
% min_{x,u} sum(u)  s.t.  -u <= x <= u,  Ax=b
% and use primal-dual interior point method
%
% Usage: xp = l1eq_pd(x0, A, At, b, pdtol, pdmaxiter, cgtol
    , cgmaxiter)
%
% x0 - Nx1 vector, initial point.
%
```

```
% A - Either a handle to a function that takes a N vector
    and returns a K
%       vector , or a KxN matrix.  If A is a function handle,
     the algorithm
%       operates in "largescale" mode, solving the Newton
    systems via the
%       Conjugate Gradients algorithm.
%
% At - Handle to a function that takes a K vector and
    returns an N vector.
%        If A is a KxN matrix, At is ignored.
%
% b - Kx1 vector of observations.
%
% pdtol - Tolerance for primal-dual algorithm (algorithm
    terminates if
%       the duality gap is less than pdtol).
%       Default = 1e-3.
%
% pdmaxiter - Maximum number of primal-dual iterations.
%       Default = 50.
%
% cgtol - Tolerance for Conjugate Gradients; ignored if A
    is a matrix.
%       Default = 1e-8.
%
```

```
% cgmaxiter - Maximum number of iterations for Conjugate
    Gradients; ignored
%       if A is a matrix.
%       Default = 200.
%
% Written by: Justin Romberg, Caltech
% Email: jrom@acm.caltech.edu
% Created: October 2005
%

function xp = l1eq_pd(x0, A, At, b, pdtol, pdmaxiter, cgtol
    , cgmaxiter)

largescale = isa(A,'function_handle');

if (nargin < 5), pdtol = 1e-3;  end
if (nargin < 6), pdmaxiter = 50;  end
if (nargin < 7), cgtol = 1e8;  end
if (nargin < 8), cgmaxiter = 200;  end

N = length(x0);

alpha = 0.01;
beta = 0.5;
mu = 10;
```

```
gradf0 = [zeros(N,1); ones(N,1)];

% starting point --- make sure that it is feasible
if (largescale)
if (norm(A(x0)-b)/norm(b) > cgtol)
disp('Starting point infeasible; using x0 = At*inv(AAt)*y.'
   );
AAt = @(z) A(At(z));
[w, cgres, cgiter] = cgsolve(AAt, b, cgtol, cgmaxiter, 0);
if (cgres > 1/2)
disp('A*At is ill-conditioned: cannot find starting point')
   ;
xp = x0;
return;
end
x0 = At(w);
end
else
if (norm(A*x0-b)/norm(b) > cgtol)
disp('Starting point infeasible; using x0 = At*inv(AAt)*y.'
   );
opts.POSDEF = true; opts.SYM = true;
[w, hcond] = linsolve(A*A', b, opts);
if (hcond < 1e-14)
disp('A*At is ill-conditioned: cannot find starting point')
   ;
```

```
xp = x0;
return;
end
x0 = A'*w;
end
end
x = x0;
u = (0.95)*abs(x0) + (0.10)*max(abs(x0));

% set up for the first iteration
fu1 = x - u;
fu2 = -x - u;
lamu1 = -1./fu1;
lamu2 = -1./fu2;
if (largescale)
v = -A(lamu1-lamu2);
Atv = At(v);
rpri = A(x) - b;
else
v = -A*(lamu1-lamu2);
Atv = A'*v;
rpri = A*x - b;
end

sdg = -(fu1'*lamu1 + fu2'*lamu2);
tau = mu*2*N/sdg;
```

```
rcent = [-lamu1.*fu1; -lamu2.*fu2] - (1/tau);
rdual = gradf0 + [lamu1-lamu2; -lamu1-lamu2] + [Atv; zeros(
   N,1)];
resnorm = norm([rdual; rcent; rpri]);

pditer = 0;
done = (sdg < pdtol) | (pditer >= pdmaxiter);
while (~done)

pditer = pditer + 1;

w1 = -1/tau*(-1./fu1 + 1./fu2) - Atv;
w2 = -1 - 1/tau*(1./fu1 + 1./fu2);
w3 = -rpri;

sig1 = -lamu1./fu1 - lamu2./fu2;
sig2 = lamu1./fu1 - lamu2./fu2;
sigx = sig1 - sig2.^2./sig1;

if (largescale)
w1p = w3 - A(w1./sigx - w2.*sig2./(sigx.*sig1));
h11pfun = @(z) -A(1./sigx.*At(z));
[dv, cgres, cgiter] = cgsolve(h11pfun, w1p, cgtol,
   cgmaxiter, 0);
if (cgres > 1/2)
```

```
disp('Cannot solve system.  Returning previous iterate.  (
   See Section 4 of notes for more information.)');
xp = x;
return
end
dx = (w1 - w2.*sig2./sig1 - At(dv))./sigx;
Adx = A(dx);
Atdv = At(dv);
else
w1p = -(w3 - A*(w1./sigx - w2.*sig2./(sigx.*sig1)));
H11p = A*(sparse(diag(1./sigx))*A');
opts.POSDEF = true; opts.SYM = true;
[dv,hcond] = linsolve(H11p, w1p, opts);
if (hcond < 1e-14)
disp('Matrix ill-conditioned.  Returning previous iterate.
    (See Section 4 of notes for more information.)');
xp = x;
return
end
dx = (w1 - w2.*sig2./sig1 - A'*dv)./sigx;
Adx = A*dx;
Atdv = A'*dv;
end


du = (w2 - sig2.*dx)./sig1;
```

```
dlamu1 = (lamu1./fu1).*(-dx+du) - lamu1 - (1/tau)*1./fu1;
dlamu2 = (lamu2./fu2).*(dx+du) - lamu2 - 1/tau*1./fu2;

% make sure that the step is feasible: keeps lamu1,lamu2 >
    0, fu1,fu2 < 0
indp = find(dlamu1 < 0);  indn = find(dlamu2 < 0);
s = min([1; -lamu1(indp)./dlamu1(indp); -lamu2(indn)./
    dlamu2(indn)]);
indp = find((dx-du) > 0);  indn = find((-dx-du) > 0);
s = (0.99)*min([s; -fu1(indp)./(dx(indp)-du(indp)); -fu2(
    indn)./(-dx(indn)-du(indn))]);

% backtracking line search
suffdec = 0;
backiter = 0;
while (~suffdec)
xp = x + s*dx;  up = u + s*du;
vp = v + s*dv;  Atvp = Atv + s*Atdv;
lamu1p = lamu1 + s*dlamu1;  lamu2p = lamu2 + s*dlamu2;
fu1p = xp - up;  fu2p = -xp - up;
rdp = gradf0 + [lamu1p-lamu2p; -lamu1p-lamu2p] + [Atvp;
    zeros(N,1)];
rcp = [-lamu1p.*fu1p; -lamu2p.*fu2p] - (1/tau);
rpp = rpri + s*Adx;
suffdec = (norm([rdp; rcp; rpp]) <= (1-alpha*s)*resnorm);
s = beta*s;
```

```
backiter = backiter + 1;
if (backiter > 32)
disp('Stuck backtracking, returning last iterate. (See
    Section 4 of notes for more information.)')
xp = x;
return
end
end


% next iteration
x = xp;  u = up;
v = vp;  Atv = Atvp;
lamu1 = lamu1p;  lamu2 = lamu2p;
fu1 = fu1p;  fu2 = fu2p;

% surrogate duality gap
sdg = -(fu1'*lamu1 + fu2'*lamu2);
tau = mu*2*N/sdg;
rpri = rpp;
rcent = [-lamu1.*fu1; -lamu2.*fu2] - (1/tau);
rdual = gradf0 + [lamu1-lamu2; -lamu1-lamu2] + [Atv; zeros(
    N,1)];
resnorm = norm([rdual; rcent; rpri]);

done = (sdg < pdtol) | (pditer >= pdmaxiter);
```

```
disp(sprintf('Iteration = %d, tau = %8.3e, Primal = %8.3e,
   PDGap = %8.3e, Dual res = %8.3e, Primal res = %8.3e',...
pditer, tau, sum(u), sdg, norm(rdual), norm(rpri)));
if (largescale)
disp(sprintf('                    CG Res = %8.3e, CG Iter = %
   d', cgres, cgiter));
else
disp(sprintf('                    H1lp condition number =
   %8.3e', hcond));
end

end
```

The below code is used to reconstruct OCT signal from 66% measurements. A binary sequence is used as PRBS in this case.

```
clc;clear all;close all;
k=1;for i = 3820875: 1e5 : 8720875
y1(k) = max(cp(i-1500:1:i+1500-1));k=k+1;  % find the local
    maxima of the compressed pulses measured with lowspeed
   Photodiode
end

y=y1(1:1:33)';   % take only 33 measurements

for i = 1:1:50
```

```
A1(i,:) = prbs((i-1)*50+1:1:(i)*50); % The PRBS used in the
    AWG has been split into 50 random sequences each of
    length 50 points
end
A=A1(1:1:33,:); % only 33 PRBS sequences are taken

N=50; % signal length

A_m = A*ifft(eye(N)); % Theta = PRBS*IDFT
A_m_actual = [real(A_m) -imag(A_m);imag(A_m) real(A_m)];
meas1_actual = [real(y);imag(y)];

x0 = pinv(A_m_actual)*meas1_actual; % initial point
x = l1eq_pd(x0,A_m_actual,A_m_actual',meas1_actual,1e-3,21)
    ; % L1-magic

x_real = x(1:50,1);
x_imag = x(51:100,1);

z = complex(x_real,x_imag);

x_hat = (abs(ifft(z))); %reconstructed OCT signal
sig = interp1(x_hat,[0.1:0.1:40],'spline'); % interpolated
    signal
figure(1);createfigure(time,inter_500);
```

```
t=time(1:1e5); % time scale

M=length(inter(1:1e5)); % actual interference pulse
    measured with high speed oscilloscope
deltat=(t(2)-t(1)); % sampling interval
T=deltat*M; % actual signal duration
t=(-T/2:deltat:T/2-deltat);
deltaf=1/T; % frequency resolution
F=1/deltat; % overall bandwidth
f=linspace(-F/2-deltaf,F/2,M);
Y_w=fftshift(fft(inter(1:1e5))); % FFT of the interference
    pulse
plot(f,abs(Y_w));

rfi = 1:1:50;
r_f = ((rfi-26)/25*1.25);

r_t = (rfi-1)*0.5;

time_interpolated = interp1(r_t,[1:0.1:40],'spline'); %
    interpolated time
sig_interpolated = interp1(x_hat,[0:0.1:39],'spline'); %
    interpolated reconstrucged signal from L1 minimization
    algorithm.
```